

# Direct numerical simulation and macroscopic modeling of turbulent flows in porous media

Vom Fachbereich Produktionstechnik  
der  
UNIVERSITÄT BREMEN

zur Erlangung des Grades  
Doktor der Ingenieurwissenschaften (Dr.-Ing.)  
genehmigte

Dissertation

Von  
M. Eng. Feixiong Rao

Gutachter: Prof. Dr. Marc Avila

Prof. Dr.-Ing. habil. Udo Fritsching

Tag der mündlichen Prüfung: 13.05.2022



University of Bremen



Faculty of Production Engineering  
Center for Applied Space Technology and Microgravity  
Fluid Mechanics and Simulation Group

Dissertation for the award of the degree “Doctor of Engineering” (Dr.-Ing.) of the  
University of Bremen

## **Direct numerical simulation and macroscopic modeling of turbulent flows in porous media**

Feixiong Rao

1. Reviewer Prof. Dr. Marc Avila  
Center of Applied Space Technology and Microgravity  
University of Bremen
2. Reviewer Prof. Dr.-Ing. habil. Udo Fritsching  
Particles and Process Engineering Institute for Materials Science  
University of Bremen

Supervisor Prof. Dr. Marc Avila

**Feixiong Rao**

Direct numerical simulation and macroscopic modeling of turbulent flows in porous media

Dissertation for the award of the degree “Doctor of Engineering” (Dr.-Ing.) of the University of Bremen, October 19, 2021

Reviewers: Prof. Dr. Marc Avila and Prof. Dr.-Ing. habil. Udo Fritsching

Supervisor: Prof. Dr. Marc Avila

**University of Bremen**

Fluid Mechanics and Simulation Group

Center for Applied Space Technology and Microgravity

Faculty of Production Engineering

Am Fallturm 2

28195 Bremen

# Abstract

Turbulence in porous media is an important phenomenon in the industry. While turbulence reinforces heat and mass transfer, it also leads to more losses of kinetic energy. Turbulent flows can be calculated with direct numerical simulation (DNS) by solving the transient Navier-Stokes equations and hence accounting for all scales of turbulent motions without using any turbulence model. However, it's impractical to apply DNS in engineering questions since DNS is too computationally expensive. Therefore, macroscopic equations in which the detailed geometry is not resolved are often used to compute convection in porous media.

The purpose of this thesis is to develop a macroscopic model for convection in porous media taking the effect of momentum dispersion into account. The developed model is based on the pore-scale prevalence hypothesis (PSPH) which states that the size of turbulent eddies is restricted by the pore size. A Laplacian term is applied to approximate the effects of macroscopic velocity gradient on momentum transport. The ratio of effective viscosity to molecular viscosity is expanded as a Taylor series concerning the local Reynolds number  $Re_d$ . The pore size as the characteristic length and the mixing velocity as the characteristic velocity make up the local Reynolds number  $Re_d$ . The pore size is identified by the square root of permeability (the ability of a porous media to transmit fluids). The two leading order terms of the Taylor series are adopted in the present PSPH momentum-dispersion model. The corresponding coefficients are determined by fitting the DNS results for flows in a regular porous medium bounded by a wall.

To validate the macroscopic model, three types of porous media (a porous medium bounded by two walls, a porous medium with two porosities, and a porous medium with two length scales) are applied. The macroscopic equations are solved with a finite volume method (FVM) while the DNSs are performed by using a Lattice-Boltzmann method (LBM). In the macroscopic simulations, the porous matrix is modeled with geometric parameters, whereas all detailed geometries of porous matrix are taken into account in DNS. The results imply that the momentum dispersion generally only affects the first

representative elementary volume (REV) near the wall boundary and is independent of the Darcy number  $Da$  (the ratio of the permeability to the cross-sectional area). A series of test cases with a wide range of the Reynolds number, Darcy number, and porosity are performed. The results show that the model results are in good agreement with the DNS results.

To complement the PSPH and thus know the application boundary of our macroscopic model, the possibility of survival of macroscopic turbulence at high porosity is studied by using DNS and macroscopic simulations. The porous matrix with one or two length scales is applied. The large porous elements made of staggered arrays of square cylinders can stimulate strong macroscopic (large-scale) turbulence, while the small porous elements made of aligned arrays of spheres or cubes suppress the advent of macroscopic turbulence. The analyses are performed for various values of the Reynolds number, Darcy number  $Da_n$  (the ratio of the permeability to the element size squared), pore-scale ratio, geometry of the porous matrix, and porosity. Instantaneous Q iso-surfaces, turbulent two-point correlations, integral length scales, premultiplied energy spectra, and turbulent kinetic energy are calculated from the DNS and macroscopic simulation results to measure the size of turbulent structures quantitatively and qualitatively. In all cases, the turbulent flow is fully developed. However, the length scale of turbulence is not considerably affected by the Reynolds number, Darcy number  $Da_n$ , and pore-scale geometry. The PSPH is valid when the porosity has small or medium values. At a sufficiently large Reynolds number, large-scale turbulence survives if the porosity is larger than a critical value. The DNS and macroscopic simulation results suggest that the critical porosity  $\phi_c$  for the survival of macroscopic turbulence is between 0.93 and 0.98.

# Zusammenfassung

Turbulenzen in porösen Medien sind ein wichtiges Phänomen in der Industrie. Turbulenzen verstärken zwar den Wärme- und Stofftransport, führen aber auch zu mehr Verlusten an kinetischer Energie. Turbulente Strömungen können mit direkter numerischer Simulation (DNS) berechnet werden, indem die transienten Navier-Stokes-Gleichungen gelöst werden und somit alle Skalen turbulenter Bewegungen ohne Verwendung eines Turbulenzmodells berücksichtigt werden. Es ist jedoch unpraktisch, DNS in technischen Fragen anzuwenden, da DNS zu rechenaufwendig ist. Daher werden häufig makroskopische Gleichungen verwendet, bei denen die detaillierte Geometrie nicht aufgelöst wird, um Konvektion in porösen Medien zu berechnen.

Das Ziel dieser Arbeit ist die Entwicklung eines makroskopischen Modells für Konvektion in porösen Medien unter Berücksichtigung des Einflusses der Impulsdispersion. Das entwickelte Modell basiert auf der Porenskalen-Prävalenzhypothese (PSPH), die besagt, dass die Größe turbulenter Wirbel durch die Porengröße begrenzt wird. Ein Laplace-Term wird verwendet, um die Auswirkungen des makroskopischen Geschwindigkeitsgradienten auf den Impulstransport anzunähern. Das Verhältnis von effektiver Viskosität zu molekularer Viskosität wird als Taylor-Reihe um die lokale Reynolds-Zahl  $Re_d$  erweitert. Die Porengröße als charakteristische Länge und die Mischgeschwindigkeit als charakteristische Geschwindigkeit bilden die lokale Reynolds-Zahl  $Re_d$ . Die Porengröße wird durch die Quadratwurzel der Permeabilität (die Fähigkeit eines porösen Mediums, Flüssigkeiten zu übertragen) identifiziert. Die beiden Terme führender Ordnung der Taylor-Reihe werden in das vorliegende PSPH-Impulsdispersionsmodell übernommen. Die entsprechenden Koeffizienten werden durch Anpassung der DNS-Ergebnisse für Strömungen in einem regelmäßigen porösen Medium bestimmt, das von einer Wand begrenzt wird.

Um das makroskopische Modell zu validieren, werden drei Arten von porösen Medien (ein poröses Medium, das von zwei Wänden begrenzt wird, ein poröses Medium mit zwei

Porositäten und ein poröses Medium mit zwei Längenskalen) verwendet. Die makroskopischen Gleichungen werden mit einer Finite-Volumen-Methode (FVM) gelöst, während die DNSs mit einer Lattice-Boltzmann-Methode (LBM) durchgeführt werden. In den makroskopischen Simulationen wird die poröse Matrix mit geometrischen Parametern modelliert, während im DNS alle Detailgeometrien der porösen Matrix berücksichtigt werden. Die Ergebnisse implizieren, dass die Impulsdispersion im Allgemeinen nur das erste repräsentative Elementarvolumen (REV) nahe der Wandgrenze beeinflusst und unabhängig von der Darcy-Zahl  $Da$  (dem Verhältnis der Permeabilität zur Querschnittsfläche) ist. Es wird eine Reihe von Testfällen mit einem breiten Bereich der Reynolds-Zahl, Darcy-Zahl und Porosität durchgeführt. Die Ergebnisse zeigen, dass die Modellergebnisse gut mit den DNS-Ergebnissen übereinstimmen.

Um die PSPH zu ergänzen und damit die Anwendungsgrenzen unseres makroskopischen Modells zu kennen, wird die Überlebensmöglichkeit makroskopischer Turbulenzen bei hoher Porosität mit Hilfe von DNS und makroskopischen Simulationen untersucht. Die poröse Matrix mit einer oder zwei Längenskalen wird aufgetragen. Die großen porösen Elemente aus gestaffelten Anordnungen von quadratischen Zylindern können starke makroskopische (großflächige) Turbulenzen stimulieren, während die kleinen porösen Elemente aus ausgerichteten Anordnungen von Kugeln oder Würfeln das Auftreten makroskopischer Turbulenzen unterdrücken. Die Analysen werden für verschiedene Werte der Reynolds-Zahl, Darcy-Zahl  $Da_n$  (das Verhältnis der Permeabilität zur Elementgröße zum Quadrat), Porenskalenverhältnis, Geometrie der porösen Matrix und Porosität durchgeführt. Momentane Q-Isoflächen, turbulente Zweipunktkorrelationen, integrale Längenskalen, vormultiplizierte Energiespektren und turbulente kinetische Energie werden aus den DNS- und makroskopischen Simulationsergebnissen berechnet, um die Größe turbulenter Strukturen quantitativ und qualitativ zu messen. In allen Fällen ist die turbulente Strömung voll entwickelt. Die Längenskala der Turbulenz wird jedoch nicht wesentlich von der Reynolds-Zahl, der Darcy-Zahl  $Da_n$  und der Porenskalengeometrie beeinflusst. Die PSPH ist gültig, wenn die Porosität kleine oder mittlere Werte hat. Bei einer ausreichend großen Reynolds-Zahl überlebt großräumige Turbulenz, wenn die Porosität größer als ein kritischer Wert ist. Die Ergebnisse der DNS-

und makroskopischen Simulation legen nahe, dass die kritische Porosität  $\phi_c$  für das Überleben makroskopischer Turbulenzen zwischen 0.93 und 0.98 liegt.

# Acknowledgment

Firstly, I would like to thank Dr. Yan Jin for the support of my Ph. D study and scientific and technical discussions. Especially, I'm indebted to him for the help in preparing our joint scientific paper.

More importantly, I would like to express my sincere gratitude to Prof. Marc Avila for his understanding and essential support for the final phase of my Ph. D study. His inclusion and high morality impress me deeply. He is always glad to give a hand to me whenever I need help. And he is the wind beneath my wings. Without his unselfish dedication, I couldn't finish my Ph. D study. It's my pleasure and honor to work with you.

Thirdly, my sincere thanks also go to my fellow Ph. D students from the Fluid Simulation and Modelling group at the Center for Applied Space Technology and Microgravity. The warm and comfortable discussion atmosphere motivates me.

Last but not least, I would like to say thanks to my family for the endless and unconditional support of my study.

Financial support for my Ph. D project from China Scholarship Council (CSC) and the Center of Applied Space Technology and Microgravity (ZARM), University of Bremen, for the work environment and more specifically for the computing time in the fsm cluster, are fully acknowledged.

# Contents

Contents .....	XV
Nomenclature .....	XIX
List of Figures .....	XXV
List of Tables .....	XXX
1. Introduction.....	1
1.1 Scope of the study .....	1
1.2 Relevance .....	2
1.3 Research Motivation .....	7
1.4 Utilized Numerical Framework.....	11
1.5 Goal & Achievements .....	12
1.6 Structure of the thesis.....	12
1.7 List of Scientific Publications .....	13
2. Mathematical models and equations.....	14
2.1 Introduction .....	14
2.2 The properties of porous media.....	14
2.2.1 Porosity.....	14
2.2.2 Permeability.....	15
2.2.3 REVs.....	15
2.2.4 Tortuosity.....	16

2.3	Governing equations for microscopic DNS .....	16
2.4	Governing equations for macroscopic simulation.....	17
2.4.1	Local volume averaging .....	17
2.4.2	Macroscopic equations .....	18
2.4.3	Total drag.....	18
2.4.4	PSPH model for momentum dispersion .....	19
2.5	Model coefficients.....	21
2.6	Conclusions .....	28
3.	Numerical methods .....	29
3.1	Introduction .....	29
3.2	Finite volume method.....	29
3.2.1	Gauss integral theorem .....	29
3.2.2	Numerical scheme .....	30
3.2.3	Pressure-velocity coupling. ....	31
3.3	Lattice-Boltzmann method.....	32
3.3.1	The Boltzmann equation.....	33
3.3.2	Boundary conditions.....	35
3.4	Conclusions .....	36
4.	Flows in a porous medium bounded by walls.....	38
4.1	Introduction .....	38
4.2	Test cases in the study .....	38
4.2.1	Geometry of the porous matrix.....	38
4.2.2	Instantaneous flow fields.....	41

4.2.3 Statistical results .....	42
4.3 Conclusions .....	46
5. Flows in a porous medium with two different porosities .....	47
5.1 Introduction .....	47
5.2 Test cases in the study .....	47
5.2.1 Geometry of the porous matrix.....	47
5.2.2 Instantaneous flow fields .....	49
5.2.3 Statistical results.....	49
5.3 Conclusions .....	52
6. Flows in a porous medium with two length scales .....	53
6.1 Introduction .....	53
6.2 Test cases in the study .....	53
6.2.1 Geometry of the porous matrix.....	53
6.2.2 Instantaneous flow fields.....	55
6.2.3 Statistical results.....	56
6.3 Conclusions .....	58
7. Limit of the pore scale prevalence hypothesis .....	60
7.1 Introduction .....	60
7.2 Description of the test cases .....	60
7.3 Macroscopic equations for infinite Reynolds number .....	61
7.4 Description of the test cases .....	62
7.5 Instantaneous flow field .....	64
7.6 Two-point turbulent correlations.....	68

7.7 Integral length scales .....	74
7.8 Energy spectra and their premultiplied form.....	82
7.9 Turbulent kinetic energy .....	85
7.10 Conclusions .....	87
8. Summary and outlook.....	89
8.1 Summary .....	89
8.2 Outlook.....	90
Appendix A.....	92
Bibliography .....	94

# Nomenclature

## Abbreviations

BGK Bhatnagar-Gross-Krook operator

CFD Computational fluid dynamics

DNS Direct numerical simulation

FVM Finite volume method

GPM Generic porous matrix

LBM Lattice-Boltzmann method

PISO Pressure-Implicit scheme with Splitting of Operators

PSPH Pore-scale-prevalence hypothesis

REV Representative volumetry element

REVs Representative volumetry elements

## Dimensionless variables

$c_{B1}, c_{B2}, \dots, c_{Bn}$  the coefficients of the Taylor series with respect to  $Re_d$

$c_F, c_{F1}, c_{F2}, \dots, c_{Fn}$  the coefficients of the Taylor series with respect to  $Re_K$

$Da$  Darcy number about the ratio of the permeability to its cross-sectional area

$Da_n$  Darcy number about the ratio of the permeability to the element size

$L_x, L_y$  the longitudinal integral length scales in the parallel ( $x_1$ -) and transverse ( $x_2$ -) directions

$\tilde{L}_i$  the dimensionless Laplacian terms

$Re_{cl}$  Reynolds number based the half channel height  $H$

$Re_d = \frac{K|s_{Dij}|}{\nu}$  Reynolds number based on permeability and magnitude of the strain rate

$Re_K = \frac{\sqrt{K}|u_D|}{\nu}$  Reynolds number based on the square root of permeability and the superficial velocity

$Re_p = \frac{u_m s}{\nu}$ ,  $Re_1 = \frac{u_a s}{\nu}$ ,  $Re_2 = \frac{u_b s}{\nu}$  Reynolds number based on the pore size

$Re_s = \frac{u_m d_s}{\nu}$ ;  $Re_l = \frac{u_m d_l}{\nu}$  Reynolds number based on the element size

$\tilde{R}_i$  dimensionless drag terms

$\tilde{u}_{Di}$  dimensionless superficial velocity

$\tilde{x}_i$  dimensionless distance

$\tilde{p}$  dimensionless pressure gradient

### Discretization

$\mathbf{c}$  velocity vector of particles

$\mathbf{c}_i$  velocity vector of particles along with  $i$  direction

$c_s$  lattice speed of sound

$f(\mathbf{r}, \mathbf{c}, t)$  the probability of particles

$f_i(\mathbf{r}, \mathbf{c}_i, t)$  the probability of particles along with  $i$  direction

$f^{eq}$  collision distribution function

$f_i^{eq}$  collision distribution function along with  $i$  direction

$H(\cdot)$  the finite-difference representation of the spatial convective and diffusive fluxes of the momentum

$h$  uniform mesh size in LBM

$n$  time step

$N$  the number of cell centers in FVM

$p^*$  first corrected pressure

XX

$p^{**}$	second corrected pressure
$t$	time step
$u_f$	velocity at the interfaces of the grid cells
$\mathbf{u}^*$	tentative velocity
$\mathbf{u}^{**}$	first corrected velocity
$\mathbf{u}^{***}$	second corrected velocity
$w_i$	the weight factor for $i^{\text{th}}$ direction
$\Omega$	collision operator
$\tau$	relaxation factor

### **Hydrodynamic variables**

$A_i$	surface areas of pores
$d$	element size
$d_l$	element size of large porous elements
$d_s$	element size of small porous elements
$D_e$	size of the bed
$D_{ij}$	asymmetric tensor
$D_{p2}$	effective average particle or fiber diameter
$g_i$	applied pressure gradient
$H$	channel height
$K$	permeability
$L_i$	Laplacian term
$\mathbf{n}$	unit vector normal to the surface areas of pores

$n_i$	unit vector
$p$	pressure
$\mathbf{r}$	distance vector
$R_i$	total drag
$\hat{R}_i$	total drag far away from wall
$R_{Di}$	drag due to Darcy term
$R_{Fi}$	drag due to Forchheimer term
$R_{ij}$	overall two-point correlation
$\tilde{R}_{ij}$	non-turbulent two-point correlation
$\hat{R}_{ij}$	true two-point correlation
$s$	the pore size
$s_l$	the pore size of large porous elements
$s_s$	the pore size of small porous elements
$s_{Dij}$	the strain rate of the superficial velocity $\mathbf{u}_D$
$S$	surface of the porous elements
$u_i$	fluid velocity
$\mathbf{u}_D$	superficial velocity vector
$\mathbf{u}$	velocity vector
$u_{Di}$	superficial velocity component
$u_{cl}$	mean velocity away from the wall in the channel
$u_m$	mean seepage velocity
$u'_i$	velocity fluctuation component

$\tilde{\mu}$	effective dynamic viscosity
$\nu$	kinematic viscosity
$\tilde{\nu}$	effective viscosity
$V$	cell volume
$x_i, r_i$	distance
$\rho$	density
$\phi, \phi_s$	fraction of pore space to the total volume of porous media

### Other symbols/Notation

$\mathbf{e}_i$	unit vector
$\hat{E}_{ii}$	energy spectra
$k$	macroscopic turbulence kinetic energy
$k_i$	wavenumber along with $i$ direction
$Q = -\frac{1}{2} \frac{\partial u_i}{\partial x_j} \frac{\partial u_j}{\partial x_i}$	the second invariant of the instantaneous velocity gradient tensor
$R_{ij}(\mathbf{r}, \mathbf{x}_0) = \langle u'_i(\mathbf{x}_0, t) u'_j(\mathbf{x}_0 + \mathbf{r}, t) \rangle_t$	the averaged two-point correlation over time
$\alpha, \beta$	model coefficients of Ergun's equation
$\Lambda = 2\pi/k_1$	the maximum of wavelength

### Mathematical operators

$\langle \varphi \rangle^V$	the averaging value over the whole volume
$\langle \varphi \rangle^i$	the averaging value over the fluid volume
$\langle p \rangle^i$	the averaging pressure over the fluid volume
$\langle u_i \rangle^i$	the averaging velocity over the fluid volume
$\langle {}^i u_i {}^i u_j \rangle^i$	the averaging momentum dispersion over the fluid volume

$\langle \cdot \rangle_t$  time-averaging

# List of Figures

1.1	Examples of natural porous materials: (a) beach sand, (b) sandstone, (c) limestones, (d) rye bread, (e) wood, (f) human lung (Nield & Bejan, 2017).....	2
1.2	Schematic view of biological tissue.....	5
1.3	Schematic view of the submerged canopies. ....	6
1.4	Schematic view of CO <sub>2</sub> transfer from the soil. ....	7
2.1.	(a) Schematic geometry of the porous matrix; (b) one REV. ....	16
2.2.	Schematic geometry of the porous matrix. ....	23
2.3.	Applied pressure gradient $g_1$ versus Reynolds number $Re_K$ . The porous matrix is made of arrays of spheres. $\phi = 0.48$ ( $s/d = 1$ ), $K = 0.0026$ , $c_{F1} = 0.049$ , and $c_{F2} = 0.003$ . The DNS solutions from a high-resolution mesh ( $81^3$ grid points for each REV) and from a low-resolution mesh ( $71^3$ grid points for each REV) are compared to indicate the numerical error. ....	24
2.4.	Permeability $K$ versus porosity $\phi$ for porous matrices composed of spheres and cubes. The $K$ values obtained from DNS results are compared with the results from the Carman-Kozeny (Eq. 2.23) and Ergun (Eq. 2.26) equations. ....	25
2.5.	The Forchheimer coefficient $c_F$ versus $Re_K$ . The porous matrix is composed of spheres ( $\phi = 0.48$ ) or cubes ( $\phi = 0.42$ ). The values of $c_F$ in this study are calculated using $c_F = c_{F1} + c_{F2}Re_K$ . $c_{F1}$ and $c_{F2}$ are determined from the DNS results. They are compared with the range 0.1-0.55 suggested by Nield and Bejan (2017) and the predictions of the Ergun equation (Eq. 2.26). ....	26
2.6.	$c_{B1}$ versus porosity $\phi$ for different geometries of porous elements.....	27
2.7.	$c_{B2}$ versus porosity $\phi$ for different geometries of porous elements.....	27
3.1.	Interpolation stencils of face-neighboring cells .....	30

3.2. Grid structure and velocities with the D3Q19 discretization (Jin <i>et al.</i> 2015).....	34
3.3. (a) bounce back scheme I; (b) bounce back schemeII. ....	36
4.1. Schematic geometry of the porous matrix. (a) The porous matrices made of 3-dimensional aligned-distributed spheres for DNS; (b) the porous matrices made of 3-dimensional aligned-distributed cubes for DNS; (c) the porous matrices for macroscopic simulations. ....	39
4.2. Instantaneous velocity magnitude. In (a) and (b), the porous matrix is composed of spheres, $\phi = 0.48$ . (a) $Re_{cl}=98$ , laminar; (b) $Re_{cl}=1730$ , turbulent. In (c) and (d), the porous matrix is composed of cubes, $\phi = 0.49$ . (c) $Re_{cl}=127$ , laminar; (d) $Re_{cl}=2339$ , turbulent. ....	42
4.3. $u_{D1}/u_{cl}$ and $\langle u_{D1} \rangle^v / u_{cl}$ versus the normalized distance from the wall $x_2/H$ . The porous matrix is composed of cubes, $\phi = 0.49$ , $Re_{cl} = 127$ . Lines: $u_{D1}/u_{cl}$ obtained from continuous PSPH model results; hollow symbols: $\langle u_{D1} \rangle^v / u_{cl}$ from REV-averaged PSPH model results; solid symbols: $\langle u_{D1} \rangle^v / u_{cl}$ from REV-averaged DNS results. ....	42
4.4. $u_{D1}/u_{cl}$ and $\langle u_{D1} \rangle^v / u_{cl}$ versus the normalized distance from the wall $x_2/s$ . The porous matrix is composed of cubes, $\phi = 0.49$ , $Re_{cl} = 127$ .....	43
4.5. Streamwise velocity $\langle u_{D1} \rangle^v$ versus the normalized distance from the wall $x_2/s$ for different values of $Re_{cl}$ . The porous matrix is composed of spheres (a) and cubes (b). Hollow symbols: PSPH model results; solid symbols: DNS results. Mesh1: $101^3$ grid points for each REV; mesh 2: $76^3$ grid points for each REV.....	44
4.6. $\langle u_{D1} \rangle^v$ in the first REV next to the wall versus the applied pressure gradient $g_1$ . The porous matrix is composed of cubes. (a) the whole range of values of the applied pressure gradient; (b) zoomed results in the turbulent regime.....	46
5.1. Schematic geometry of a porous matrix with two porosities. (a) the domain for microscopic simulation, (b) the domain for macroscopic simulation. ....	48

5.2. Instantaneous velocity magnitude. The porous matrix is composed of cubes,  $\phi_1 = 0.42$ ,  $\phi_2 = 0.49$ . (a)  $Re_1 = 30$  and  $Re_2 = 60$  (laminar flow); (b)  $Re_1 = 454$  and  $Re_2 = 860$  (turbulent flow). ..... 49

5.3. REV-averaged streamwise velocity  $\langle u_{D1} \rangle^v$  versus the normalized distance from the wall  $x_2/s$ . The porous matrix is composed of cubes,  $\phi_1 = 0.42$ ,  $\phi_2 = 0.49$ . (a)  $Re_1 = 30$ ,  $Re_2 = 60$  (laminar flow); (b)  $Re_1 = 454$ ,  $Re_2 = 860$  (turbulent flow). Mesh1:  $151^3$  grid points for each REV; mesh 2:  $91^3$  grid points for each REV. .... 50

5.4.  $\langle u_{D1} \rangle^v$  in the first REV next to the wall versus applied pressure gradient  $g_1$ . (a) Cubes,  $\phi_1 = 0.42$  and  $\phi_2 = 0.49$ ; (b) cubes,  $\phi_1 = 0.42$  and  $\phi_2 = 0.54$ . ..... 52

6.1. Porous matrices used in the DNS study. (a) A porous matrix with two length scales (made of spheres); (b) a REV for the small porous element. .... 54

6.2. A porous matrix with only a large pore scale (made of bars) for macroscopic study. .... 55

6.3. Instantaneous velocity magnitude for porous medium with two length scales,  $\phi_s = 0.70$ ,  $Re_s = 620$ . (a) DNS result; (b) macroscopic simulation result. .... 56

6.4. Applied pressure gradient  $g_1$  versus Reynolds number  $Re_l$ , DNS results. The porous matrix is made of staggered arrays of bars. FVM and LBM results with different mesh resolutions are compared. .... 57

6.5. Distribution of  $\langle \bar{u}_1 \rangle^{v,x^3}$  and  $\langle \bar{u}_2 \rangle^{v,x^3}$  along the streamwise ( $x_1$ -) lines at  $x_2/s_s = 0.5$  (squares), 2.5 (circles), 4.5 (up-pointing triangles) and 6.5 (down-pointing triangles). Solid symbols indicate DNS results and hollowed symbols indicate macroscopic simulation results. The porous matrix is “bars+spheres” with  $\phi_s = 0.70$ . The Reynolds number  $Re_s$  is 436 (a, b) or 620 (c, d). .... 58

7.1 Porous matrices used in the study. (a) A porous matrix with two length scales (made of cubes and spheres); (b) a REV for the small porous element; (c) a porous matrix with only small pore scale (made of spheres); (d) a porous matrix with only large pore scale (made of bars) ..... 61

7.2	Instantaneous turbulence structures for DNS results, color coding showing the instantaneous value of the vertical velocity $u_2$ , $Q/Q_M = 2 \times 10^{-2}$ . Possible large-scale structures are indicated by circles. (a) Bars, $\phi_s = 1.0$ , $Re_l = 641$ , $Q_M d_l^2 / u_m^2 = 4.8 \times 10^3$ ; (b) Spheres, $\phi_s = 0.70$ , $Re_s = 545$ , $Re_l = 1308$ , $Q_M d_l^2 / u_m^2 = 2.04 \times 10^4$ ; (c) Bars and spheres, $\phi_s = 0.70$ , $Re_s = 536$ , $Re_l = 1286$ , $Q_M d_l^2 / u_m^2 = 1.35 \times 10^4$ ; (d) Bars and spheres, $\phi_s = 0.98$ , $Re_s = 564$ , $Re_l = 3384$ , $Q_M d_l^2 / u_m^2 = 2.01 \times 10^5$ ....65	
7.3	Instantaneous velocity magnitude for macroscopic simulation results, “bars+spheres”. (a) $\phi_s = 0.93$ , $Da_n = 0.07$ , $Re_K = 1302$ , $Re_l = 5060$ ; (b) $\phi_s = 0.98$ , $Da_n = 0.39$ , $Re_K = 1225$ , $Re_l = 1969$ ; (c) $\phi_s = 0.99$ , $Da_n = 1.26$ , $Re_K = 1135$ , $Re_l = 1009$ ; (d) $\phi_s = 1.0$ , $Re_l = 630$ ..... 67	
7.4	Correlation points in two parallel planes (Uth <i>et al.</i> , 2016)..... 68	
7.5	Turbulent two-point correlations in the streamwise $x_1$ direction (a) and transverse $x_2$ direction (b) for DNS results..... 70	
7.6	Turbulent two-point correlations in the streamwise $x_1$ direction (a) and transverse $x_2$ direction (b) for DNS results. Solid lines: “bars+spheres”, $\phi_s = 0.98$ , $Re_s = 564$ , $Re_l = 3384$ ; Dashed lines: “spheres”, $\phi_s = 0.98$ , $Re_s = 727$ , $Re_l = 4362$ ; Dash dotted lines: “bars”, $\phi_s = 1.0$ , $Re_l = 641$ ..... 71	
7.7	Turbulent two-point correlations in the streamwise $x_1$ direction (a) and transverse $x_2$ direction (b) for macroscopic simulation results. The porosity $\phi_s$ , Reynolds number $Re_l$ and $Re_K$ are varied..... 73	
7.8	Turbulent two-point correlations in the streamwise ( $x_1$ -) direction (a) and transverse ( $x_2$ -) direction (b). The porous matrix is made of staggered arrays of bars. FVM and LBM results are compared..... 74	
7.9	Effects of the Reynolds number on the integral length scales for DNS results. (a) $L_x/s_l$ , $\phi_s = 0.70$ ; (b) $L_y/s_l$ , $\phi_s = 0.70$ ; (c) $L_x/s_l$ , $\phi_s = 0.98$ ; (d) $L_y/s_l$ , $\phi_s = 0.98$ . ..... 76	
7.10	Effects of $s_l/s_s$ on the averaged integral length scales, $\phi_s = 0.70$ for DNS results. The length scales are averaged in the range $Re_s \in [436, 649]$ . (a) $\langle L_x \rangle / s_l$ ; (b) $\langle L_y \rangle / s_l$ ..... 77	

7.11 Effects of the porosity $\phi_s$ on the averaged integral length scales for DNS results. (a) $\langle L_x \rangle / s_l$ ; (b) $\langle L_y \rangle / s_l$ . .....	79
7.12 The averaged integral length scales for “bars+cubes” for DNS results. (a) $\langle L_x \rangle / s_l$ ; (b) $\langle L_y \rangle / s_l$ . .....	80
7.13 Turbulent two-point correlations in the streamwise ( $x_1$ -) direction and transverse ( $x_2$ -) direction, “bars+spheres” for macroscopic simulation results. (a) $L_x$ ; (b) $L_y$ . .....	81
7.14 Pre-multiplied energy spectra for “bars+spheres”, “bars” and “spheres” for DNS results, $s_l / s_s = 4$ . The peaks with the lowest wave numbers are indicated with solid circles. The values of $Re_s$ are 536 for “bars+spheres” with $\phi_s = 0.7$ , 564 for “bars+spheres” with $\phi_s = 0.98$ and 545 for “spheres”, respectively. The value of $Re_l$ for “bars” is 641. ....	83
7.15 Pre-multiplied energy spectra for “bars+spheres” for macroscopic simulation results. The peaks with the lowest wave numbers are indicated with solid circles.....	84
7.16 Pre-multiplied energy spectra. The porous matrix is made of staggered arrays of bars. FVM and LBM results are compared. ....	84
7.17 Normalized macroscopic turbulence kinetic energy $2\langle k \rangle / u_m^2$ versus porosity versus, $Re_l \rightarrow \infty$ , $Da_n \in [0.3, 1.2]$ , “bars+GPM”.. ..	86
7.18 Reynolds number $Re_K$ versus normalized kinetic energy of macroscopic turbulence $2\langle k \rangle / u_m^2$ , $\phi_s = 0.98$ . ....	87

# List of Tables

4.1. Main parameters for the DNS cases, LBM. The characteristic velocity is from the first REV near the wall boundary. The lowest and highest mesh resolutions for each porous matrix are shown.....	40
4.2. Main parameters for the cases of macroscopic simulation, FVM. The characteristic velocity is from the first REV near the wall boundary. ....	40
5.1. Main parameters for the DNS cases and the macroscopic simulation. The characteristic velocity is from the first REV near the interface. The lowest and highest mesh resolutions for each porous matrix are shown.....	48
7.1. Main parameters for the DNS cases, LBM. The lowest and highest mesh resolutions for each porous matrix are shown.....	63
7.2. Main parameters for the cases of macroscopic simulation, FVM. The lowest and highest mesh resolutions for each porous matrix are shown. ....	64
A1. Main parameters for the typical DNS cases, LBM. ....	93

# Chapter 1

## Introduction

### 1.1 Scope of the study

This Ph.D. thesis is committed to macroscopic modeling of laminar and turbulent flows in porous media. Flow in porous media occurs in a range of engineering applications, such as compact heat exchangers, geothermal power plants, grain storage, heat sinks, and waste management (Nield and Bejan, 2017; Vafai, 2015; Ingham and Pop, 1998). However, the DNS accounting for the detailed geometry of the porous medium is often too expensive and the macroscopic model is more convenient. Therefore, a PSPH momentum-dispersion model (Rao *et al.*, 2020) was developed to study turbulent convection in the porous media since turbulence is crucial to industry applications. This model is derived by volume-averaging the Navier-Stokes equations. The effects of the porous matrix on the losses of mechanical energy are approximated by the Darcy and Forchheimer terms. In this thesis, a Laplacian term is applied to model the effects of the macroscopic velocity gradients on momentum transport, which were ignored in the previous papers. The corresponding geometric parameters concerning the pore matrix are determined by fitting the DNS results.

The simulations are carried out using a finite volume method (FVM) and a Lattice-Boltzmann method (LBM). FVM is used to solve the macroscopic equations, whereas LBM is issued to indirectly solve the Navier-Stokes equations (DNS). The macroscopic PSPH model results and DNS results are compared to validate and verify mutually the two approaches.

Furthermore, the cheap, feasible, and efficient PSPH model and DNS are used to investigate the possibility for the survival of macroscopic turbulence. When the porosity (the fraction of pore space to the total volume of the porous medium) approaches 1, the macroscopic turbulence will emerge without the restriction of the porous matrix. The flow in the investigated porous media with periodic boundary conditions is fully developed. Multiple methods including turbulent two-point correlations, integral length scales, premultiplied energy spectra, and turbulent kinetic energy are adopted in this thesis to confirm the macroscopic turbulence in porous media with high porosity.

## 1.2 Relevance

A porous medium consists of a solid matrix with interconnected voids (Nield & Bejan, 2017). The solid matrix is assumed as rigid or undergoes negligible deformation. The voids among the solid matrix allow one single fluid or more fluids to flow through the porous media. In natural porous media, the solid matrix concerning the geometry and size is irregular. Examples include beach sand, sandstone, limestone, rye bread, wood, human lung, hair, coal, rock, and soil, see Fig. 1.1. For natural porous media, the porosity is normally lower than 0.6 (Nield & Bejan, 2017). Manmade porous media include cement, ceramics, composite materials, and high-porosity metallic foams. For manmade porous media, the porosity could approach 1, such as metallic foams (Nield & Bejan, 2017). At the University of Bremen, there is a graduate school working on porous media-related topics.

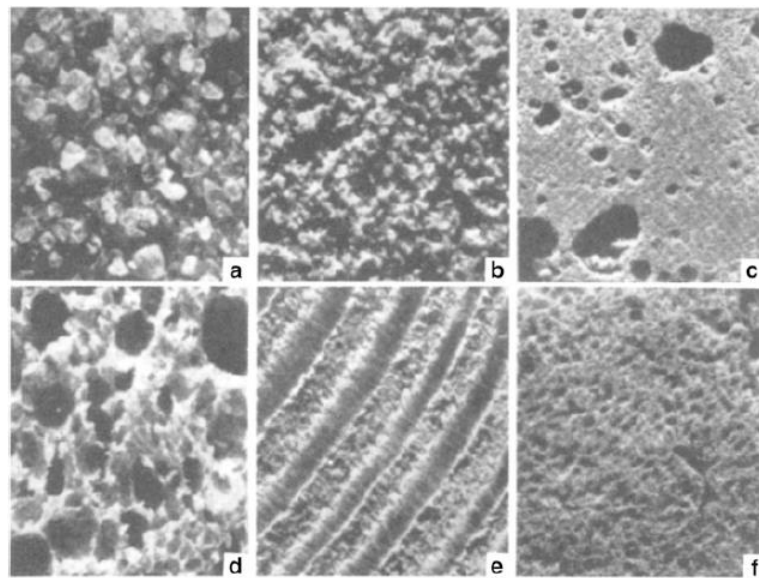


Figure 1.1. Examples of natural porous materials: (a) beach sand, (b) sandstone, (c) limestones, (d) rye bread, (e) wood, (f) human lung (Nield & Bejan, 2017).

Flows in porous media are often laminar due to their low pore-scale Reynolds number (the characteristic length is the pore size), such as seepage through saturated and unsaturated layers. However, at certain conditions, the Reynolds number based on the pore-scale might exceed its critical value for laminar-turbulence transition and thus the flow can become turbulent. Turbulent flow in porous media is welcome in many processes (Bruant *et al.*, 2002; Taheri, 2014) since it significantly enhances heat and mass transfer.

Understanding the flow in the porous media can help make contributions to the fast-growing global energy demand. Recently, the energy demand is increasing dramatically due to population growth and industrialization. Although renewable energy including solar, wind, geothermal, wave, and biofuels energy is receiving more attention and develops fast, it only accounts for around 10% of the primary energy production (Pickl, 2019). Traditional fossil oil and gas are still the main sources of energy and are strongly reliable. However, due to the limited resources, how to extract, transport, and store these valuable resources efficiently becomes considerably imperative. For example, the common methods to displace oil from the reservoir into the well are carbon dioxide and water injection. Multiphase flow in porous media is important in these processes. Understanding these effects of porous media on the flows could increase traditional crude oil production recovery efficiency. Experiments are performed to investigate the transport abilities of liquid in porous media (Grebenyuk *et al.*, 2016, 2017). Another application is how to store the hydrogen in porous media for safe and efficient large-scale energy storage, see e.g. Heinemann *et al.* (2021). This would help enable a hydrogen-related economy and protect the environment. In general, understanding the effects of the flow in the porous media deeply could contribute to the optimization in industrial processes including oil recovery and gas storage.

Turbulence in porous media has important applications in industry, such as compact heat exchangers, geothermal power plants, grain storage, heat sinks, and waste management (Nield and Bejan, 2017; Vafai, 2015; Ingham and Pop, 1998). For example, since macroscopic turbulence in porous media increases effective thermal conductivity, the charging process of the thermal storage tank in the adsorption heat pump cycle can be improved (Taheri, 2014). And the energy efficiency of heat sinks is improved by turbulence, which could be widely used in heating or cooling systems to save energy (Siavashi *et al.*, 2019). For example, heat exchangers with open-cell aluminum foams are more efficient to dissipate large amounts of heat (Boomsma, 2003) due to the dramatically increasing overall effective thermal conductivity (Calmidi and Mahajan, 1999). Hsu *et al.* (1993) argue that the turbulence inside an inert porous matrix contributes to the combustion process, such as higher burning speed and volumetric energy release rates, higher combustion stability and the ability to burn gases, and low energy content. de Lemos (2009) investigated reactive turbulence flow in porous media to determine the effects of turbulence in smoothing temperature distributions.

The effects of porous media on the flow are also applied to the cooling system of gas turbines (Cerri *et al.*, 2007). During the transpiration cooling process, the porous media wall separates the coolant gas and hot gas stream on each side of the wall. The coolant gas flows through the porous media and mixes with the hot gas. The mixed gas layer reduces the heat flux from the hot gas to the porous media wall, which increases the thermodynamic efficiency. Dahmen *et al.* (2014) used numerical simulations to research cooling efficiency using porous media models, which could be applied to cool rocket thrust chambers. The geometry of porous media was investigated in detail to increase the performance of the cooling system (Scrittore *et al.*, 2007).

Flows in porous media are also relevant to heat transfer in human tissues. The tissues can be considered as pores, whereas the blood is seen as the fluid through the voids between the pores, see Fig. 1.2. Blood convection and metabolic heat generation in the human body cause heat transfer which is referred to as bioheat (Khaled & Vafai, 2003). If the tissue temperature is over 50°C, tumor tissue is destroyed while the surrounding healthy tissue is protected (Tucci *et al.*, 2021). Therefore, bioheat is the basis for the human thermotherapy and thermoregulation system (Sanyal & Maji, 2001; Khaled & Vafai, 2003). Fan & Wang (2011) attempted to set up an accurate model for bioheat by the porous media theory. The porous media theory is most appropriate to treat bioheat because it makes fewer assumptions compared to other bioheat transfer approaches (Khaled & Vafai, 2003; Khanafer & Vafai, 2006). Volume averaging theory is adopted in the field of fluid-saturated porous media to present a general set of bioheat transfer equations for blood flows and its surrounding biological tissue (Nakayama & Kuwahara, 2008; Roetzel & Xuan, 1998).

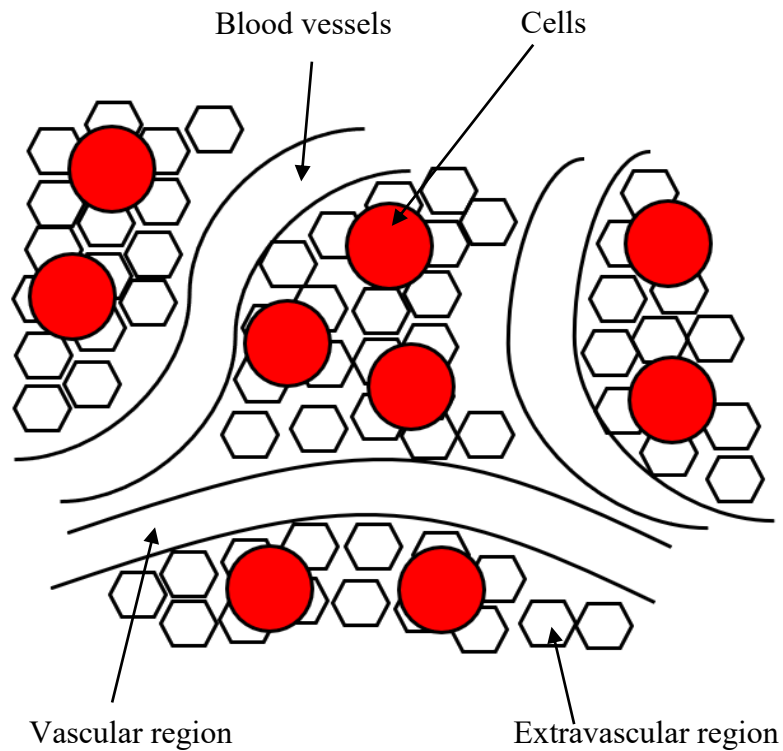


Figure 1. 2. Schematic view of biological tissue.

Turbulence in porous media is also relevant to canopy flows. Examples include the flows in porous canopies made of trees, vegetation, or buildings (Meroney, 2007). These canopies usually have large porosities (typically  $>90\%$ , see Ghisalberti & Nepf, 2009) and high permeability (the ability of a porous media to transmit fluids,  $10^{-4} - 10^{-1} \text{ m}^2$ , see Rubol *et al.*, 2018). Whether macroscopic turbulence can survive or not in porous media is a significant question for these applications. Macroscopic turbulence might enhance pollutant removal in the wetland (Serra *et al.*, 2004), benefit vegetation by augmenting nutrient uptake and/or gas exchange (Nepf, 2012), influence biological and ecological mechanisms (de Langre, 2008). One type of macroscopic turbulence is generated due to Kelvin-Helmholtz stability which occurs at the canopy interface, see Fig. 1.3. Many studies about this type of macroscopic turbulence can be found, see Breugem *et al.* (2006); Suga (2016); Kim *et al.* (2020) as examples. Nepf (2012) indicated that the lower canopy, which is far below the interface, is associated with pore-scale turbulence. However, when the lower canopy has more than one length scale, the large-scale turbulence stimulated by the large porous elements (e.g. tree trunks in a forest canopy) can be also interpreted as macroscopic turbulence.

This macroscopic turbulence might survive if it cannot be suppressed by the small porous elements (e.g. tree leaves, stems, or grass).

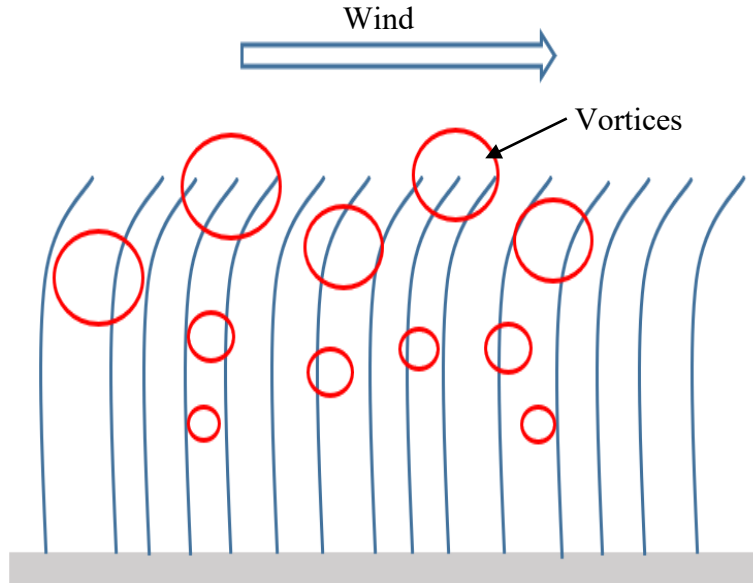


Figure 1.3. Schematic view of the submerged canopies.

In addition, turbulence in porous media can be applied in urbanization, where the city is seen as a porous medium. Hang and Li (2010) considered the buildings as porous matrix and the distance between buildings as void space. Macroscopic turbulence can help blow air pollutants in a city away efficiently, which is essential to people's health. Antohe & Lage (1997) derived a two-equation turbulence model of incompressible flow to study the macroscale flows in the city. A turbulent flow model was developed to study airflow in an urban canopy by macroscale flow experiments and numerical simulations (see Brown, 2001; Lien *et al.*, 2004). Besides, macroscopic turbulence can enhance the diffusion capacity of the heat environment and contributes to addressing global warming, particularly in cities. The mechanism of buoyancy and turbulence-driven atmospheric circulation between low-level inflow and outflow in the upper mixed layer are studied by simulating the urban canopy (Fan *et al.*, 2017). The effect of street aspect ratios on flow and heat transmission on the street (Chen *et al.*, 2020a) and building heat storage on urban heat transfer (Chen *et al.*, 2020b) are researched by a series of field experiments.

Another important application is how CO<sub>2</sub> is transported from the soil or snow to the atmosphere since soil and snow are essentially porous media (Winston *et al.*, 1995), see Fig. 1.4.

Due to the increasing level of CO<sub>2</sub> in the atmosphere, global warming is becoming worse and the ecosystem is deteriorating. The understanding of the process that CO<sub>2</sub> is transferred in the upper layers of soil or snow is significant to geological studies regarding glacial ice and climatology. During the process, the atmospheric turbulence can affect soil gas transport greatly by inducing the pressure gradients (Bowling and Massman, 2011; Maier *et al.*, 2012).

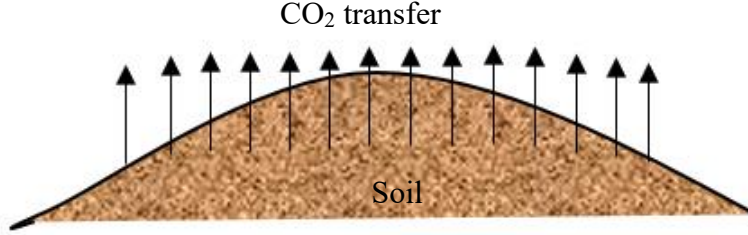


Figure 1.4. Schematic view of CO<sub>2</sub> transfer from the soil.

### 1.3 Research Motivation

Turbulence in a porous media can be calculated using direct numerical simulation (DNS), in which all geometrical details of the porous matrix and all scales of turbulent motion down to the viscous (Kolmogorov) scale are taken into account. However, DNS is often too computationally expensive and provides much more information than is usually needed, which is not practical in engineering applications. Therefore, flows in porous media are more often studied by solving macroscopic equations.

Macroscopic equations for simulating flow in a porous medium can be derived by time- and volume-averaging the Navier-Stokes equations (Pope, 2000; de Lemos, 2005). The effect of the porous matrix on the losses of mechanical energy is often approximated by the Darcy term  $\frac{\nu}{K} u_{Di}$  when the flow velocity is low, which defines as:

$$\frac{1}{\rho} \frac{\partial p_i}{\partial x_i} = -\frac{\nu}{K} u_{Di}. \quad (1.1)$$

Eq. 1.1 includes pressure  $p_i$ , distance  $x_i$ , the kinematic viscosity of the fluid  $\nu$ , permeability  $K$  and the seepage velocity  $u_{Di}$ . The Forchheimer term  $\frac{c_F}{\sqrt{K}} |u_{Di}| u_{Di}$  is used to correct the Darcy equation when the velocity is high, which defines as:

$$\frac{1}{\rho} \frac{\partial p_i}{\partial x_i} = -\frac{\nu}{K} u_{Di} - \frac{c_F}{\sqrt{K}} |u_{Di}| u_{Di}, \quad (1.2)$$

where  $c_F$  is a dimensionless coefficient. In a recent study, Lasseux *et al.* (2019) proposed a more accurate and complicated model that involves two effective coefficients for accounting for the time-decaying influence of the flow initial condition. However, the Darcy-Forchheimer equation is still the most widely used model for solving engineering problems.

Another alternative to the Darcy equation is known as the Brinkman equation, which defines as:

$$\frac{1}{\rho} \frac{\partial p_i}{\partial x_i} = -\frac{\nu}{K} u_{Di} + \tilde{\mu} \frac{1}{\rho} \frac{\partial^2 u_{Di}}{\partial x_j^2}, \quad (1.3)$$

where  $\tilde{\mu}$  is the effective dynamic viscosity. A Laplacian term is introduced in the macroscopic momentum equation to model the effects of the velocity gradient, including the effects of momentum dispersion and molecular diffusion. In early papers, the effective dynamic viscosity  $\tilde{\mu}$  in the Brinkman equation was assumed to have the same value as the molecular dynamic viscosity  $\mu$ , see Brinkman (1947). However, the experiments by Givler and Altobelli (1994) show that  $\tilde{\mu}$  may be different from  $\mu$ , and the effects of this difference were investigated e.g. by Kuznetsov (1997). Later, Valdes-Parada *et al.* (2007) argued the effective dynamic viscosity is different from the fluid dynamic viscosity only for high porosity cases. By performing a series of numerical simulations, Vafai (2015) concluded that whether  $\tilde{\mu}/\mu$  is larger or smaller than unity depends on the type of a porous medium. Ochoa-Tapia and Whitaker (1995) suggested that a value of  $\tilde{\mu}/\mu$  can be approximated as  $1/\phi$ , where  $\phi$  is the porosity of the porous medium. Thus,  $\tilde{\mu}/\mu$  is larger than unity. Bear and Bachmat (1990) suggested  $\tilde{\mu}/\mu$  to be equal to  $1/(\phi\tau^*)$ , where  $\tau^*$  is the tortuosity of the porous medium and depends on the geometry of a porous matrix. Saez *et al.* (1991) also suggested that  $\tilde{\mu}/\mu$  is close to the tortuosity which is thought to be less than unity. Based on the earlier work by Vafai and Tien (1981, 1982) and without strict validation, Hsu and Cheng (1990) proposed a momentum equation that models the momentum dispersion by the Brinkman term, in which  $\tilde{\mu}/\mu$  is set to 1.

Some studies examined the validity of the Brinkman equation. Using the Green's function approach, Durlflosky and Brady (1987) suggested that the Brinkman equation is valid for  $\phi > 0.95$ . Rubinstein (1986) argued that the Brinkman equation can be used when  $\phi$  is as small as 0.8. Nield

and Bejan (2017) argued that the Brinkman model breaks down when a large value of  $\tilde{\mu}/\mu$  is needed to match theory and experiment. Gerritsen *et al.* (2005) suggested that the Brinkman equation is not uniformly valid as the porosity tends to unity. Auriault (2009) stated that the Brinkman equation appears to be valid for flows through fixed beds of particles or fibers at very low porosity because it cannot be physically justified for classical porous media with connected porous matrices. However, in another recent study, Kuznetsov and Kuznetsov (2017) showed that the Brinkman model can fit experimental data when  $\tilde{\mu}/\mu$  is as large as 8 and reported the confidence intervals for the effective dynamic viscosity. In summary, it is still not clear whether a Laplacian term, such as one used in the Brinkman model, can be used as a reasonable approximation of momentum dispersion, especially when the porosity is small.

Some other studies suggested that the Brinkman term does not need to be taken into account in many applications since its effect is significant only in a thin boundary layer, see Nield *et al.* (2017), Tam (1969), and Levy (1981). However, in a recent DNS study, Jin and Kuznetsov (2017) showed that the Brinkman term may have an important effect near a wall when the flow is turbulent.

Jin *et al.* (2015) and Uth *et al.* (2016) studied turbulent flows in porous media using DNS and proposed the pore-scale-prevalence hypothesis (PSPH). The PSPH states that the size of turbulent eddies is restricted by the pore size. Jin and Kuznetsov (2017) further indicated that both turbulent motions and momentum dispersion are characterized by the pore size. Chu *et al.* (2018) confirmed the PSPH if the porous matrix is not sparsely packed. However, the effect of the pore size on momentum dispersion is not explicitly accounted for in previous models (Brinkman, 1947; Ochoa-Tapia and Whitaker, 1995; Hsu and Cheng, 1990).

Therefore, the first part of this thesis is to develop a PSPH model taking into account momentum dispersion based on the PSPH. Results of the PSPH model will be validated by the DNS results in which the detailed pore-scale geometry is accounted for. Through this study, whether the effects of the velocity gradient on momentum transport can be reasonably well approximated by using the Laplacian term will be answered.

The first part of this thesis focuses on a macroscopic model based on the PSPH, in which it is assumed that no macroscopic turbulence survives in porous media. However, the possibility for survival of macroscopic turbulence in porous media has been intensively studied in the past years. There are two distinct views on this question. According to the first view, macroscopic turbulence

in porous media is believed to be possible, see Lee & Howell (1991), and Antohe & Lage (1997). As a consequence, the transport of turbulence kinetic energy should be accounted for when there is macroscopic turbulence. Examples include the models by Prescott and Incropera (1995); Antohe & Lage (1997); Getachew *et al.* (2000); de Lemos (2012a). Macroscopic turbulence models have also been used to simulate flow in a porous matrix represented by a periodic array of square cylinders (Kazerooni & Hannani, 2009; Kundu *et al.*, 2014). Belcher *et al.* (2012) suggested that canopy flows are characterized by the drag length scale rather than the depth of the canopy. However, it is not clear if the drag length scale is related to macroscopic turbulence.

In the second view, macroscopic turbulence is considered impossible because of the limitation on the size of turbulent eddies imposed by the pore scale, see Nield (1991, 2001), Nakayama & Kuwahara (1999), and Kuwahara *et al.* (1998) as examples. Using an experimental method, Tanino & Nepf (2008) suggested that the integral length scale of turbulence is determined by the minimum value of the surface-to-surface distance between cylinders and the cylinder diameter, both of which belong to pore-scales. They further proposed that only turbulent eddies with mixing length scale greater than the cylinder diameter contribute significantly to dispersion, which is the transportation of solute due to both time fluctuations and spatial deviations of microscopic velocity and species concentration. Through a direct numerical simulation (DNS) study of turbulent flows in a porous medium made of square cylinders, Jin *et al.* (2015) concluded the turbulent eddies are generally restricted by the pore size, leading to the pore-scale prevalence hypothesis (PSPH). Uth *et al.* (2016) and Jin & Kuznetsov (2017) confirmed the PSPH with the DNS results for different geometries of the porous matrix.

However, the PSPH has a certain limit of validity. If the porosity approaches 1, the effect of the porous matrix on the flow will disappear and macroscopic turbulence can survive under such a condition. In Uth *et al.* (2016), a second (large) element is imposed in the porous matrix, which stimulates strong large-scale turbulence. Their DNS results show that, when the porosity for the porous matrix made of small length scales is large enough, the macroscopic turbulence seems to survive. Chu *et al.* (2018) and Srikanth *et al.* (2018) also confirmed the existence of large turbulent structures for flows with large porosities. Therefore, the PSPH should have a critical value of porosity, beyond which macroscopic turbulence might survive.

The second part of this thesis is to find out in what conditions the large turbulent structures might survive. The macroscopic turbulence in porous media is studied deeply, which is helpful to canopy flow, urbanization, and heat transfer. In addition, the PSPH theory can be complemented and the accuracy of the PSPH model can be further confirmed and refined.

## 1.4 Utilized Numerical Framework

In this work, a Lattice-Boltzmann method (LBM) and a finite volume method (FVM) are both applied to complement and verify each other. The microscopic equations (DNS) are solved with LBM, whereas the macroscopic equations are solved with the FVM. The DNS results and macroscopic results reinforce mutually.

The FVM is an integral scheme by integrating across the area, whereas the finite difference method (FDM) is a differential scheme by approximating a local Taylor expansion. Therefore, the FVM scores over the FDM when the mesh is irregular. The computational domain is discretized into finite volumes and the different variables are stored in the cell or face centers in the FVM (Hirsch, 2007). These characters allow the FVM to tackle complex geometries. The solver is developed based on the open-source computational fluid dynamics (CFD) code OpenFOAM 18.12 (OpenFOAM, 2018) which is made up of an open-source C++ library that includes domain discretization, equation implementation, and numerical equation discretization separately.

Unlike the FVM which is a general method to solve nonlinear partial differential equations in integral form, the LBM indirectly is equivalent to solving the Navier-Stokes equations by a discretized form of the Boltzmann equation. The probability of the density is simulated by streaming and collision processes over a discrete lattice. Then, the physical velocity is calculated by the probability of the density. The algorithm, uniform mesh, and efficiency on massively parallel architectures make the LBM competent to deal with complicated environments. The LBM is implemented in the Palabos library 2.2.0 which is written in C++ (Latt *et al.*, 2020). Its programming interface is comparatively friendly and easy to set up various fluid simulations. Furthermore, it allows for extended libraries and new models.

Both the LBM and FVM solvers have received intensive validations and verifications in the previous studies (Jin *et al.*, 2015, 2017; Uth *et al.*, 2016). Therefore, these numerical methods are directly used in this study. Typical DNS cases are calculated using different meshes to estimate the

uncertainty of the DNS solutions due to mesh dependence. Furthermore, the typical DNS results are compared with macroscopic results for validation of the PSPH model. Details about verification and validation are presented in chapters 4-7 and appendix A.

## **1.5 Goal & Achievements**

The first purpose of this work is to derive a PSPH model for turbulent and laminar flows in porous media. Instead of expensive DNS, this cheap, accurate, and efficient model can be widely applied in industrial applications, such as compact heat exchangers, geothermal power plants, grain storage, heat sinks, and waste management (Nield and Bejan, 2017; Vafai, 2015; Ingham and Pop, 1998). Hence this thesis could contribute to alleviating the global energy crisis by increasing the efficiency of energy transport and storage. The bioheat could be understood deeply so that thermotherapy and thermoregulation systems can be enhanced by this PSPH model which takes both laminar and turbulent flows into account.

The second goal of this work is to find under what conditions large turbulent structures might survive and the PSPH might be invalid. This research complements the PSPH and confirms further the capability of the PSPH model. This research contributes to the study of canopy flow (Meroney, 2007) and urbanization where macroscopic turbulence influences biological and ecological mechanisms, helps blow air pollutants in a city away efficiently, and enhances the diffusion capacity of the heat environment. The optimization of the spread of canopy and urbanization could be strengthened.

## **1.6 Structure of the thesis**

Chapter 2 focuses on the derivation of the macroscopic equations for flows in porous media. Firstly, the Navier-Stokes equations are volume averaged. Then, the Darcy-Forchheimer term is used to model the losses of the mechanical energy which is caused by the porous matrix. Furthermore, the process that a PSPH model is developed for flows in porous media is shown. Finally, how to determine the corresponding coefficients of the PSPH model is shown.

Chapter 3 is devoted to the numerical methods applied in the study. The FVM discretizes the Navier-Stokes equations by linear interpolation for spatial discretization and PISO algorithms for correcting the velocity. The LBM adopts the particle distributions to solve the Navier-Stokes

equations indirectly. The bounce-back model applied in the boundary conditions is to give second-order numerical accuracy.

Chapters 4-6 are devoted to the validation of the macroscopic equations. To validate the proposed PSPH model, the flow simulations are performed in three types of porous media including a porous medium bounded by two walls, a porous medium with two porosities, and a porous medium with two length scales. The macroscopic equations are solved with the FVM, whereas the microscopic equations (DNS) are solved with the LBM. The model results are compared with the DNS results in a wide range of the Reynolds number, Darcy number, and porosity.

In chapter 7, the microscopic equations (DNS) and the developed PSPH macroscopic model are used to find the critical value of porosity above which the large turbulent structures might emerge. The turbulent flow with various values of the Reynolds number, pore-scale ratio, geometry of the porous matrix, Darcy number, and porosity is simulated in porous matrices with one or two length scales. Turbulent two-point correlations, integral length scales, premultiplied energy spectra, and turbulent kinetic energy are adopted to find the critical value. At the end of the chapter, the capability of using this PSPH model is further investigated by comparing DNS results and macroscopic results.

Finally, in chapter 8 the main conclusions in the dissertation are shown and the outlooks of further work are discussed.

## **1.7 List of Scientific Publications**

RAO, F., KUZNETSOV, A. V. & JIN, Y. 2020 Numerical modeling of momentum dispersion in porous media based on the pore scale prevalence hypothesis. *Transp Porous Med* **133**, 271-292.

RAO, F. Possibility for survival of macroscopic turbulence in porous media with high porosity. Submitted to *J. Fluid Mech.* for publication, under review.

# Chapter 2

## Mathematical models and equations

### 2.1 Introduction

In this chapter, the derivation of the PSPH model is introduced in detail. Although the DNS takes into account all scales of turbulent motions, it is too expensive to apply in industrial applications. Therefore, turbulence models in porous media are more popular. However, in previous studies (e.g. Brinkman, 1947; Ochoa-Tapia and Whitaker, 1995; Hsu and Cheng, 1990), the effect of the pore size on momentum dispersion was ignored. In this chapter, the effects of the macroscopic velocity gradient on momentum transport are accounted for and approximated by a Laplacian term. A Taylor expansion is made for the effective viscosity with respect to the local Reynolds number. The corresponding model constants are determined by fitting a series of DNS cases in chapter 2.

### 2.2 The properties of porous media

Porous media are widely spread in nature, such as beach sand, sandstone, and the human lung. Fluid flow through the void of porous media is important in many applications, such as waste storage in deep geological formations, water, and contaminants in aquifers. To derive macroscopic models for fluid flows in porous media, it's necessary to study the main properties of porous media first.

#### 2.2.1 Porosity

The porosity  $\phi$  of a porous medium is defined as the fraction of pore space to the total volume of the porous medium, precisely

$$\phi = \frac{V_f}{V_s + V_f}, \quad (2.1)$$

where  $V_s$  and  $V_f$  are the solid and fluid volumes, respectively, and  $V_s + V_f$  is the total volume of the porous medium. According to the definition, the value  $\phi$  is between 0 and 1. The smallest porosities in common materials can be around 0.012, as in coal and concrete. The largest porosities can approach the value 1, as in porous canopies (Meroney, 2007) and metallic foams. In this work, the porous medium is considered a rigid or non-deformable domain. Thus, the porosity is a non-changing value.

### 2.2.2 Permeability

The permeability  $K$  is the ability of a porous media to transmit fluids. It is commonly estimated by the ratio of the flow rate to the applied pressure according to Darcy law. Its dimension is (length)<sup>2</sup>. The coefficient  $K$  is independent of the nature of the fluid but depends on the geometry of the porous medium. In isotropic porous media, the permeability is independent of the direction. In this thesis, the considered porous media are assumed isotropic and the permeability is hence a scalar.

### 2.2.3 REVs

In porous media, representative elementary volumes (REV) are the smallest volumes that can represent properties (such as porosity and permeability) of the whole domain. For homogeneous, regular porous media and laminar flow, the size of REV is of the order of the pore scale which is the smallest relevant geometric scale. For the same porous media but in turbulent flow, Jin *et al.* (2015) argued that the size of REV is as same as the one for laminar flow when the porosity has small or moderate values. In this work, the REV refers to the smallest relevant geometric cell, as shown in Fig. 2.1.

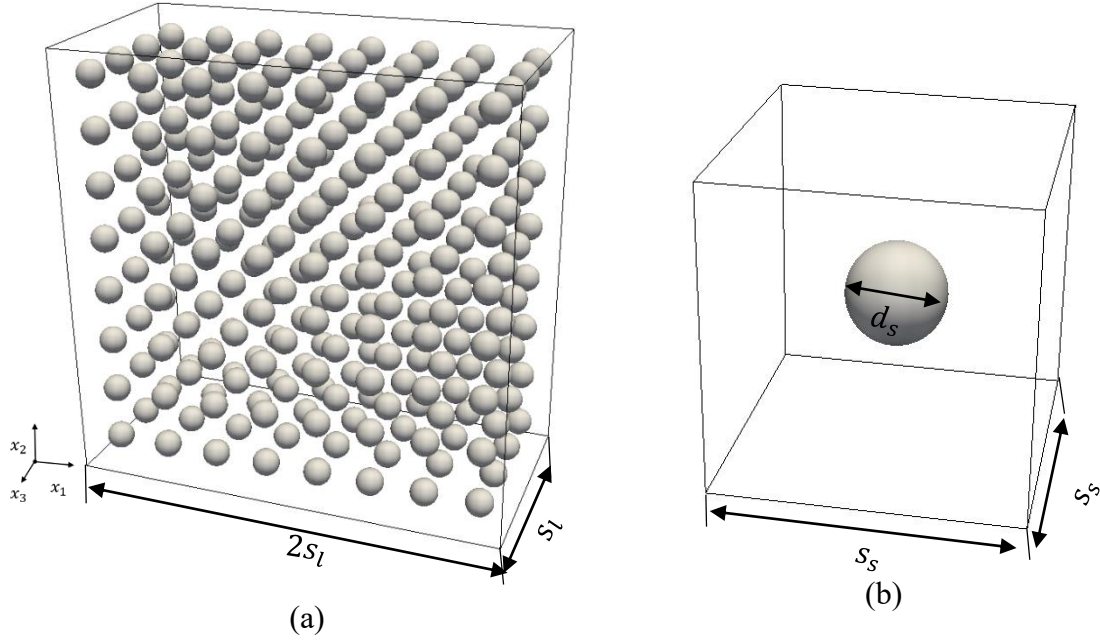


Figure 2.1. (a) Schematic geometry of the porous matrix; (b) one REV.

#### 2.2.4 Tortuosity

In porous media, tortuosity refers to the diffusion in the fluid flow (Epstein, 1989). The simplest mathematical method to get tortuosity is the arc-chord ratio which is the ratio of the length of the curve to the distance between its ends. Hart *et al.* (1999) approached the tortuosity as the integral of the square of the curvature. Further, Grisan *et al.* (2003) suggested that the curve was divided into several parts with the fixed curvature. The integral of the square of derivative of curvature was applied to measure the tortuosity in Patasius *et al.* (2005). Despite its widespread use in industry, the definition of tortuosity remains ambiguous.

### 2.3 Governing equations for microscopic DNS

The governing microscopic equations for incompressible flows in porous media are the transient Navier-Stokes equations. They read

$$\frac{\partial u_i}{\partial x_i} = 0, \quad (2.2)$$

$$\frac{\partial u_i}{\partial t} + \frac{\partial u_i u_j}{\partial x_j} = -\frac{1}{\rho} \frac{\partial p}{\partial x_i} + \nu \frac{\partial^2 u_i}{\partial x_j^2} + g_i. \quad (2.3)$$

The dimensions of the velocity  $u_i$ , distance  $x_i$ , time  $t$ , density  $\rho$ , pressure  $p$ , kinematic viscosity of the fluid  $\nu$ , and negative of the applied pressure gradient  $g_i$  (assumed to be a constant value) in Eqs. (2.2) and (2.3) are [LT], [L], [T], [ML<sup>-3</sup>], [ML<sup>-1</sup>T<sup>-2</sup>], [L<sup>2</sup>T<sup>-1</sup>], and [LT<sup>-2</sup>], respectively, where L, T and M can be any units of length, time, and mass.

The purpose of performing microscopic DNS is to determine the model coefficients and to obtain the data for model validation. Because the detailed geometry of the porous matrix is accounted for in microscopic DNS, no additional model is necessary and the results are physically correct, provided that all scales of turbulent motion down to the Kolmogorov scale are resolved.

## 2.4 Governing equations for macroscopic simulation

### 2.4.1 Local volume averaging

To get macroscopic equations, volume averaging the Navier-Stokes equations over the representative elementary volumes (REVs) is applied. The volumetric averaging value of the general fluid property  $\varphi$  over a REV can be written as

$$\langle \varphi \rangle^V = \frac{1}{\Delta V} \int_{\Delta V} \varphi dV, \quad (2.4)$$

Where  $\varphi$  could be any variable under consideration and  $\langle \cdot \rangle^V$  denotes the average of a REV of size  $\Delta V$  including the solid and fluid volumes. The relationship between this averaging value and the intrinsic average is

$$\langle \varphi \rangle^V = \phi \langle \varphi \rangle^i, \quad (2.5)$$

where  $\langle \cdot \rangle^i$  only denotes the average of the fluid volumes and  $\phi$  is the porosity.

Based on the Theorem of Local Volumetric Average (Slattery, 1967; Whitaker, 1969, 1999; Gray and Lee, 1977), the volumetric averaging values of the derivatives are written as

$$\langle \nabla \varphi \rangle^V = \nabla (\phi \langle \varphi \rangle^i) + \frac{1}{\Delta V} \int_{A_i} \mathbf{n} \varphi dS, \quad (2.6)$$

$$\langle \nabla \cdot \varphi \rangle^V = \nabla \cdot (\phi \langle \varphi \rangle^i) + \frac{1}{\Delta V} \int_{A_i} \mathbf{n} \cdot \varphi dS, \quad (2.7)$$

$$\langle \frac{\partial \varphi}{\partial t} \rangle^V = \frac{\partial}{\partial t} (\phi \langle \varphi \rangle^i) - \frac{1}{\Delta V} \int_{A_i} \mathbf{n} \cdot (\mathbf{u}_i \varphi) dS. \quad (2.8)$$

where  $A_i$ ,  $\mathbf{u}_i$  and  $\mathbf{n}$  are the surface areas of pores, the fluid velocity and the unit vector normal to  $A_i$ , respectively.

### 2.4.2 Macroscopic equations

Based on the Theorem of Local Volumetric Average, the Macroscopic equations for flows in porous media are derived by volume averaging the Navier-Stokes equations. The approach of derivation is similar to that used by de Lemos (2012a, 2012b), who averaged the governing equations (2.2)-(2.3) over volume and time. By contrast, only volume averaging was used in our derivation. The macroscopic equations are expressed as

$$\frac{\partial(\phi\langle u_i \rangle^i)}{\partial x_i} = 0, \quad (2.9)$$

$$\frac{\partial(\phi\langle u_i \rangle^i)}{\partial t} + \frac{\partial(\phi\langle u_i \rangle^i \langle u_j \rangle^j)}{\partial x_j} = -\frac{1}{\rho} \frac{\partial(\phi p)}{\partial x_i} + \phi g_i - \phi R_i + \nu \frac{\partial^2(\phi\langle u_i \rangle^i)}{\partial x_j^2} - \frac{\partial(\phi\langle^i u_i \rangle^i \langle u_j \rangle^j)}{\partial x_j}. \quad (2.10)$$

$R_i$  denotes the total drag caused by the effect of the porous matrix.

It should be noted that an undetermined tensor  $\phi\langle^i u_i \rangle^i \langle u_j \rangle^j$ , which corresponds to momentum dispersion, appears in Eq. (2.10). The spatial deviation  ${}^i\varphi$ , where  $\varphi$  could be any variable under consideration, is the difference between the real value and its intrinsic average, calculated as

$${}^i\varphi = \varphi - \langle \varphi \rangle^i, \quad (2.11)$$

$\phi\langle^i u_i \rangle^i \langle u_j \rangle^j$  needs to be closed before the macroscopic equations (2.9)-(2.10) can be solved.

### 2.4.3 Total drag

Far away from wall boundaries, the total drag  $R_i$  is usually approximated by the Forchheimer extension of the Darcy equation  $\hat{R}_i$  (Lage and Antohe, 2000),

$$R_i = \hat{R}_i = R_{Di} + R_{Fi} = \frac{\nu}{K} u_{Di} + \frac{c_F}{\sqrt{K}} |\mathbf{u}_D| u_{Di}, \quad (2.12)$$

$u_{Di}$  denotes the seepage velocity  $\phi\langle u_i \rangle^i$ .  $\mathbf{u}_D$  is the superficial velocity vector and  $c_F$  is a dimensionless coefficient, which accounts for the nonlinear increase of the form-drag with the velocity. Masuoka and Takatsu (1996) and Wood *et al.* (2020) stated that the Darcy–Forchheimer law appears to be valid for both laminar ( $c_F = 0$ ) and turbulent flows. The permeability  $K$  is a measure of the ability of a porous medium to allow fluids to pass through it. For isotropic,

homogeneous porous media,  $K$  is traditionally determined by the ratio of  $\nu u_{D1}$  and  $g_1 - \frac{1}{\rho} \frac{\Delta p}{\Delta x}$  as the flow velocity is small (approaches 0), where  $\Delta p$  is the increase of pressure over the length  $\Delta x$ .

Some studies show that  $c_F$  is not a constant but is related to the superficial (filtration) flow velocity, see Lage *et al.* (1997). Here, a Taylor expansion is made for  $\hat{R}_i$  with respect to a local Reynolds number,  $Re_K$ , calculated as

$$\hat{R}_i = \frac{\nu}{K} u_{Di} (1 + c_{F1} Re_K + c_{F2} Re_K^2 + \dots + c_{Fn} Re_K^n + O(Re_K^{n+1})). \quad (2.13)$$

$c_{F1}, c_{F2}, \dots, c_{Fn}$  are the coefficients of the Taylor series.  $Re_K$  is the local Reynolds number based on the permeability, calculated as

$$Re_K = \frac{\sqrt{K} |\mathbf{u}_D|}{\nu}. \quad (2.14)$$

Comparing Eqs. (2.13) and (2.12), it is evident that  $c_F$  is calculated as

$$c_F = c_{F1} + c_{F2} Re_K + \dots + c_{Fn} Re_K^{n-1} + O(Re_K^n). \quad (2.15)$$

In this study,  $\hat{R}_i$  is approximated with the three leading order terms of Eq. (2.13), as

$$\hat{R}_i \approx \frac{\nu}{K} u_{Di} (1 + c_{F1} Re_K + c_{F2} Re_K^2). \quad (2.16)$$

The dependence of  $c_F$  on the velocity is taken into account in Eq. (2.16).

#### 2.4.4 PSPH model for momentum dispersion

The gradient of macroscopic velocity might affect the momentum dispersion  $\phi \langle {}^i u_i {}^i u_j \rangle^i$ , molecular diffusion  $2\nu s_{Dij}$ , and total drag  $R_i$ . A Laplacian term  $L_i$  is used to account for the effect of the gradient of  $u_{Di}$  on the momentum dispersion  $\phi \langle {}^i u_i {}^i u_j \rangle^i$ , molecular diffusion  $2\nu s_{Dij}$ , and total drag  $R_i$ , expressed as

$$L_i = \phi (R_i - \hat{R}_i) + \nu \frac{\partial^2 u_{Di}}{\partial x_j^2} - \frac{\partial(\phi \langle {}^i u_i {}^i u_j \rangle^i)}{\partial x_j} = \tilde{\nu} \frac{\partial^2 u_{Di}}{\partial x_j^2}. \quad (2.17)$$

A symmetric tensor  $D_{ij} = 2\tilde{\nu} s_{Dij}$  is introduced to account for its effects, where  $s_{Dij}$  is the strain rate of the superficial velocity  $\mathbf{u}_D$  and  $\tilde{\nu}$  is an effective viscosity.

The macroscopic equation (2.10) becomes

$$\frac{\partial u_{Di}}{\partial t} + \frac{\partial(u_{Di}u_{Dj}/\phi)}{\partial x_j} = -\frac{1}{\rho} \frac{\partial(\phi(p)^i)}{\partial x_i} + \phi g_i - \phi R_i + \frac{\partial D_{ij}}{\partial x_j}, \quad (2.18)$$

and  $\tilde{v}/\nu$  is often treated as a constant or a function of the porosity (Brinkman, 1947; Ochoa-Tapia and Whitaker, 1995). However, the DNS results by Jin *et al.* (2017) showed that the magnitude of  $\tilde{v}$  increases with increasing local Reynolds number, as the momentum dispersion becomes more important. A new Reynolds number that characterizes the strength of the local momentum dispersion is proposed. According to the PSPH, the characteristic length scale of the flow in a porous medium is the pore size  $s$ . In a review paper, Wood *et al.* (2020) suggested that the pore size can be characterized by the mean particle diameter for a generic porous matrix (GPM). In this study,  $\sqrt{K}$  is used to characterize the pore size  $s$ , because  $\sqrt{K}$  has a linear relationship with  $s$  when the shape of the porous matrix is fixed.  $\sqrt{K}$  is also used as the length scale because it is easy to determine  $K$  for a porous matrix.

Jin and Kuznetsov (2017) suggested that the characteristic velocity for flows in porous media close to the wall is the product of  $\sqrt{K}$  and the magnitude of the strain rate  $|s_{Dij}|$ , calculated as

$$|s_{Dij}| = (2s_{Dij}s_{Dij})^{1/2}. \quad (2.19)$$

This is similar to the mixing length model of Prandtl (1925), in which the fluid is assumed to mix within the mixing length due to turbulent fluctuations.

Using  $\sqrt{K}$  and  $|s_{Dij}|\sqrt{K}$  as the characteristic length and velocity, respectively,  $Re_d$  is defined as

$$Re_d = \frac{K|s_{Dij}|}{\nu}. \quad (2.20)$$

For a one-dimensional wall-bounded flow,  $Re_d$  represents the ratio between the inertial force  $u|du/dy|$  and the resisting force according to the Darcy law,  $\frac{\nu}{K}u$ , where  $u$  is the macroscopic streamwise velocity and  $y$  is the distance from the wall.

The ratio  $\tilde{v}/\nu$  approaches a constant value  $c_{B1}$  when the Reynolds number  $Re_d$  approaches 0. A Taylor expansion with respect to  $Re_d$  can be made for  $\tilde{v}/\nu$ , as follows

$$\tilde{v}/\nu = c_{B1} + c_{B2}Re_d + \dots + c_{Bn}Re_d^{n-1} + O(Re_d^n), \quad (2.21)$$

where  $c_{B1}$ ,  $c_{B2}$ ,  $\dots$ ,  $c_{Bn}$  are the coefficients of the Taylor series. In this study, the two leading order terms of Eq. (2.21) are taken, i.e.,

$$\tilde{\nu}/\nu \approx c_{B1} + c_{B2}Re_d. \quad (2.22)$$

The effective viscosity  $\tilde{\nu}$  in Eq. (2.18) can be determined using Eq. (2.22).

## 2.5 Model coefficients

The model coefficients  $K$ ,  $c_{F1}$ ,  $c_{F2}$ ,  $c_{B1}$ , and  $c_{B2}$  are geometric parameters which are independent of the flow condition. They need to be determined before the macroscopic equations (2.9)-(2.10) can be solved. Various empirical and half-empirical correlations exist for calculating these coefficients.

In the case of beds of particles or fibers, the permeability  $K$  can be approximated by the Carman–Kozeny equation (Kozeny, 1927; Carman, 1956)

$$K = \frac{D_{P2}^2 \phi^3}{180(1-\phi)^2}, \quad (2.23)$$

where  $D_{P2}$  is an effective average particle or fiber diameter.

$c_F$  is often set to a constant in previous studies, so  $c_F$  is identical to  $c_{F1}$  and  $c_{F2}$  is 0 according to Eq. (2.15). Ward (1964) suggested that  $c_F$  is a universal constant, with a value of approximately 0.55. In a later study, Beavers *et al.*(1973) showed that for the case in which the solid matrix is made out of spheres,  $c_F$  can be better expressed as

$$c_F = 0.55 \left( 1 - 5.5 \frac{d}{D_e} \right), \quad (2.24)$$

where  $d$  is the sphere diameter and  $D_e$  is the size of the bed. Nield and Bejan (2017) suggested that  $c_F$  depends on the nature of the porous medium, and can be as small as 0.1. Irmay (1958) suggested an alternate equation for calculating the total drag  $R_i$ , i.e.,

$$R_i = \frac{\beta(1-\phi)^2}{D_{P2}^2 \phi^3} u_{Di} + \frac{\alpha(1-\phi)}{D_{P2} \phi^3} |\mathbf{u}_D| u_{Di}, \quad (2.25)$$

which is known as Ergun's equation. The model coefficients  $\alpha$  and  $\beta$  are set to 1.75 and 150, respectively.  $K$  and  $c_F$  in Eq. (2.25) are calculated as

$$K = \frac{D_{P2}^2 \phi^3}{\beta(1-\phi)^2}, c_F = \alpha \beta^{-1/2} \phi^{-3/2}. \quad (2.26)$$

To my knowledge,  $c_{B2}$  has never been accounted for in the previous studies; Brinkman (1947) set  $c_{B1}$  to 1. Thus,  $D_{ij}$  in Eq. (2.18) is calculated as

$$D_{ij} = \nu \frac{\partial u_{Di}}{\partial x_j}, \quad (2.27)$$

which neglects momentum dispersion. The same assumption is also used in the macroscopic equations proposed by Hsu and Cheng (1990).

The results of Ochoa-Tapia and Whitaker (Ochoa-Tapia & Whitaker, 1995) suggest that  $c_{B1} = \frac{1}{\phi}$ .  $D_{ij}$  is then calculated as

$$D_{ij} = \frac{\nu}{\phi} \frac{\partial u_{Di}}{\partial x_j}. \quad (2.28)$$

In practice, it's found that the correlations above may produce considerable errors since these model coefficients are related to the geometry of the porous matrix. The concept of tortuosity was introduced in some studies to account for the variation of pore-scale geometries. However, it is hard to determine the tortuosity. Also, I have not found a clear relationship between the model coefficients and the tortuosity. Therefore, the concept of tortuosity is not used in this thesis.

With the fast development of high-performance computers, it is possible to determine the model coefficients directly from the CFD results. To determine the model coefficients, DNS is used to compute the flow in porous media bounded by two walls. Periodic boundary conditions are used in the streamwise and transverse directions. The number of REV's in the wall-normal direction should be large enough so that the flow near the central region is not affected by the walls.

Two types of porous matrices are utilized in this study; they are composed of arrays of spheres or cubes. A schematic geometry of a porous matrix is shown in Fig. 2.2. The porous matrix is composed of 128 ( $4 \times 8 \times 4$ ) REV's. The domain size is  $4s \times 8s \times 4s$ , where the pore size  $s$  is defined as the distance between two adjacent solid elements. The viscosity  $\nu$  is set to  $0.002 \text{ L}^2\text{T}^{-1}$ .  $g_1$  is varied to obtain different Reynolds numbers. The simulations are performed using the LBM. The grid points are uniformly distributed.  $(41 s/d)^3$  grid points are used in each REV for laminar

flows.  $d$  is the size of the porous element.  $(81 s/d)^3$  grid points are used in each REV for turbulent flows. Up to 161 million grid points are used in the study.

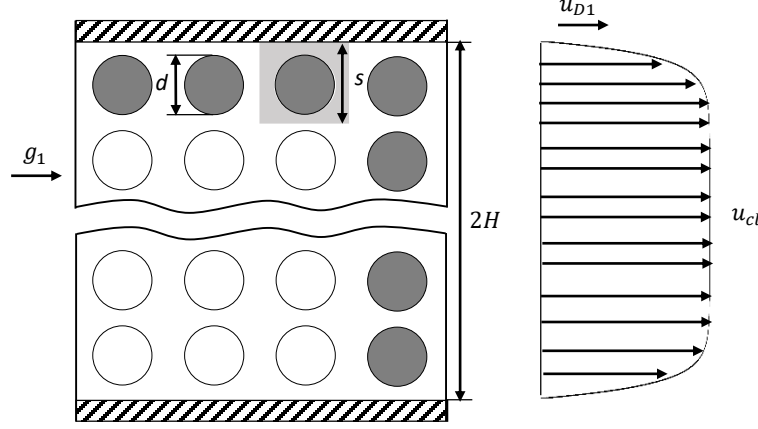


Figure 2.2. Schematic geometry of the porous matrix.

Since a wall is expected to affect the flow in a few REV's next to it, the macroscopic equation in the central region of the channel can be simplified to

$$g_1 - R_1 = g_1 - \frac{\nu}{K} u_{D1} (1 + c_{F1} Re_K + c_{F2} Re_K^2) = 0. \quad (2.29)$$

In order to determine the value of  $K$ ,  $g_1$  is specified firstly and then calculate the seepage velocity  $u_{D1}$ . I then calculate the approximate value of  $K$  by fitting the DNS results with  $g_1 = \frac{\nu}{K} u_{D1}$  for  $1 \leq Re_p \leq 20$ , where  $Re_p$  is the Reynolds number based on the pore size  $s$ . The corresponding values of  $Re_K$  are in the range 0.04-0.8. Ward (1964) suggested that the transition from the Darcy regime to the Forchheimer regime occurs in the  $Re_K$  range 1-10, so the flow is still in the Darcy regime. I did not determine  $K$  for very small values of  $Re_p$  because it leads to a considerable error for flows with large  $Re_K$  values. I then set  $c_{F2}$  in Eq. (2.29) to 0, and adjusted the values of  $K$  and  $c_{F1}$  by fitting the microscopic DNS results with Eq. (2.29) for  $Re_K \leq 3$ . After  $K$  and  $c_{F1}$  are determined, the value of  $c_{F2}$  is obtained by fitting the microscopic DNS results for  $Re_K > 3$ . The solution of Eq. (2.29) and the microscopic DNS results for the porous matrix composed of spheres are compared in Fig. 2.3. Typical turbulent cases are recalculated using a different resolution ( $71^3$  grid points for each REV) to estimate the uncertainty due to the mesh resolution. It can be seen

that our DNS solutions are generally mesh-independent. It is evident that  $c_{F2}$  has significant effects at large  $Re_K$  values.

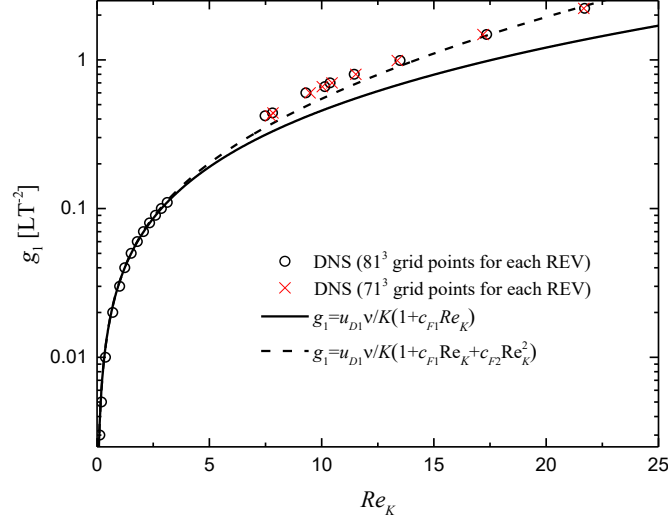


Figure 2.3. Applied pressure gradient  $g_1$  versus Reynolds number  $Re_K$ . The porous matrix is made of arrays of spheres.  $\phi = 0.48$  ( $s/d = 1$ ),  $K = 0.0026$ ,  $c_{F1} = 0.049$ , and  $c_{F2} = 0.003$ . The DNS solutions from a high-resolution mesh ( $81^3$  grid points for each REV) and from a low-resolution mesh ( $71^3$  grid points for each REV) are compared to indicate the numerical error.

The values of  $K$  for different geometries of porous elements are shown in Fig. 2.4. It can be seen that the geometry of the porous matrix has significant effects on the model coefficients. The correlations proposed in the previous studies produce considerable errors, particularly for large values of  $\phi$ . Therefore, instead of using the correlations in the references, the values of  $K$  are determined by fitting with the DNS results obtained in this study.

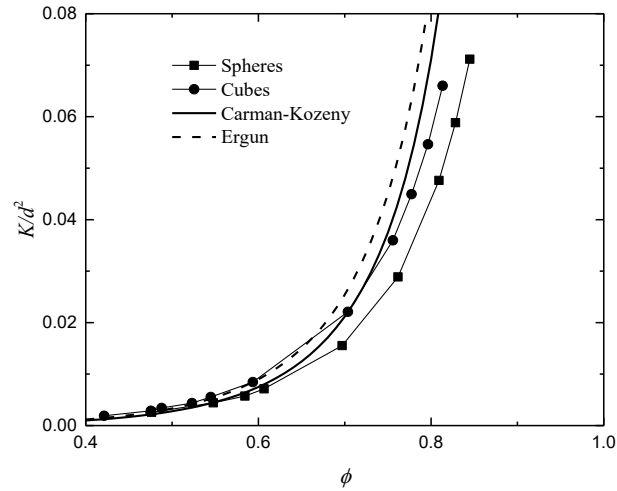


Figure 2.4. Permeability  $K$  versus porosity  $\phi$  for porous matrices composed of spheres and cubes. The  $K$  values obtained from DNS results are compared with the results from the Carman–Kozeny (Eq. 2.23) and Ergun (Eq. 2.26) equations.

The values of  $c_F = c_{F1} + c_{F2}Re_K$  for the porous matrices composed of spheres and cubes are shown in Fig. 2.5. Values of  $c_{F1}$  and  $c_{F2}$  are also obtained directly by fitting the DNS results. It can be seen that the values of  $c_F$  for a porous matrix composed of spheres are close to the lower limit of the values suggested by Nield and Bejan (2017). The values of  $c_F$  for a porous matrix composed of cubes are even lower.

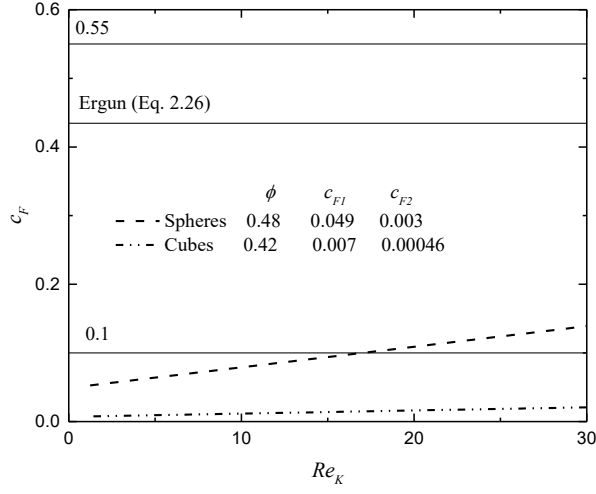


Figure 2.5. The Forchheimer coefficient  $c_F$  versus  $Re_K$ . The porous matrix is composed of spheres ( $\phi = 0.48$ ) or cubes ( $\phi = 0.42$ ). The values of  $c_F$  in this study are calculated using  $c_F = c_{F1} + c_{F2}Re_K$ .  $c_{F1}$  and  $c_{F2}$  are determined from the DNS results. They are compared with the range 0.1-0.55 suggested by Nield and Bejan (2017) and the predictions of the Ergun equation (Eq. 2.26).

When the flow is developed fully and keeps steady, the macroscopic equation near the wall can be simplified to

$$\phi g_1 - \phi R_1 + \frac{d}{dx_1}(\tilde{\nu}D_{12}) = 0. \quad (2.30)$$

The coefficients for calculating  $R_1$  have already been determined above.  $c_{B1}$  and  $c_{B2}$  are determined by fitting the solution of Eq. (2.30) near the wall to the DNS results. The error of  $R_1$  in the central region may affect the accuracy of  $c_{B1}$  and  $c_{B2}$ . To avoid this uncertainty, the value of  $c_{F2}$  is adjusted so that the calculated velocity at the center line  $u_{cl}$  is identical to the DNS results.

$c_{B2}$  is firstly set to 0.  $c_{B1}$  is adjusted until the solution of Eq. (2.30) averaged in the first REV close to the wall is identical to the DNS results. The DNS results for  $Re_K \leq 1$  are used to determine  $c_{B1}$ . The values of  $c_{B1}$  for different geometries of porous elements are shown in Fig. 2.6.

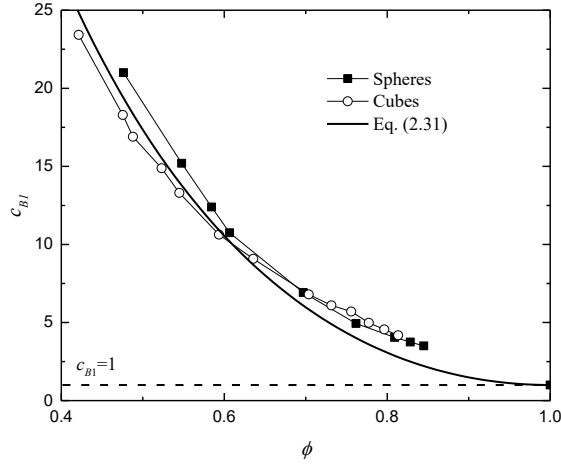


Figure 2.6.  $c_{B1}$  versus porosity  $\phi$  for different geometries of porous elements.

It can be seen that  $c_{B1}$  approaches 1 as  $\phi$  increases asymptotically to 1, while it approaches infinity as  $\phi$  decreases asymptotically to 0. This agrees with physical expectations.  $c_{B1}$  does not change significantly when the geometry of the porous matrix is changed. It can be reasonably approximated as

$$c_{B1} = 49.63 \times \frac{(1-\phi)^2}{\phi^{0.5}} + 1. \quad (2.31)$$

$c_{B2}$  is determined by fitting the model results to the DNS results for  $Re_K > 1$ , see Fig. 2.7.

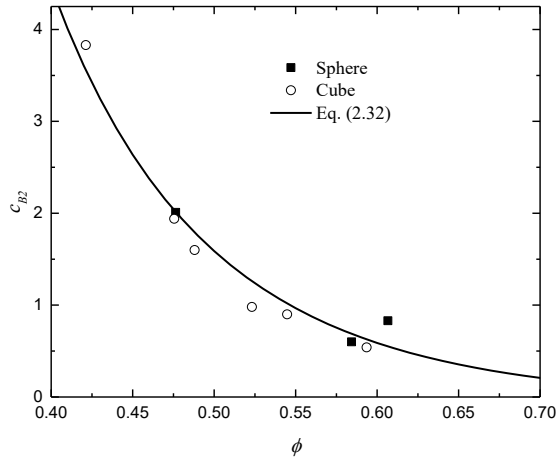


Figure 2.7.  $c_{B2}$  versus porosity  $\phi$  for different geometries of porous elements.

$c_{B2}$  for porous matrices composed of cubes or spheres can be approximated by the following correlation

$$c_{B2} = 0.79 \times \frac{(1-\phi)^2}{\phi^3}. \quad (2.32)$$

$c_{B2}$  approaches 0 as  $\phi$  increases asymptotically to 1, while it approaches infinity as  $\phi$  decreases asymptotically to 0. Eqs. (2.31) and (2.32) are the fitting formulas that best fit the DNS results. Only two geometries of the porous elements are considered in this study. Our numerical results show that values of  $c_{B1}$  and  $c_{B2}$  are not affected significantly when the pore-scale geometry is changed.

## 2.6 Conclusions

A PSPH model for flows in porous media is proposed based on the PSPH, which states that the characteristic length scale for flows in porous media is the pore size. The porosity and the permeability are assumed constant, which corresponds to the assumption that the considered porous media are isotropic and homogeneous. Volume-averaging is applied to the Navier-Stokes equations. The Darcy–Forchheimer term is adopted to approximate the total drag when it is far away from the wall boundary. Near the wall boundary, the effects of macroscopic velocity gradients are modeled with a Laplacian term in the macroscopic momentum equation. The local Reynolds number  $Re_d = \frac{K|s_{Dij}|}{\nu}$ , which describes the strength of the local momentum dispersion, is introduced using the pore size (identified by  $\sqrt{K}$ ) as the characteristic length and the mixing velocity,  $\sqrt{K}|s_{Dij}|$ , as the characteristic velocity. The effective viscosity is expanded as a Taylor series with respect to  $Re_d$ . The model coefficients are determined by fitting the DNS results for flows in a wall-bounded porous medium made of the REV. The coefficients are expected to be only related to the geometry of the REV.

# Chapter 3

## Numerical methods

### 3.1 Introduction

In this study, a finite-volume method (FVM) and a Lattice-Boltzmann method (LBM) are employed. The FVM is used in macroscopic simulations. The LBM is used for the DNS, which approximates the solution of the Navier-Stokes equations by computing particle distributions. These two methods are introduced in detail in this chapter.

### 3.2 Finite volume method

The FVM is used for solving the macroscopic equations (2.9)-(2.10). The FVM is used to discretize the partial differential equations in space and thus approximate the solution. The values located in each grid point surrounded by a small cell are calculated on a meshed geometry. Therefore, the FVM could handle irregular geometries. Besides, the FVM can conserve the variables on the coarse mesh easily, which is important in many physical problems. The solver is developed based on the open source computational fluid dynamics (CFD) code OpenFOAM 18.12.

#### 3.2.1 Gauss integral theorem

Eq. (3.1) is the momentum conservation.

$$\frac{\partial u_{Di}}{\partial t} + \frac{\partial (u_{Di}u_{Dj}/\phi)}{\partial x_j} = -\frac{1}{\rho} \frac{\partial (\phi \langle p \rangle^i)}{\partial x_i} + \phi g_i - \phi R_i + \frac{\partial D_{ij}}{\partial x_j}. \quad (3.1)$$

Integrating this equation over a spatially fixed control volume  $V$ , leads to

$$\frac{1}{V} \int_V \frac{\partial u_{Di}}{\partial t} dV + \frac{1}{V} \int_V \frac{\partial (u_{Di}u_{Dj}/\phi)}{\partial x_j} dV = -\frac{1}{V} \int_V \frac{1}{\rho} \frac{\partial (\phi \langle p \rangle^i)}{\partial x_i} dV + \frac{1}{V} \int_V \phi g_i dV - \frac{1}{V} \int_V \phi R_i dV + \frac{1}{V} \int_V \frac{\partial D_{ij}}{\partial x_j} dV. \quad (3.2)$$

Gauss's theorem is used to transform volume integrals into surface integrals,

$$\int_V \nabla \cdot \varphi dV = \int_S \varphi \cdot \mathbf{n} dS, \quad (3.3)$$

$$\int_V \nabla \cdot (\mathbf{u}\varphi) dV = \int_S (\mathbf{u}\varphi) \cdot \mathbf{n} dS, \quad (3.4)$$

$$\int_V \nabla \cdot (\nabla\varphi) dV = \int_S \nabla\varphi \cdot \mathbf{n} dS. \quad (3.5)$$

Where  $S$  is the surface of volume  $V$  and  $\mathbf{n}$  is the unit vector normal to the surface  $S$ . Applying Gauss's theorem, Eq. (3.2) is formulated as

$$\frac{1}{V} \int_V \frac{\partial u_{Di}}{\partial t} dV + \frac{1}{V} \int_S u_{Di} u_{Dj} n_j / \phi dS = -\frac{1}{V} \int_S \frac{1}{\rho} \phi \langle p \rangle^i n_i dS + \phi g_i - \phi R_i + \frac{1}{V} \int_S \tilde{v} \frac{\partial u_{Di}}{\partial x_j} n_j dS. \quad (3.6)$$

### 3.2.2 Numerical scheme

To compute the variables at the surface of the control volume in Eq.(3.6), linear interpolation is applied as shown in Fig. 3.1 and Eq. (3.7).

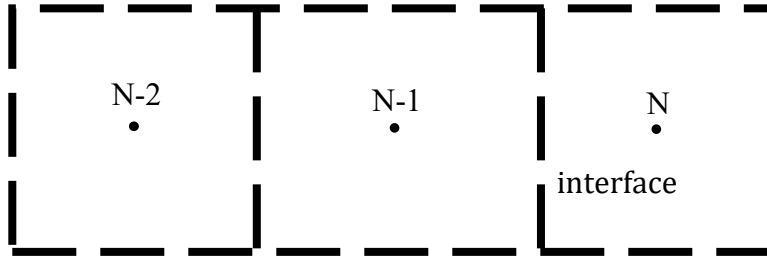


Figure 3.1. Interpolation stencils of face-neighboring cells

$$u_f = \frac{V_N}{V_{N-1}+V_N} u^{N-1} + \frac{V_{N-1}}{V_{N-1}+V_N} u^N \quad (3.7)$$

where the subscript  $f$  refers to the interface center and  $N$  denotes the number of cell centers.

### 3.2.3 Pressure-velocity coupling

The pressure at the new time level is determined by solving a Poisson equation. The time step is set to  $10^{-3}T$ . The velocity is corrected by the Pressure-Implicit scheme with Splitting of Operators (PISO) pressure-velocity coupling. In the following, the PISO method is introduced in detail.

According to Issa (1986), Eq. (3.6) can be changed into

$$\frac{\mathbf{u}^{n+1}-\mathbf{u}^n}{\Delta t} - H(\mathbf{u}^{n+1}) = -\frac{1}{\rho}\nabla p^{n+1} + \mathbf{g}. \quad (3.8)$$

Where  $n$  is the time step and  $H(\cdot)$  stands for the finite-difference representation of the spatial convective and diffusive fluxes of the momentum. The Euler implicit temporal difference scheme is applied. The tentative velocity field  $\mathbf{u}^*$  can be obtained by replacing unknown  $\nabla p^{n+1}$  by known  $\nabla p^n$  from the previous time step, as shown in Eqs. (3.9)-(3.10),

$$\frac{\mathbf{u}^*-\mathbf{u}^n}{\Delta t} - H(\mathbf{u}^*) = -\frac{1}{\rho}\nabla p^n + \mathbf{g}, \quad (3.9)$$

$$\mathbf{u}^* = \Delta t \left( -\frac{1}{\rho}\nabla p^n + \mathbf{g} + H(\mathbf{u}^*) \right) + \mathbf{u}^n. \quad (3.10)$$

However, the velocity  $\mathbf{u}^*$  doesn't satisfy the discretized continuity equation. Therefore, the first corrector step is applied. It's assumed that a new pressure field  $p^*$  and new velocity  $\mathbf{u}^{**}$  satisfy the following equations in the first corrector step

$$\nabla \mathbf{u}^{**} = 0, \quad (3.11)$$

$$\frac{\mathbf{u}^{**}-\mathbf{u}^n}{\Delta t} - H(\mathbf{u}^*) = -\frac{1}{\rho}\nabla p^* + \mathbf{g}. \quad (3.12)$$

By solving Eq. (3.11)-(3.12), the unknown variables  $p^*$  and  $\mathbf{u}^{**}$  can be obtained. In order to increase accuracy, the second corrector step is adopted. It is similar to the first corrector step. A new pressure field  $p^{**}$  and new velocity  $\mathbf{u}^{***}$  are assumed to satisfy the following equations

$$\nabla \mathbf{u}^{***} = 0, \quad (3.13)$$

$$\frac{\mathbf{u}^{***}-\mathbf{u}^n}{\Delta t} - H(\mathbf{u}^{**}) = -\frac{1}{\rho}\nabla p^{**} + \mathbf{g}. \quad (3.14)$$

In these equations, the velocity  $\mathbf{u}^{**}$  is obtained in the first corrector step. Therefore, there are only two unknown variables  $p^{**}$  and  $\mathbf{u}^{***}$  that can be obtained easily by solving Eqs.(3.13)-(3.14).

Although further corrector steps can be performed, the velocity  $\mathbf{u}^{***}$  meets the accuracy requirement and is used as the final solution in general.

The basic steps for PISO are summarized as follows:

- (1) Set the initial pressure field  $p^n$  and velocity field  $\mathbf{u}^n$ .
- (2) Solve the Eq. (3.10) to obtain the tentative velocity field  $\mathbf{u}^*$ .
- (3) The first corrector step:
  - (a) Solve the Eqs. (3.11)-(3.12) to update the pressure field.
  - (b) Correct the velocity field by Eq. (3.12).
- (4) The second corrector step:
  - (a) Repeat the first corrector step by Eqs. (3.13)-(3.14) to obtain the pressure field  $p^{**}$ .
  - (b) Correct the velocity field by Eq. (3.14) for the velocity field  $\mathbf{u}^{***}$ .
- (5) Return to step (1) until convergence.

### 3.3 Lattice-Boltzmann method

Unlike the traditional FVM, which focuses on the conservative form of nonlinear partial differential equations, LBM statistically models the particle streaming along with the fixed directions and the collision at the lattice site. The fictive particles simulate the fluid by performing consecutive propagation and collision processes. The explicit character of the LBM facilitates the parallel processing computation. On top of that, the LBM can deal with complicated boundary conditions well. The bounce-back model applied in non-slip wall conditions contributes to the accuracy. In this thesis, the LBM is used to compute the velocity field by fully resolving the fluid flow in the porous media. This is equivalent to resolving the Navier—Stokes equations with no-slip boundary conditions at the solid matrix. The results are used to determine the model coefficients and obtain the validation data.

### 3.3.1 The Boltzmann equation

The LBM method approximates the continuous Boltzmann equation by discretizing physical space with uniformly lattice nodes and velocity space by the probability of particles. The basic equation for the LBM is made up of the distribution function  $f(\mathbf{r}, \mathbf{c}, t)$  and collision operator  $\Omega$ , which reads (see Aidun & Clausen, 2009)

$$\frac{\partial f}{\partial t} + \mathbf{c} \cdot \nabla f = \Omega. \quad (3.15)$$

$f(\mathbf{r}, \mathbf{c}, t)$  is the probability of particles with velocities between  $\mathbf{c}$  and  $\mathbf{c} + d\mathbf{c}$ , positioned between  $\mathbf{r}$  and  $\mathbf{r} + d\mathbf{r}$  at time  $t$ . The collision term  $\Omega$  is the function of  $f(\mathbf{r}, \mathbf{c}, t)$  and needs to be determined before the Boltzmann equation is solved.

A simplified model named BGK operator approximating the collision operator  $\Omega$  is introduced by Bhatnagar et al. (1954).

$$\Omega = \frac{1}{\tau} (f^{eq} - f). \quad (3.16)$$

$\tau$  is the relaxation factor and determines the viscosity of the fluid.  $f^{eq}$  is the collision distribution function which originates from the normalized Maxwell's distribution function.

Submitting Eq. (3.16) into Eq. (3.15), the basic equation becomes

$$\frac{\partial f_i}{\partial t} + \mathbf{c}_i \nabla f_i = \frac{1}{\tau} (f_i^{eq} - f_i). \quad (3.17)$$

$i$  denotes the streaming direction of the particles. Eq. (3.17) can be further simplified as

$$f_i(\mathbf{r} + \mathbf{c}_i \Delta t, t + \Delta t) = f_i(\mathbf{r}, t) + \frac{\Delta t}{\tau} [f_i^{eq}(\mathbf{r}, t) - f_i(\mathbf{r}, t)]. \quad (3.18)$$

In this discrete equation, the left-hand side represents the streaming process, while the right-hand side denotes the collision process. The simplicity of LBM promotes its wide applications for many fluid mechanics problems. With the help of the Chapman–Enskog expansion (Chen & Doolen, 1998), the compressible Navier–Stokes equations can be derived from the Lattice Boltzmann equation. Eq. (3.18) is equivalent to the compressible Navier–Stokes equations (2.2)–(2.3) for small Mach numbers, *i.e.* for small compressibility of the fluid (Chen & Doolen, 1998).

In this study, the D3Q19 grid is shown in Fig. 3.2. D3 stands for 3 dimensions while Q19 denotes 19 discrete velocities. In each time step, a particle travels from one grid point to a neighboring grid point. The probability  $f_i$  is gotten by Eq. (3.18) where  $f_i^{eq}$  is read by

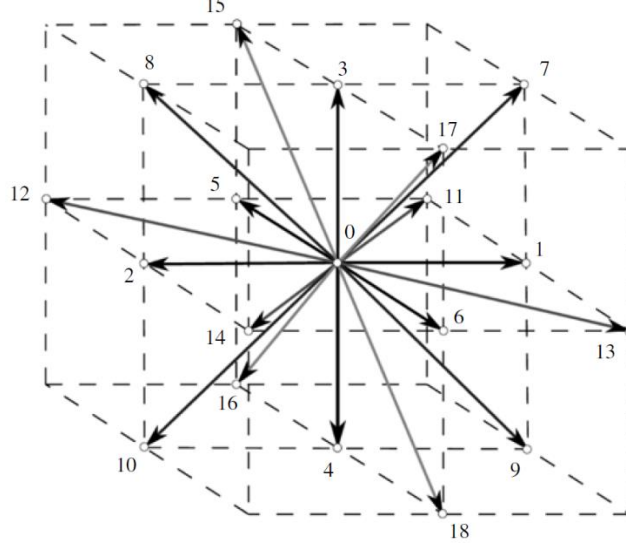


Figure 3.2. Grid structure and velocities with the D3Q19 discretization (Jin *et al.* 2015).

$$f_i^{eq}(\mathbf{r}, t) = w_i \rho(\mathbf{r}, t) \left[ 1 + \frac{\mathbf{c}_i \cdot \mathbf{u}}{c_s^2} + \frac{1}{2} \frac{(\mathbf{c}_i \cdot \mathbf{u})^2}{c_s^4} - \frac{1}{2} \frac{\mathbf{u}^2}{c_s^2} \right]. \quad (3.19)$$

Where  $\mathbf{u}$  is the macroscopic velocity of the node,  $c_s = \frac{c_i}{\sqrt{3}}$  is the lattice speed of sound.  $w_i$  is the weight factor for  $i^{\text{th}}$  direction,  $w_0 = 0$  for the original grid point,  $w_i = \frac{1}{18}$  ( $1 \leq i \leq 6$ ) for particles streaming to the face-connected neighbors and  $w_i = \frac{1}{36}$  ( $7 \leq i \leq 18$ ) for particles streaming to the edge-connected neighbors. The variables from the Navier-Stokes equations can be obtained by computing the probability  $f(\mathbf{r}, \mathbf{c}, t)$ , as follows

$$\rho(\mathbf{r}, t) = \sum_{i=0}^{18} f_i(\mathbf{r}, \mathbf{c}, t), \quad (3.20)$$

$$\mathbf{u}(\mathbf{r}, t) = \frac{1}{\rho(\mathbf{r}, t)} \sum_{i=0}^{18} \mathbf{c}_i f_i(\mathbf{r}, \mathbf{c}, t). \quad (3.21)$$

Eqs. (3.20) and (3.21) are respectively conservation of mass and of momentum.

The basic steps for LBM are summarized as follows:

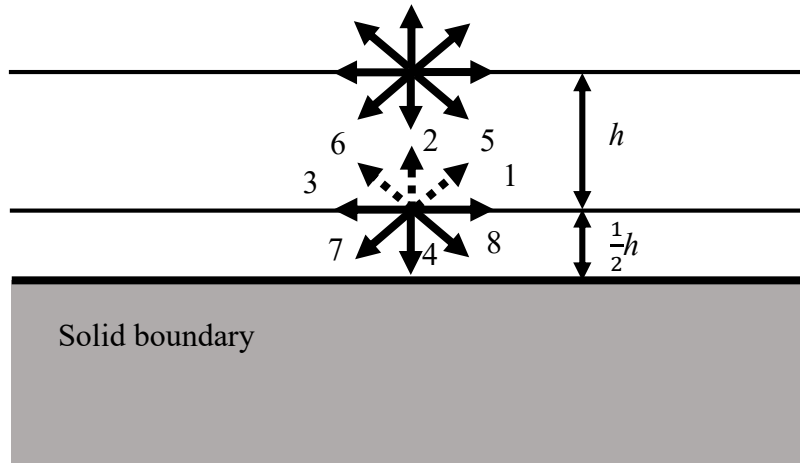
- (1) Set the initial  $\rho(\mathbf{r}, t)$ ,  $\mathbf{u}(\mathbf{r}, t)$ ,  $f_i(\mathbf{r}, t)$  and  $f_i^{eq}(\mathbf{r}, t)$ .

- (2) Streaming step: obtain  $f_i(\mathbf{r} + \mathbf{c}_i\Delta t, t + \Delta t)$  in the direction of  $\mathbf{c}_i$ .
- (3) Compute macroscopic variables  $\rho(\mathbf{r}, t + \Delta t)$  and  $\mathbf{u}(\mathbf{r}, t + \Delta t)$  by Eqs.(3.20)-  
(3.21)
- (4) Compute  $f_i^{eq}(\mathbf{r}, t + \Delta t)$  by Eq. (3.19).
- (5) Collision step: update the particle distribution  $f_i(\mathbf{r} + \mathbf{c}_i\Delta t, t + \Delta t)$  by Eq.  
(3.18).
- (6) Return to step (2) and repeat steps (2)-(5).

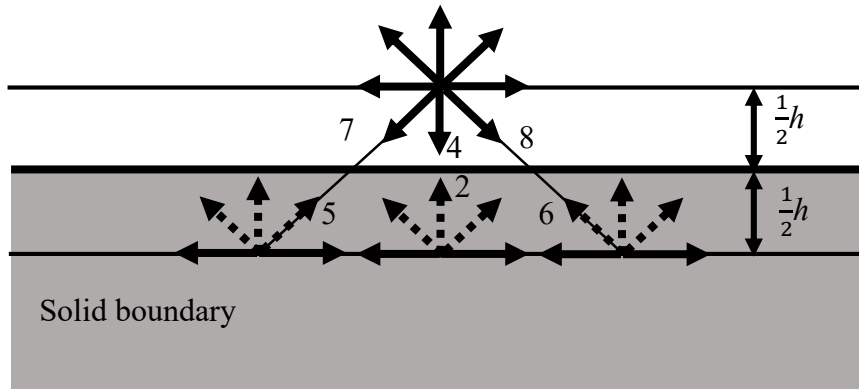
### 3.3.2 Boundary conditions

In order to enforce the no-slip boundary condition at the solid walls, the halfway bounce back model is applied in the LBM. In this model, the particles are bounced back to the flow domain without any loss of mechanical energy when they collide with a wall. This model ensures the conservation of mass and momentum at the boundary (Mohamad, 2011).

In this study, two schemes of the bounce-back model are applied: bounce-back scheme I and bounce-back scheme II, as shown in Fig. 3.3. For bounce-back scheme I, the wall is located at half the distance from the lattice sites.  $f_7$ ,  $f_4$  and  $f_8$  are known from the streaming process. It's assumed that the particles hit the wall then bounce back into the streaming process. Therefore,  $f_5 = f_7$ ,  $f_2 = f_4$ , and  $f_6 = f_8$ . Bounce-back scheme I is widely applied in the external boundary, such as flat walls and channel surfaces. For bounce-back scheme II, the wall is located between the lattice sites. According to the bounce back assumption,  $f_5 = f_7$ ,  $f_2 = f_4$ , and  $f_6 = f_8$  while  $f_7$ ,  $f_4$  and  $f_8$  are equal to the probability of the corresponding neighbor node by streaming. Bounce-back scheme II provides better performance when dealing with the internal boundary, such as the porous matrix in fluid flow. Both schemes give second-order numerical accuracy (Mohamad, 2011).



(a)



(b)

Figure 3.3. (a) bounce back scheme I; (b) bounce back scheme II .

Both the FVM and LBM solvers used in this thesis have received intensive validations and verifications in the previous studies (Jin *et al.*, 2015, 2017; Uth *et al.*, 2016). Therefore, these numerical methods are directly used in this study. The DNS solutions can be used to validate the model results. Typical DNS cases are calculated using different meshes to estimate the uncertainty of the DNS solutions due to mesh dependence. This will be discussed in the following chapters when the numerical results are discussed.

### 3.4 Conclusions

The basic equations of FVM and LBM are presented in this chapter. The FVM discretizes the macroscopic equations including the temporal and spatial terms with linear interpolation and PISO algorithms. The LBM indirectly solves discretized form of the Boltzmann equation which is an

approximation to solving the incompressible Navier—Stokes equations. The bounce-back model is applied to achieve second-order numerical accuracy. Both methods complement each other for verification and validation.

# Chapter 4

## Flows in a porous medium bounded by walls

### 4.1 Introduction

To validate the PSPH model developed in the previous chapter, macroscopic simulations and DNS are performed to calculate flows in porous media in a wide range of Reynolds numbers, Darcy numbers, and porosities. The macroscopic equations are solved with the FVM while the microscopic equations (DNS) are solved with the LBM. The test cases shown here are about flows in a channel occupied by a regular porous matrix of spheres or cubes. Flows in porous channels are relevant to various fields, such as oil and flow in the reservoir, compact heat exchangers, geothermal power plants, grain storage, heat sinks, and waste management (Nield and Bejan; 2017, Vafai 2015; Ingham and Pop, 1998). The model results and DNS results are compared to validate the developed macroscopic PSPH model.

### 4.2 Test cases in the study

#### 4.2.1 Geometry of the porous matrix

The porous matrices are composed of 3-dimensional aligned-distributed spheres or cubes in the DNS cases, as shown in Fig. 4.1 (a-b). The wall boundary condition is imposed in the Y direction. Periodic boundary conditions are applied in the other two directions. The whole domain consists of 128 ( $4s \times 8s \times 4s$ ) REV's. The governing equations (2.2-2.3) are solved. In the macroscopic simulation, the geometry is as same size as in the DNS simulation but without porous matrix, because the porous matrix is modeled. The governing equations (2.9-2.10) with the PSPH model are used.

The purpose of this test cases is to show that the PSPH model can be used for wide ranges of Darcy numbers ( $Da$ ) and Reynolds numbers ( $Re_{cl}$ ). The Reynolds number  $Re_{cl}$  is based on the half channel height  $H$  and the centerline velocity in the channel  $u_{cl}$ , and is defined as

$$Re_{cl} = \frac{u_{cl}H}{\nu} \quad (4.1)$$

The Darcy number is the ratio of the permeability to its cross-sectional area, and is defined as

$$Da = \frac{K}{H^2} \quad (4.2)$$

The main parameters for DNS cases and macroscopic simulation cases are given in Table 4.1 and 4.2, respectively.

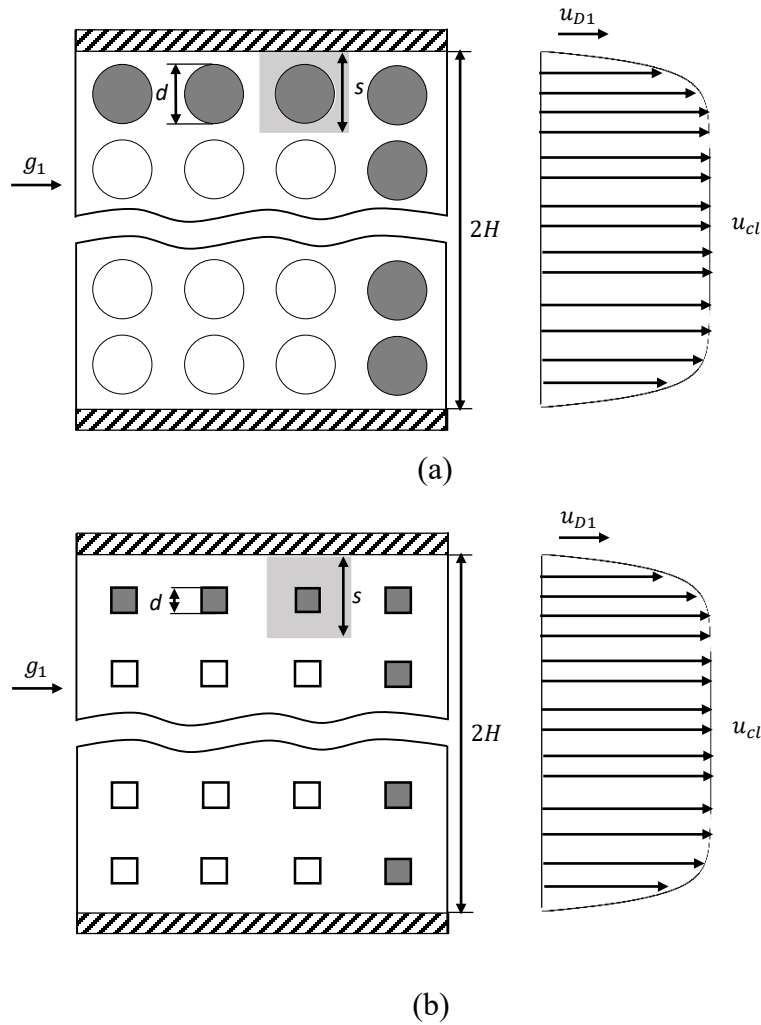


Figure 4.1. Schematic geometry of the porous matrix. (a) The porous matrices made of 3-dimensional aligned-distributed spheres for DNS; (b) the porous matrices made of 3-dimensional aligned-distributed cubes for DNS.

Porous matrix	$\phi$	Mesh resolution	$Re_p$	$Re_K$
“spheres”	0.48-0.84	$161 \times 321 \times 161$	13-512	0.8-53
		$481 \times 961 \times 481$		
“cubes”	0.42-0.81	$193 \times 385 \times 193$	20-700	0.8-43
		$561 \times 1121 \times 561$		

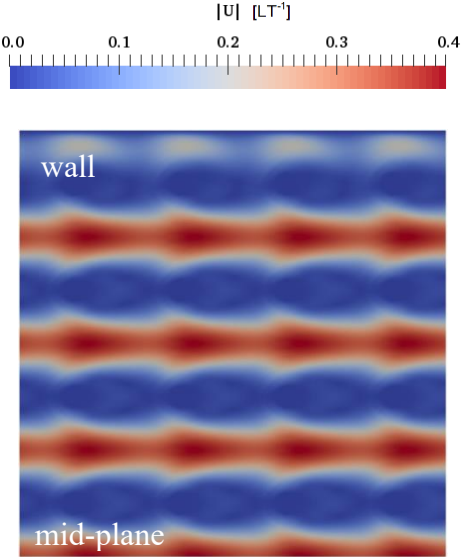
Table 4.1. Main parameters for the DNS cases, LBM. The characteristic velocity of Reynolds numbers is from the first REV near the wall boundary. The lowest and highest mesh resolutions employed for each porous matrix are shown.

Porous matrix	$\phi$	$Da$	Mesh resolution	$Re_p$	$Re_K$
“spheres”	0.48-0.84	$4.0 \times 10^{-5}$ -	$161 \times 321 \times 161$	13-498	0.8-50
		$5.0 \times 10^{-4}$			
“cubes”	0.42-0.81	$2.1 \times 10^{-5}$ -	$161 \times 321 \times 161$	20-700	0.8-43
		$3.4 \times 10^{-4}$			

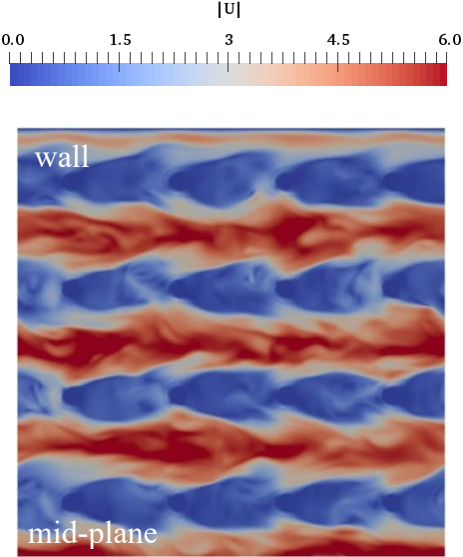
Table 4.2. Main parameters for the cases of macroscopic simulation, FVM. The characteristic velocity of Reynolds numbers is from the area of the same size as the first REV near the wall boundary.

### 4.2.2 Instantaneous flow fields

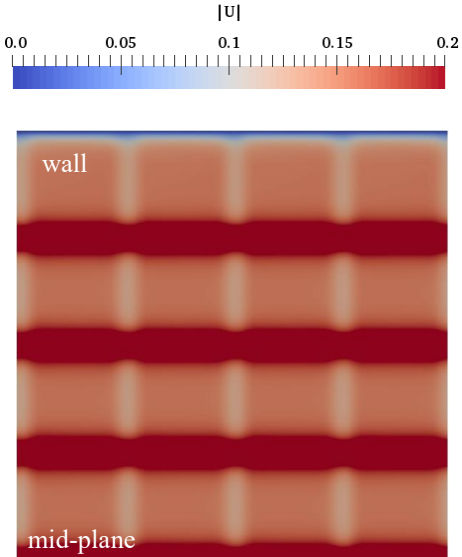
The instantaneous velocity magnitudes for representative Reynolds numbers are shown in Fig. 4.2. It may also be observed that the first REV next to the wall is mainly affected.



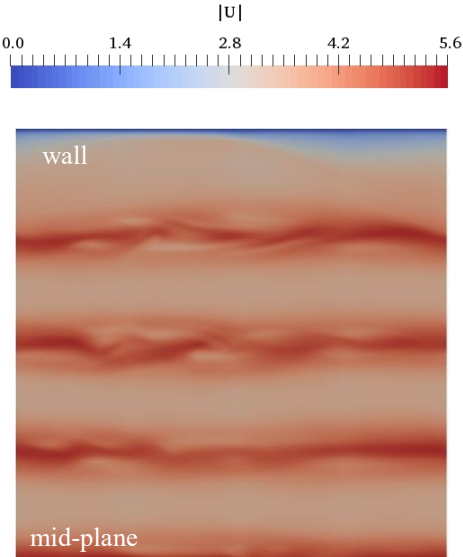
(a)



(b)



(c)



(d)

Figure 4.2. Instantaneous velocity magnitude. In (a) and (b), the porous matrix is composed of spheres,  $\phi = 0.48$ . (a)  $Re_{cl}=98$ , laminar; (b)  $Re_{cl}=1730$ , turbulent. In (c) and (d), the porous matrix is composed of cubes,  $\phi = 0.49$ . (c)  $Re_{cl}=127$ , laminar; (d)  $Re_{cl}=2339$ , turbulent.

### 4.2.3 Statistical results

I fix the half channel size  $H$  and reduce the pore size  $s$ , which results in three different scale ratios ( $H/s$ ): 20, 30, and 40. The corresponding Darcy numbers are  $8.5 \times 10^{-6}$ ,  $3.8 \times 10^{-6}$ , and  $2.1 \times 10^{-6}$ , respectively. Fig. 4.3 shows that the distribution of  $u_{D1}$  is steeper near the wall when  $Da$  is smaller. The results of  $u_{D1}$  from the PSPH model and DNS are averaged in each REV, so they can be compared quantitatively. The symbol  $\langle \dots \rangle^v$  in Fig. 4.3 denotes the whole REV-averaged velocity  $\langle u_{D1} \rangle^v$  obtained from DNS and PSPH model results. It can be seen that the results from the PSPH model are in good agreement with the DNS results.

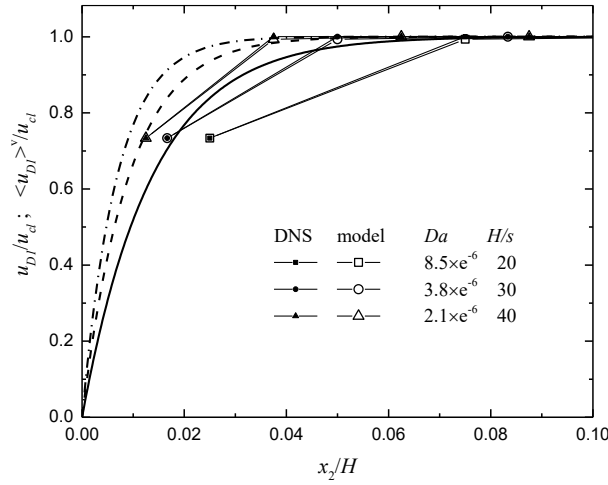


Figure 4.3.  $u_{D1}/u_{cl}$  and  $\langle u_{D1} \rangle^v/u_{cl}$  versus the normalized distance from the wall  $x_2/H$ . The porous matrix is composed of cubes,  $\phi = 0.49$ ,  $Re_{cl} = 127$ . Lines:  $u_{D1}/u_{cl}$  obtained from continuous PSPH model results; hollow symbols:  $\langle u_{D1} \rangle^v/u_{cl}$  from REV-averaged PSPH model results; solid symbols:  $\langle u_{D1} \rangle^v/u_{cl}$  from REV-averaged DNS results.

The numerical results in Fig. 4.3 are shown again in Fig. 4.4 but the distance from the wall  $x_2$  is normalized with the pore size  $s$  instead of  $H$ . The DNS results from the two mesh resolutions are almost identical, indicating the mesh independence of the DNS solution. The profiles of  $u_{D1}$

collapse to a single curve, suggesting that the characteristic length of the flow is  $s$ ; this is in accordance with the PSPH. Figure 4.4 also shows that the PSPH momentum-dispersion model is more accurate than the macroscopic model using Brinkman's expression (Brinkman, 1947) or Ochoa-Tapia and Whitaker's expression (Ochoa-Tapia & Whitaker, 1995). It can be seen that the results for the laminar flow are mesh-independent.

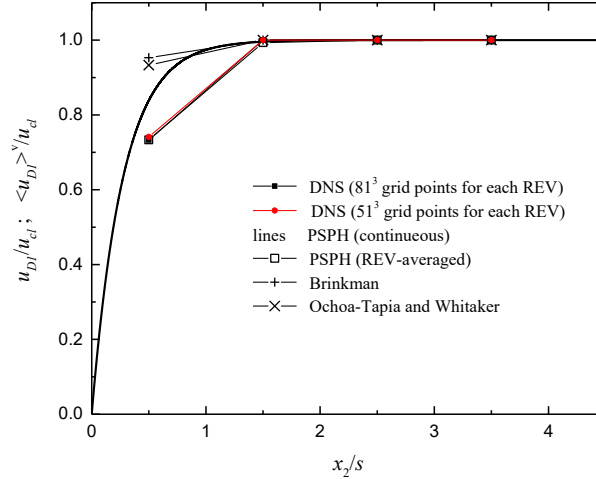
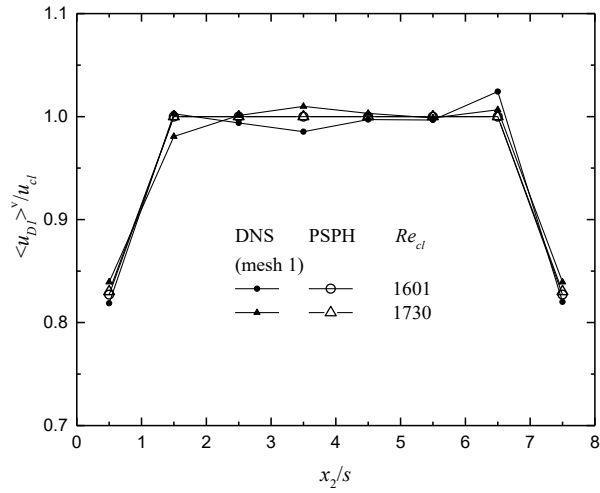
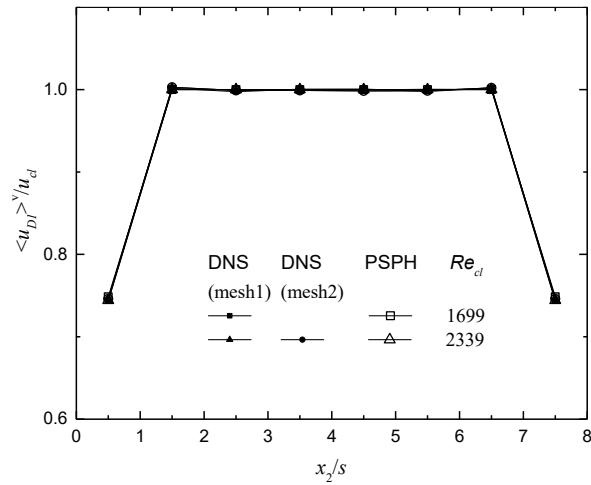


Figure 4.4.  $u_{D1}/u_{cl}$  and  $\langle u_{D1} \rangle^v/u_{cl}$  versus the normalized distance from the wall  $x_2/s$ . The porous matrix is composed of cubes,  $\phi = 0.49$ ,  $Re_{cl} = 127$ .

Different Reynolds numbers  $Re_{cl}$  can be obtained by changing the applied pressure gradient  $g_1$ . Fig. 4.5 shows the results for different values of  $Re_{cl}$  in the turbulent regime. Due to the turbulent instability, there are some perturbations of the velocity for the porous medium composed of spheres, this is also observed in Jin and Kuznetsov (2017). These perturbations are not found for the porous medium composed of cubes. The profiles of  $u_{D1}$  for different values of  $Re_{cl}$  collapse to a single curve when they are normalized with  $u_{cl}$ . The DNS results are mesh-independent, see Fig. 4.5b. The model results for both porous matrices are in good agreement with the DNS results.



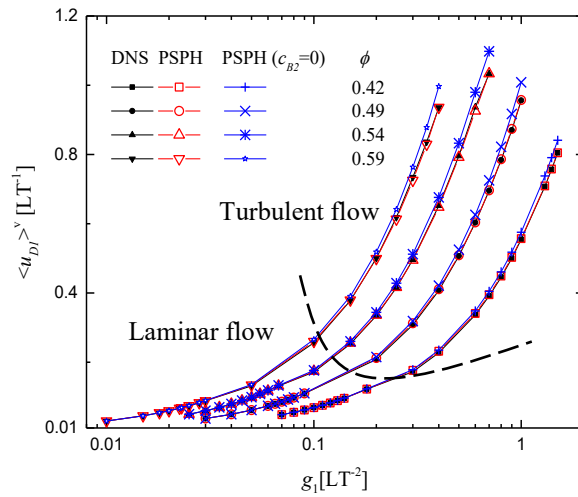
(a)



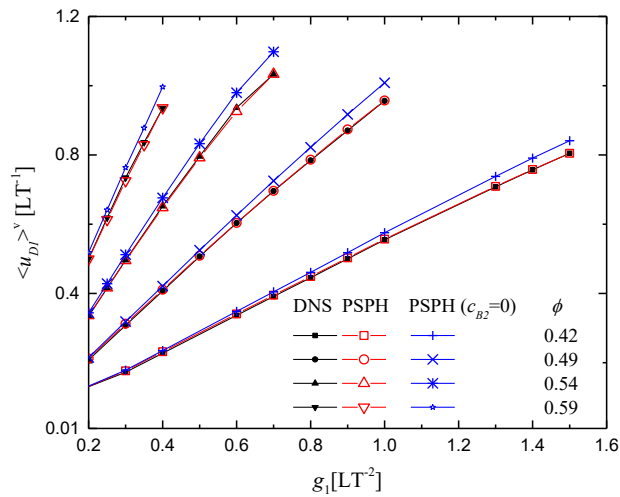
(b)

Figure 4.5. Streamwise velocity  $\langle u_{D1} \rangle^v$  versus the normalized distance from the wall  $x_2/s$  for different values of  $Re_{cl}$ . The porous matrix is composed of spheres (a) and cubes (b). Hollow symbols: PSPH model results; solid symbols: DNS results. Mesh1:  $101^3$  grid points for each REV; mesh 2:  $76^3$  grid points for each REV.

It can be also seen in Fig. 4.5 that, for the porous matrix under consideration, the wall only affects the flow in the first REV next to it. Therefore, in Fig. 4.6, I only compare the macroscopic and microscopic results for volume-averaged value of  $u_{D1}$  in the first REV next to the wall.  $c_{B2}$  has non-negligible effects when the flow has a large Reynolds number, particularly when the flow is turbulent, see Fig. 4.6 (b). The value of  $u_{D1}$  next to the wall may be over-predicted by 10% if  $c_{B2}$  is neglected.



(a)



(b)

Figure 4.6.  $\langle u_{D1} \rangle^v$  in the first REV next to the wall versus the applied pressure gradient  $g_1$ . The porous matrix is composed of cubes. (a) the whole range of values of the applied pressure gradient; (b) zoomed results in the turbulent regime.

### 4.3 Conclusions

The proposed macroscopic equations are used to simulate the flows in a porous medium bounded by two walls. More simulation cases with the laminar and turbulent flow are performed apart from the cases in chapter 2. The model results are in good agreement with the DNS results in wide ranges of the Reynolds number, Darcy number, and porosity. The study shows that the effects of macroscopic velocity gradient on momentum transport in porous media can be reasonably well approximated using a Laplacian term.

# Chapter 5

## Flows in a porous medium with two different porosities

### 5.1 Introduction

The flow in a porous medium with two different porosities is simulated to further validate the adequacy of the PSPH model. Since chapter 4 is dedicated to the interface between the porous medium and the wall (the porosity is 0), this chapter focuses on the interface between different porosities, which is more common in nature. Various Reynolds numbers, Darcy numbers, and porosity values are used in the study. The Navier-stokes equations are solved indirectly using the LBM to get the microscopic DNS results accounting for the detailed geometry of the porous matrix. The macroscopic equations solved with the FVM are applied to get the macroscopic results taking into account the model of the porous matrix. The DNS results and macroscopic results are compared.

### 5.2 Test cases in the study

#### 5.2.1 Geometry of the porous matrix

To further investigate the generality of the proposed PSPH model, flows in porous media consisting of two regions with different porosities are simulated. The geometry of the porous matrix is shown in Fig. 5.1. A constant pressure gradient  $g_1$  forces the fluid to flow with two different characteristic velocities. The zone with a higher porosity has a higher velocity. Therefore, this type of flow has two characteristic Reynolds numbers based on the pore size  $s$ , calculated as

$$Re_1 = \frac{u_a s}{\nu}; Re_2 = \frac{u_b s}{\nu}. \quad (5.1)$$

where  $u_a$  and  $u_b$  are the macroscopic velocities in the two porous medium zones far away from the interface. The computational domain is composed of 128 ( $4 \times 8 \times 4$ ) REV's. The two porous medium regions have the same pore size  $s$ , but different sizes of solid elements ( $d_1$  and  $d_2$ ), leading to two different porosities  $\phi_1$  and  $\phi_2$ . Up to 434 million grid points were used to simulate turbulent

flows (each REV has  $151^3$  points). The main parameters for DNS cases and macroscopic simulation cases are shown in Table 5.1.

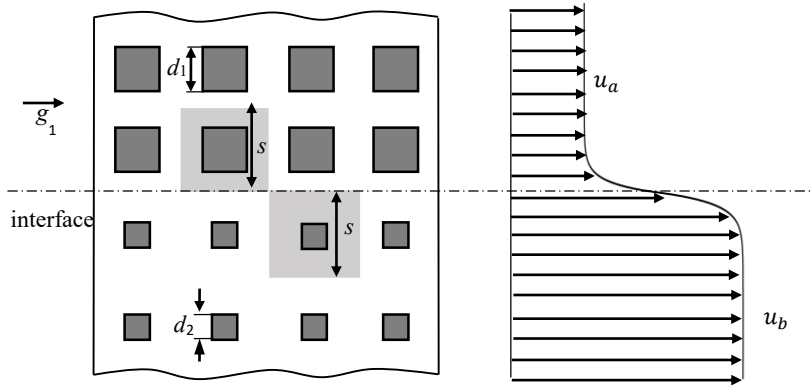


Figure 5.1. Schematic geometry of a porous matrix with two porosities for microscopic simulation.

Porous matrix	Method	$\phi$	Mesh resolution	$Re_p$	$Re_K$
“cubes”	LBM	0.42-0.54	$313 \times 625 \times 313$	32-1193	1.0-66
			$601 \times 1201 \times 601$		
“cubes”	FVM	0.42-0.54	$161 \times 321 \times 161$	33-1158	1.0-64

Table 5.1. Main parameters for the DNS cases and the macroscopic simulation. The characteristic velocity of Reynolds numbers is from the first REV or the area of the same size as the first REV near the interface. The lowest and highest mesh resolutions for each porous matrix are shown.

### 5.2.2 Instantaneous flow fields

Typical laminar and turbulent flows in this porous medium are shown in Fig. 5.2. The porosities of the two distinct regions are  $\phi_1 = 0.42$  and  $\phi_2 = 0.49$ , respectively. It can be seen that the effects of the interface are limited to the two REV's in the vicinity of the interface.

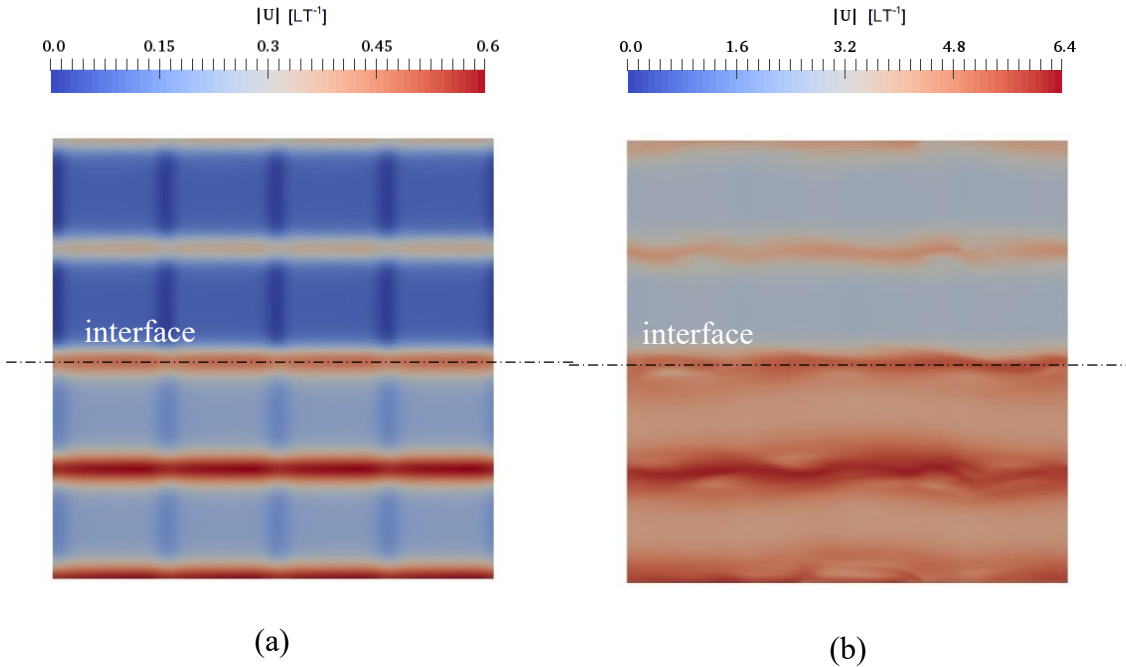
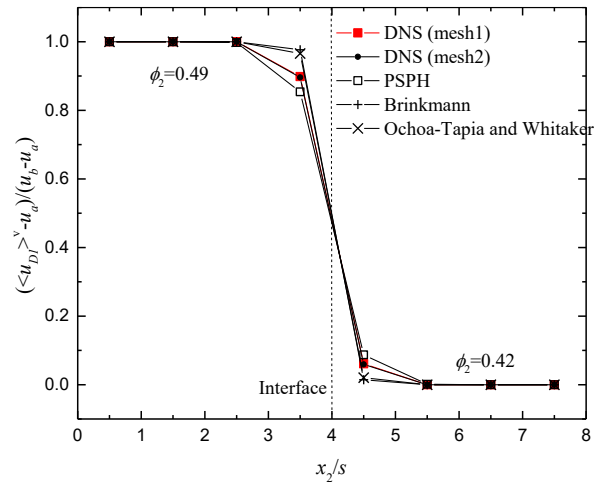


Figure 5.2. Instantaneous velocity magnitude. The porous matrix is composed of cubes,  $\phi_1 = 0.42$ ,  $\phi_2 = 0.49$ . (a)  $Re_1 = 30$  and  $Re_2 = 60$  (laminar flow); (b)  $Re_1 = 454$  and  $Re_2 = 860$  (turbulent flow).

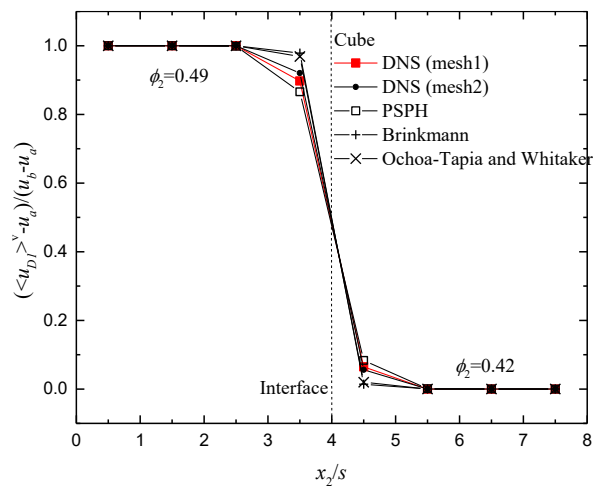
### 5.2.3 Statistical results

Figure 5.3 shows the velocity profiles in the wall normal direction for  $g_1 = 0.07$  and  $g_1 = 1.1$ . Both laminar and turbulent cases are calculated using a lower-resolution mesh (each REV has  $91^3$  points). It can be seen that the results for the laminar flow are mesh-independent. The results for the turbulent flow are slightly mesh-dependent. The PSPH model results are compared with the microscopic DNS results. It can be seen that the PSPH model is more accurate than the macroscopic model with Brinkman's expression (Brinkman, 1947) or Ochoa-Tapia and Whitaker's expression (Ochoa-Tapia & Whitaker, 1995). When the mesh resolution is improved, the DNS results become

closer to the PSPH-model results. Higher mesh resolution is impossible to carry on since DNS is too expensive.



(a)

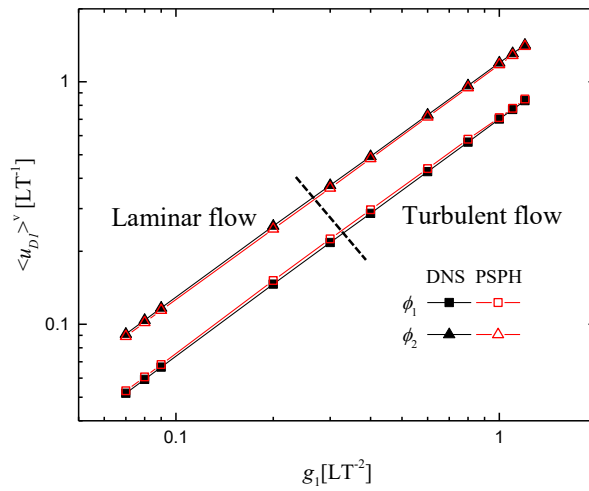


(b)

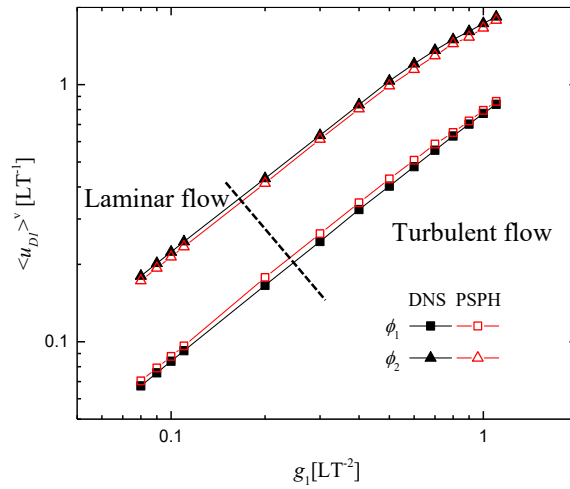
Figure 5.3. REV-averaged streamwise velocity  $\langle u_{D1} \rangle^v$  versus the normalized distance from the wall  $x_2/s$ . The porous matrix is composed of cubes,  $\phi_1 = 0.42$ ,  $\phi_2 = 0.49$ . (a)  $Re_1 = 30$ ,  $Re_2 =$

60 (laminar flow); (b)  $Re_1 = 454, Re_2 = 860$  (turbulent flow). Mesh1:  $151^3$  grid points for each REV; mesh 2:  $91^3$  grid points for each REV.

The results for more values of  $g_1$  and  $\phi$  are shown in Fig. 5.4. This figure depicts the values of  $\langle u_{D1} \rangle^v$  in two REVs adjacent to the interface. It can be seen that the PSPH model can be used in a wide range of flow conditions, including both laminar and turbulent flows. In general, the errors in velocity distributions predicted by the model for all conditions simulated here are small. The deviation of model predictions from DNS results may increase when the difference between the two porosities increases. The deviation may be related to the errors of both the PSPH model and Darcy-Forchheimer model.



(a)



(b)

Figure 5.4.  $\langle u_{D1} \rangle^v$  in the first REV adjacent to the interface versus applied pressure gradient  $g_1$ . (a) Cubes,  $\phi_1 = 0.42$  and  $\phi_2 = 0.49$ ; (b) cubes,  $\phi_1 = 0.42$  and  $\phi_2 = 0.54$ .

### 5.3 Conclusions

A series of cases to simulate the flows in a porous medium with two porosities are performed by solving the macroscopic equations and the microscopic equations (DNS). The results show that the interface mainly affects the first REV next to it. The comparisons between the macroscopic results and the DNS results in wide ranges of the Reynolds number, Darcy number, and porosity validate the proposed PSPH model.

# Chapter 6

## Flows in a porous medium with two length scales

### 6.1 Introduction

The flow in a porous medium with two length scales is simulated in order to expand the validation of the PSPH model. While chapters 4-5 are dedicated to porous medium with only one length scale (the pore size), this chapter is devoted to the double-length scales which are often found in porous canopies made of trees, vegetation, or buildings (Meroney, 2007). The large-scale and small-scale porous matrices are both taken into account in DNS simulation cases. In macroscopic simulation cases, the large-scale porous matrix is accounted for, while the small-scale one is modeled by the geometric parameters. The comparisons between DNS results and macroscopic results are presented.

### 6.2 Test cases in the study

#### 6.2.1 Geometry of the porous matrix

In the DNS simulation, the porous matrices are composed of 3-dimensional aligned-distributed spheres with the element size  $d_s$  and spacing  $s_s$  and 2-dimensional staggered-distributed bars with the element size  $d_l$  and spacing  $s_l$ , as shown in Fig. 6.1 (a-b). The computational domain is a representative elementary volume (REV) for the large porous element. The ratio between the large pore size  $s_l$  and the bar size  $d_l$  has a fixed value ( $s_l/d_l = 2$ ). The whole domain consists of 256 ( $8s_s \times 8s_s \times 4s_s$ ) REVs for small porous elements. The periodic boundary condition is applied in all directions. The governing equations (2.2-2.3) are solved.

The porous matrices are made of the same large porous elements (staggered bars), but different numbers of REVs, which have been studied in Jin *et al.* (2015). The numerical results show that the computational domain in this study is large enough to calculate the length scale of turbulence at the center of a REV accurately (Jin *et al.*, 2015).

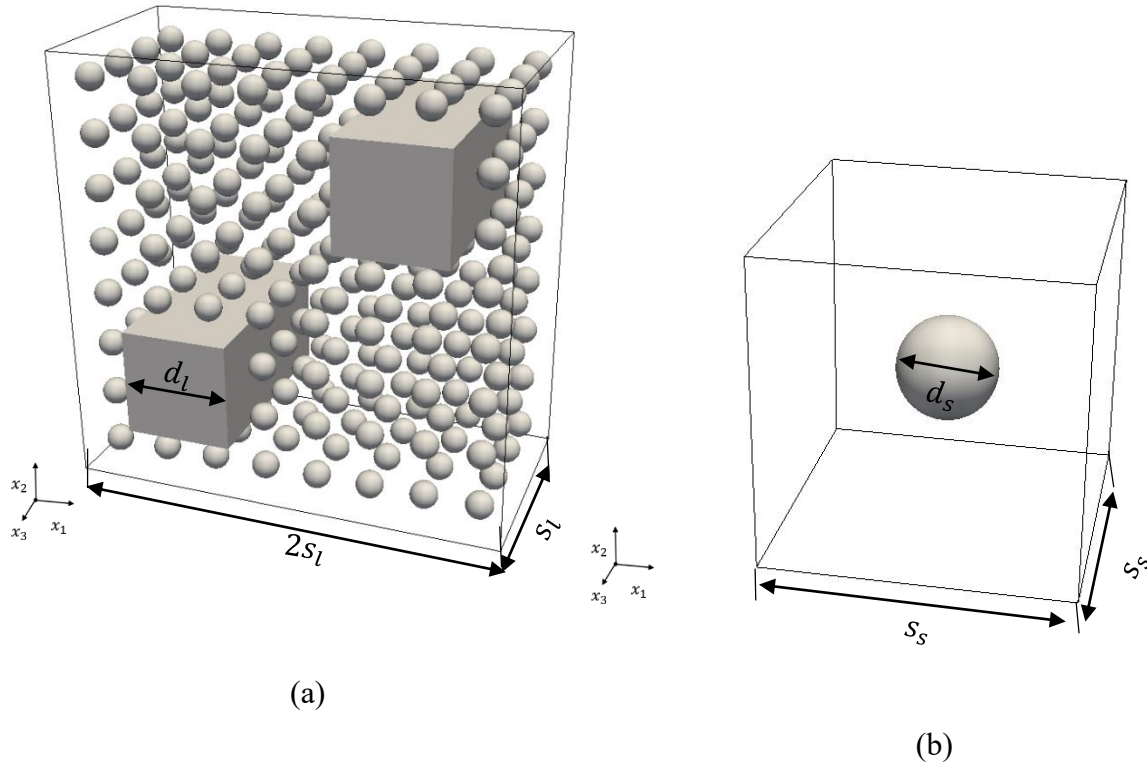


Figure 6.1. Porous matrices used in the DNS study. (a) A porous matrix with two length scales (made of spheres); (b) a REV for the small porous element.

The flow is imposed in  $x_1$ - direction. The Reynolds numbers for the large and small elements are defined as

$$Re_s = \frac{u_m d_s}{\nu}; \quad Re_l = \frac{u_m d_l}{\nu}. \quad (6.1)$$

where  $u_m$  is the mean seepage velocity.

Here  $\phi_s$  denotes the porosity for the porous matrix made of small porous elements. For the porous matrix made of spheres,  $\phi_s$  is calculated from the geometry as

$$\phi_s = 1 - \frac{\pi}{6} \left( \frac{d_s}{s_s} \right)^3. \quad (6.2)$$

In order to compare, I calculated the flows in porous matrices with only one length scale in the macroscopic simulation. They are made of only large porous elements (Fig. 6.2). The porous

matrix of small elements is modeled. The governing equations (2.9-2.10) with the PSPH model are used.

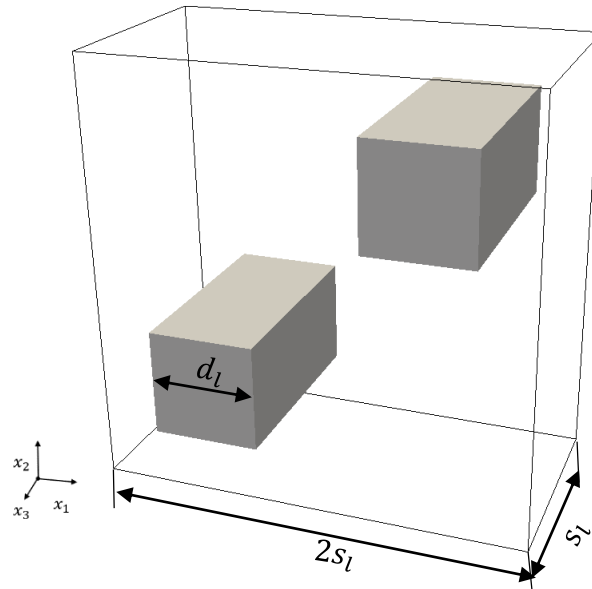


Figure 6.2. A porous matrix with only a large pore scale (made of bars) for the macroscopic study.

The flow in the geometry of Fig. 6.1(a) is simulated by solving the microscopic equations (DNS) with LBM while the flow in the geometry of Fig. 6.2 is simulated by solving the macroscopic equations with FVM, which is for all test cases in this chapter.

### 6.2.2 Instantaneous flow fields

The cases “bars+spheres” with  $\phi_s = 0.70$  are calculated using both DNS and macroscopic simulation methods. Fig. 6.3 shows instantaneous velocity magnitude. For the DNS case, the Reynolds number is high enough to ensure the turbulent flow is fully developed. However, no turbulence shows in macroscopic results with the same Reynolds number. This is reasonable because the turbulence limited in pore size is modeled based on PSPH.

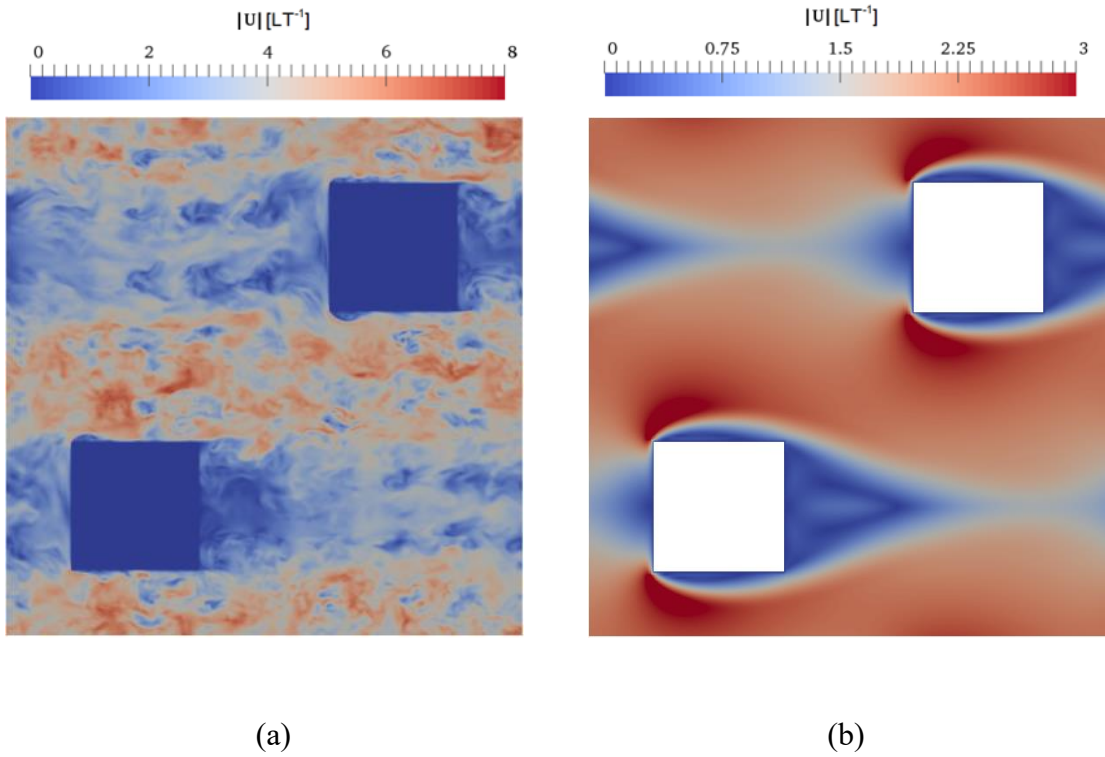


Figure 6.3. Instantaneous velocity magnitude for porous medium with two length scales,  $\phi_s = 0.70$ ,  $Re_s = 620$ . (a) DNS result; (b) macroscopic simulation result.

### 6.2.3 Statistical results

The FVM and LBM methods have been intensively applied and verified in my previous chapters 4-5. Here I make further verification of mesh independence in a porous medium with two length scales. Figure 6.4 shows the relationship between  $Re_l$  and the drag coefficient  $f_D = \frac{d_l g_1}{u_m^2}$  calculated from different mesh resolutions and solvers (the FVM and the LBM). The porous matrix is “bars+spheres” with  $\phi_s = 1.0$ . It can be seen that calculated  $Re_l$  is only marginally changed as the number of mesh cells is increased. The LBM results for the applied pressure gradient are about 6% higher than the FVM results. The reason is that the bounced back model used in the LBM leads to slightly larger solid region. This is an acknowledged error. Therefore, it can be seen that the results are mesh-independent.

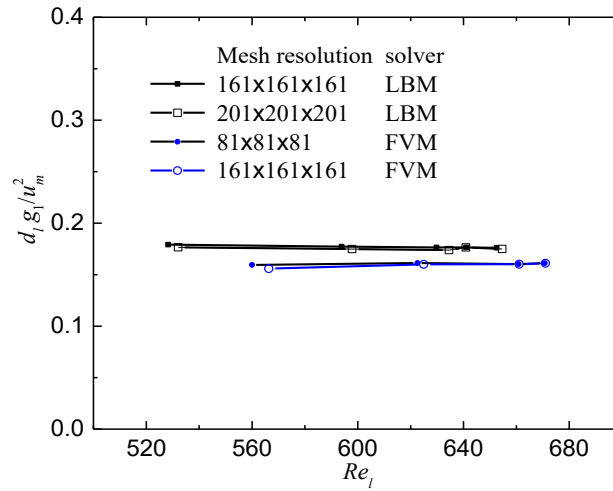


Figure 6.4. Applied pressure gradient  $g_1$  versus Reynolds number  $Re_l$ , DNS and macroscopic results. FVM and LBM results with different mesh resolutions are compared.

In order to further confirm the accuracy of the PSPH model, the flows in a porous medium with two length scales are simulated by solving microscopic equations with LBM and macroscopic equations with FVM. Fig. 6.5 shows the time-, REV-, and spanwise ( $x_3$ -) averaged velocity components  $\langle \bar{u}_1 \rangle^{v,x3}$  and  $\langle \bar{u}_2 \rangle^{v,x3}$  along the streamwise ( $x_1$ -) lines. It can be seen that the macroscopic simulation results are in reasonable accordance with the DNS results; the macroscopic simulation model is well validated.

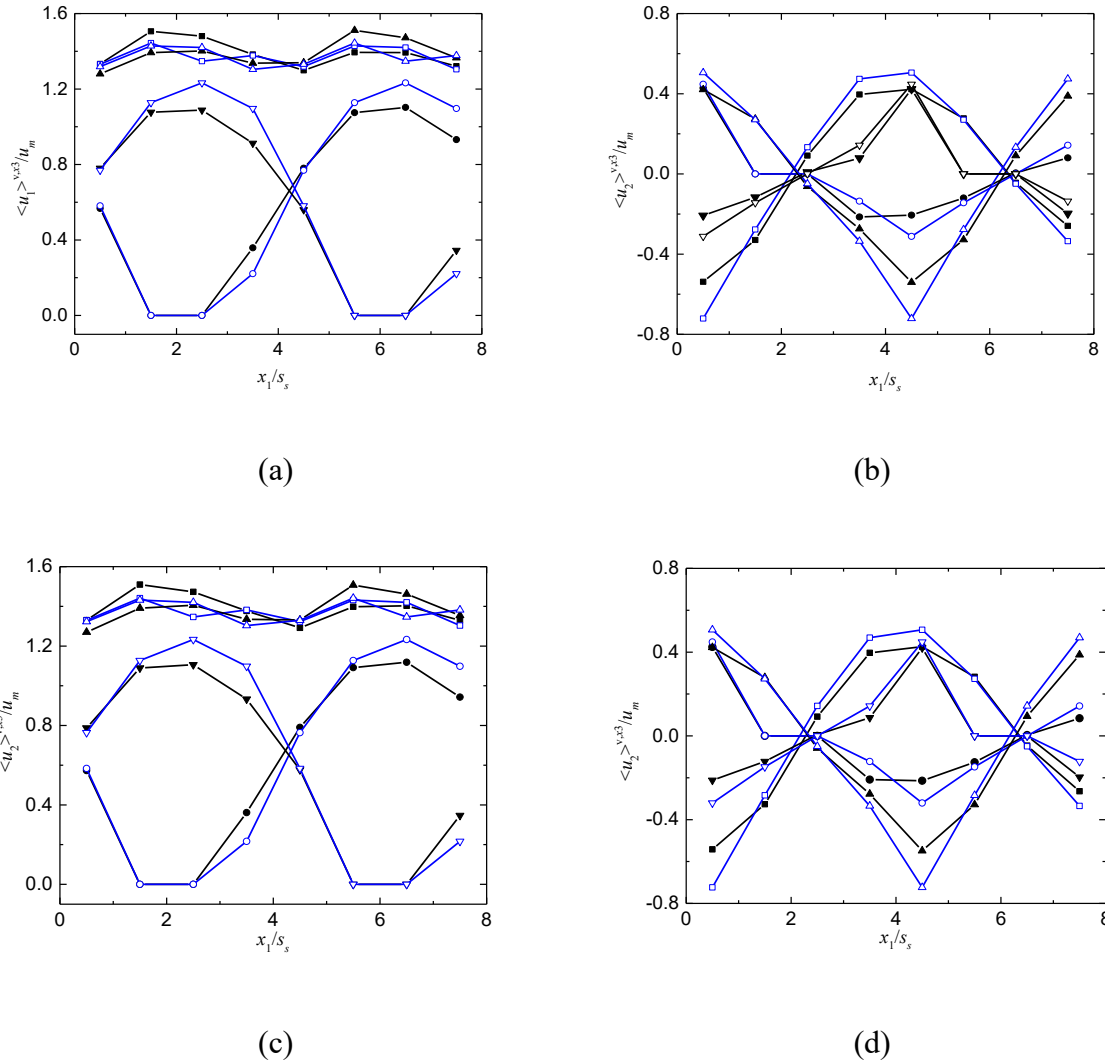


Figure 6.5. Distribution of  $\langle \bar{u}_1 \rangle^{v,x3}$  and  $\langle \bar{u}_2 \rangle^{v,x3}$  along the streamwise ( $x_1$ -) lines at  $x_2/s_s = 0.5$  (squares), 2.5 (circles), 4.5 (up-pointing triangles) and 6.5 (down-pointing triangles). Solid symbols indicate DNS results and hollow symbols indicate macroscopic simulation results. The porous matrix is “bars+spheres” with  $\phi_s = 0.70$ . The Reynolds number  $Re_s$  is 436 (a, b) and 620 (c, d), respectively.

### 6.3 Conclusions

The fluid flows in the porous medium with two length scales are simulated by solving microscopic equations (DNS) with LBM and macroscopic equations with FVM. The averaged velocity are compared between DNS and macroscopic results with two different Reynolds numbers.

The comparisons imply that the results are mesh-independent and the macroscopic simulation results are in reasonable accordance with the DNS results and well-validated.

# Chapter 7

## Limit of the pore scale prevalence hypothesis

### 7.1 Introduction

In the previous chapters, the PSPH model was derived based and validated. The PSPH asserts that turbulent structures in the porous media are limited to pore size. However, macroscopic turbulence must emerge without the restriction of the porous matrix (when the porosity approaches 1). The purpose of this chapter is to find out under what conditions the large turbulent structures might survive. To achieve this goal, the DNS and macroscopic simulation results of section 6 (flows in a porous matrix with two length scales) are further analyzed in this chapter. Strong large-scale turbulence can be stimulated by the large porous matrix made up of square cylinders. However, the large-scale turbulence is suppressed by the small porous matrix made up of spheres or cubes. The spacing between small porous elements is varied to obtain different porosity values. The analyses are performed for various values of the Reynolds number, pore-scale ratio, porosity, and Darcy numbers. Instantaneous  $Q$  iso-surfaces, turbulent two-point correlations, integral length scales, premultiplied energy spectra, and the kinetic energy of macroscopic turbulence are applied to determine the length scale of the turbulent structures from the DNS and the macroscopic simulation results. The capability of the PSPH model is further confirmed with further comparisons between the DNS and macroscopic simulation results.

### 7.2 Geometry of the porous matrix

The porous matrices of chapter 6 (Fig. 6.1 and 6.2) are used in the chapter. In order to make the comparison, I have also calculated the flows in porous matrices with only one length scale. They are made of only small porous elements (Fig. 7.1). The same domain size ( $2s_l \times 2s_l \times s_l$ ) is used for all test cases.

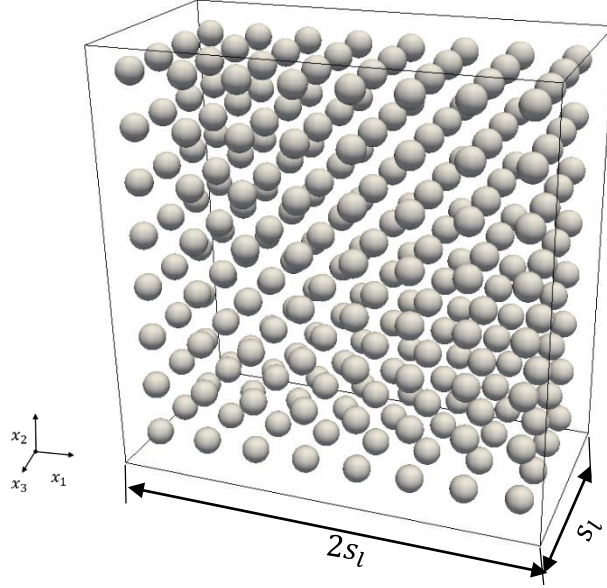


Figure 7.1. a porous matrix with only small pore scale (made of spheres).

The Darcy number  $Da_n$  for a generic porous matrix (GPM) made of small porous elements (aligned spheres or cubes) can be defined as

$$Da_n = K/d_l^2. \quad (7.1)$$

For the porous matrix made of cubes,  $\phi_s$  is calculated as

$$\phi_s = 1 - \left(\frac{d_s}{s_s}\right)^3. \quad (7.2)$$

### 7.3 Macroscopic equations for infinite Reynolds number

To further understand the derived macroscopic equation, inserting Eqs. (2.13) and (2.17) into Eq. (2.10), normalizing with the mean velocity  $u_m$  and the element size  $d_l$ , the following dimensionless macroscopic equations can be obtained:

$$\frac{\partial \tilde{u}_{Di}}{\partial \tilde{x}_i} = 0, \quad (7.3)$$

$$\frac{\partial \tilde{u}_{Di}}{\partial \tilde{t}} + \frac{\partial(\tilde{u}_{Di}\tilde{u}_{Di}/\phi)}{\partial \tilde{x}_j} = -\frac{\partial(\phi\langle \tilde{p} \rangle^i)}{\partial \tilde{x}_i} + \phi \tilde{g}_i - \tilde{R}_i + \tilde{L}_i. \quad (7.4)$$

where  $\tilde{\cdot}$  denotes a dimensionless variable.  $\tilde{R}_i$  is approximated with the first two leading order terms of Eq. (2.13). The dimensionless drag and Laplacian terms are calculated as

$$\check{R}_i = \frac{\phi}{Da_n Re_l} \check{u}_{Di} + \frac{\phi c_{F1}}{Da_n^{1/2}} |\check{\mathbf{u}}_D| \check{u}_{Di}, \quad (7.5)$$

$$\check{L}_i = 2 \frac{\partial}{\partial x_j} \left[ \left( \frac{c_{B1}}{Re_l} + c_{B2} Da_n |\check{\mathbf{s}}_D| \right) \hat{s}_{Dij} \right]. \quad (7.6)$$

When  $Re_l$  is high enough ( $Re_l \rightarrow \infty$ ), Eqs. (7.5) and (7.6) can be simplified as

$$\check{R}_i = \frac{\phi c_{F1}}{Da_n^{1/2}} |\check{\mathbf{u}}_D| \check{u}_{Di}, \quad (7.7)$$

$$\check{L}_i = \frac{\partial}{\partial x_j} (2c_{B2} Da_n |\check{\mathbf{s}}_D| \check{s}_{Dij}). \quad (7.8)$$

Eq. (7.7) is consistent with the momentum equation for canopy flows (Nepf 2012) in which the viscous resistance is neglected. It can be seen that the momentum transport is affected by the geometric parameters  $\phi$ ,  $c_{F1}$ ,  $c_{B2}$  and  $Da_n$  when  $Re_l$  is high enough. If the correlations and model coefficients for calculating  $c_{B2}$  and the Forchheimer term are generic for all porous matrices, Eqs. (7.7)-(7.8) are determined only by  $Da_n$  and  $\phi$ .

## 7.4 Description of the test cases

The main parameters for DNS cases and macroscopic simulation cases are shown in Table 7.1 and 7.2, respectively. The length-scale ratio  $s_s/d_s$  are varied in the DNS cases to obtain the porosity values from 0.61 to 0.98. For  $\phi_s = 0.7$ , the pore-size ratio  $s_l/s_s$  varies between 4 and 12. Relatively large Reynolds numbers are studied ( $Re_s > 350$  and  $Re_l > 500$ ) to ensure the flows are in the turbulent regime; the laminar-turbulent transition is not in the scope of this study. A higher resolution mesh is used for flows with a higher Reynolds number, see table 7.1 for the highest and lowest mesh resolutions for each geometry.

The solid matrix geometry in the first group of test cases is the same as “bars+spheres” in the DNS of the previous chapter. The values of  $s_l/s_s$  are set to 4 and 8 so the macroscopic simulation results can be compared with the DNS results. In another group of cases, I have carried out the macroscopic simulation for  $Re_l \rightarrow \infty$  to exclude the effect of the Reynolds number. The small porous elements are not specified in these cases and the Darcy number is given directly, so this porous matrix is named as “bars+GPM”. Eqs. (7.5) and (7.6) with the drag terms expressed by Eqs. (7.7) and (7.8), corresponding to  $Re_l \rightarrow \infty$ , are solved for the calculation of this group of cases.

Typical DNS and macroscopic simulation cases are calculated using two mesh resolutions to perform the mesh-convergence study. In addition, typical macroscopic simulation results are compared with the DNS results for validation. Details about verification and validation are presented in chapters 6 and appendix A.

Porous matrix	$\phi_s$	$s_l/s_s$	Mesh resolution	$Re_s$	$Re_l$
“bars+spheres”	0.61-0.98	4-12	$353 \times 353 \times 177$	355-704	781-4224
			$1153 \times 1153 \times 577$		
“bars+cubes”	0.88-0.98	4	$641 \times 641 \times 321$	614-749	2512-5992
			$1281 \times 1281 \times 641$		
“spheres”	0.61-0.98	-	$353 \times 353 \times 177$	391-754	860-4524
			$961 \times 961 \times 481$		
“cubes”	0.88-0.96	-	$641 \times 641 \times 321$	469-689	2352-4137
			$961 \times 961 \times 481$		
“bars”	1.0	-	$161 \times 161 \times 81$	-	528-653
			$201 \times 201 \times 201$		

Table 7.1. Main parameters for the DNS cases, LBM. The lowest and highest mesh resolutions for each porous matrix are shown.

Porous matrix	$\phi_s$	$s_l/s_s$	$Da_n$	Mesh resolution	$Re_K$	$Re_l$
“bars+spheres”	0.93-0.99	4, 8	0.07-1.26	$161 \times 161 \times 81$	39-2009	62-5392
“bars+GPM”	0.93-0.99	-	0.3-1.2	$161 \times 161 \times 81$ $256 \times 256 \times 256$	$\infty$	$\infty$
“bars”	1.0	-	-	$81 \times 81 \times 81$ $161 \times 161 \times 161$	-	566-671

Table 7.2. Main parameters for the cases of macroscopic simulation, FVM. The lowest and highest mesh resolutions for each porous matrix are shown.

## 7.5 Instantaneous flow field

The  $Q$ -method (Hunt *et al.*, 1988), where the quantity  $Q = -\frac{1}{2} \frac{\partial u_i}{\partial x_j} \frac{\partial u_j}{\partial x_i}$ , is the second invariant of the instantaneous velocity gradient tensor is used to identify the turbulent structures in porous media qualitatively. According to the  $Q$ -method, vortices can be identified by connected fluid regions with positive  $Q$  values. Figure 7.2 shows the turbulent structures identified by the iso-surfaces of  $Q$  in different porous matrices for DNS results. When the porous matrix has only large elements (staggered arrays of square cylinders), it can be seen in Fig. 7.2a that the size of vortices is close to the large pore size  $s_l$ .

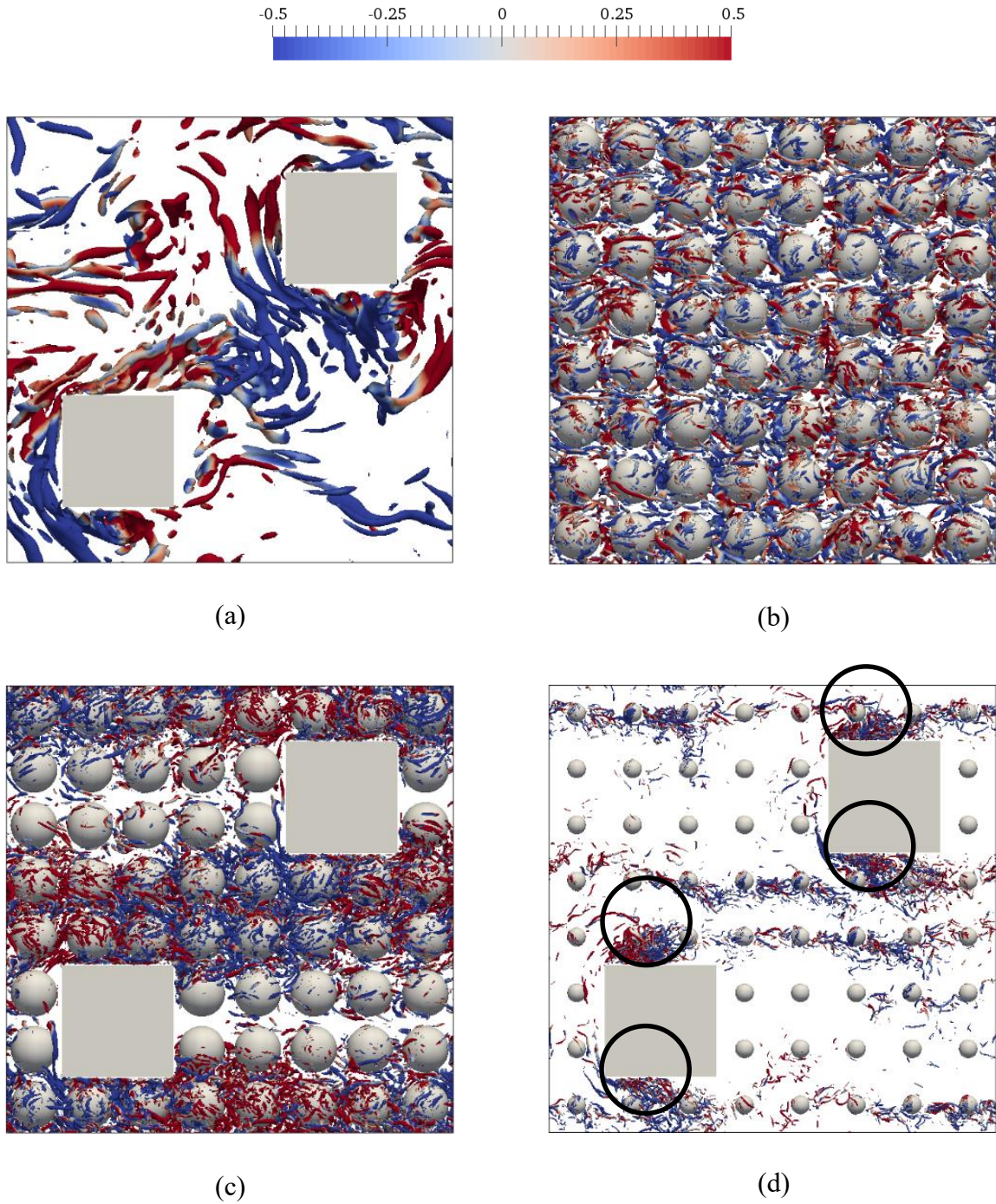


Figure 7.2. Instantaneous turbulence structures for DNS results, color coding showing the instantaneous value of the vertical velocity  $u_2$ ,  $Q/Q_M = 2 \times 10^{-2}$ . Possible large-scale structures are indicated by circles. (a) Bars,  $\phi_s = 1.0$ ,  $Re_l = 641$ ,  $Q_M d_l^2 / u_m^2 = 4.8 \times 10^3$ ; (b) Spheres,  $\phi_s = 0.70$ ,  $Re_s = 545$ ,  $Re_l = 1308$ ,  $Q_M d_l^2 / u_m^2 = 2.04 \times 10^4$ ; (c) Bars and spheres,

$\phi_s = 0.70$ ,  $Re_s = 536$ ,  $Re_l = 1286$ ,  $Q_M d_l^2 / u_m^2 = 1.35 \times 10^4$ ; (d) Bars and spheres,  $\phi_s = 0.98$ ,  $Re_s = 564$ ,  $Re_l = 3384$ ,  $Q_M d_l^2 / u_m^2 = 2.01 \times 10^5$ .

For the porous matrix with only small porous elements, fully developed turbulence can be found when  $Re_s$  is about 500. The size of vortices is close to the small pore size  $s_s$ , which is much smaller than  $s_l$ , see Fig. 7.2b.

If I combine the two porous elements together, I may investigate whether (or in what condition) the vortices with the large length scale  $s_l$  may survive. The values of  $Re_s$  for the cases in Fig. 7.2c and 7.2d are still above 500. The size of turbulent structures is generally close to the small pore size  $s_s$  for a medium porosity value ( $\phi_s = 0.7$ ), see Fig. 7.2c. The vortical tubes are more densely populated in the passage between the two large porous elements. However, any vortices which are larger than  $s_s$  have been not observed. All large vortices are damped by the porous medium made of small porous elements and vanish. This is in accordance with the PSPH. However, when the porosity is increased to  $\phi_s = 0.98$ , some vortical bulks which are larger than  $s_s$  (close to the large element size  $d_l$ ) can be found; their locations are indicated by the circles in Fig. 7.2d. The long wakes downstream the large vortical bulks can also be seen. The vortical structures show qualitatively that large scale turbulence survives when  $\phi_s = 0.98$ .

To compare with the DNS results, the instantaneous velocity magnitude of macroscopic simulation results in a cross-section for different values of porosity  $\phi_s$  is shown in Fig. 7.3. The Reynolds number  $Re_l$  is 5060 for  $\phi_s = 0.93$ , which is much higher than the critical value of  $Re_l$  for the onset of macroscopic turbulence when the porous matrix has only large porous elements. The value of  $Re_K$  is 1302, suggesting that the flow is in the Forchheimer regime. However, no macroscopic turbulence is found in this case, see Fig. 7.3 (a), while the microscopic turbulence is modeled. The macroscopic turbulence survives as the porosity  $\phi_s$  is increased to 0.98 (Fig. 7.3 (b)). Similarly, macroscopic turbulence is also found as  $\phi_s$  is further increased, see Fig. 7.3 (c) for  $\phi_s = 0.99$  and Fig. 7.3 (d) for  $\phi_s = 1$ . The macroscopic simulation results are consistent with the DNS results.

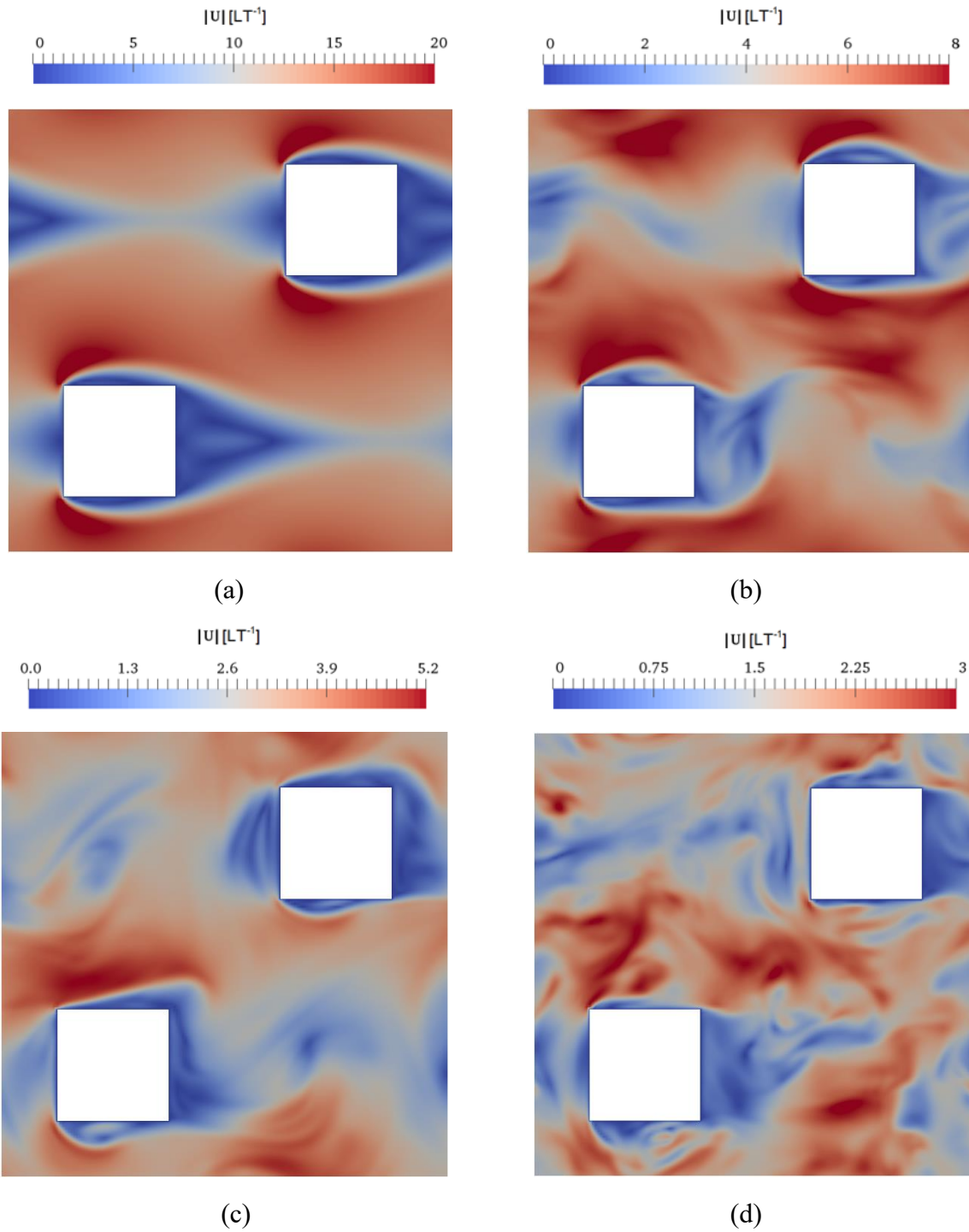


Figure 7.3. Instantaneous velocity magnitude for macroscopic simulation results, “bars+spheres”. (a)  $\phi_s = 0.93$ ,  $Da_n = 0.07$ ,  $Re_K = 1302$ ,  $Re_l = 5060$ ; (b)  $\phi_s = 0.98$ ,  $Da_n = 0.39$ ,  $Re_K = 1225$ ,  $Re_l = 1969$ ; (c)  $\phi_s = 0.99$ ,  $Da_n = 1.26$ ,  $Re_K = 1135$ ,  $Re_l = 1009$ ; (d)  $\phi_s = 1.0$ ,  $Re_l = 630$ .

## 7.6 Two-point turbulent correlations

The  $Q$ -method should be combined with other statistical results to reach quantitative conclusions. In order to detect the length scale of turbulence quantitatively, the two-point correlation due to turbulence  $\hat{R}_{ij}(\mathbf{r}, \mathbf{x}_0)$  is calculated. The following introduces how to get the true turbulent correlation  $\tilde{R}_{ij}(\mathbf{r}, \mathbf{x}_0)$ .

Based on Jin *et al.* (2015) and Uth *et al.* (2016), the turbulent velocity components  $u'_i(\mathbf{x}_0, t)$  and  $u'_j(\mathbf{x}_0 + \mathbf{r}, t)$  are correlated, as shown in Fig. 7.4.

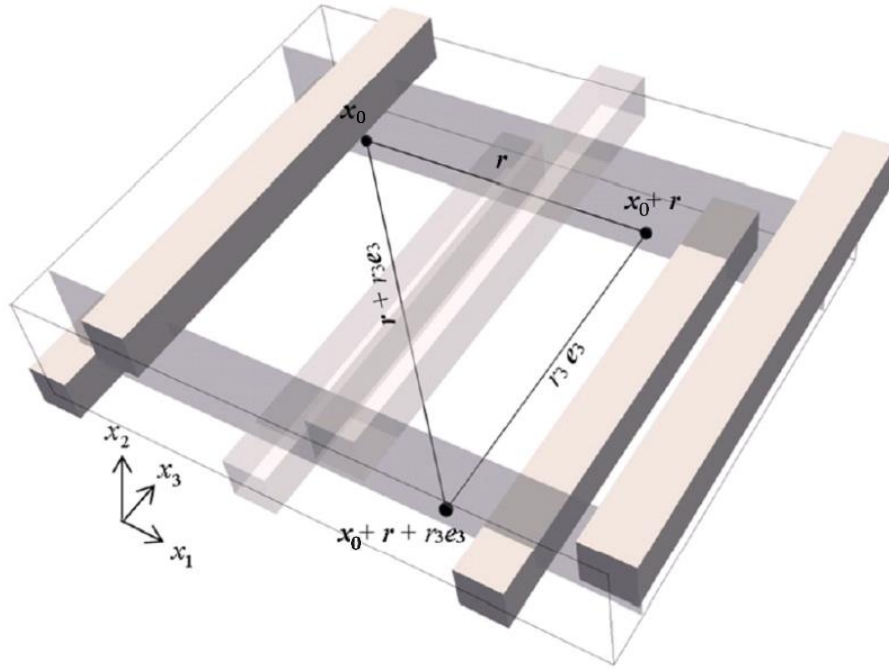


Figure 7.4. Correlation points in two parallel planes (Uth *et al.*, 2016).

The overall two-point correlation  $R_{ij}(\mathbf{r}, \mathbf{x}_0)$  can be directly calculated, it is defined as

$$R_{ij}(\mathbf{r}, \mathbf{x}_0) = \langle u'_i(\mathbf{x}_0, t)u'_j(\mathbf{x}_0 + \mathbf{r}, t) \rangle_t \quad (7.9)$$

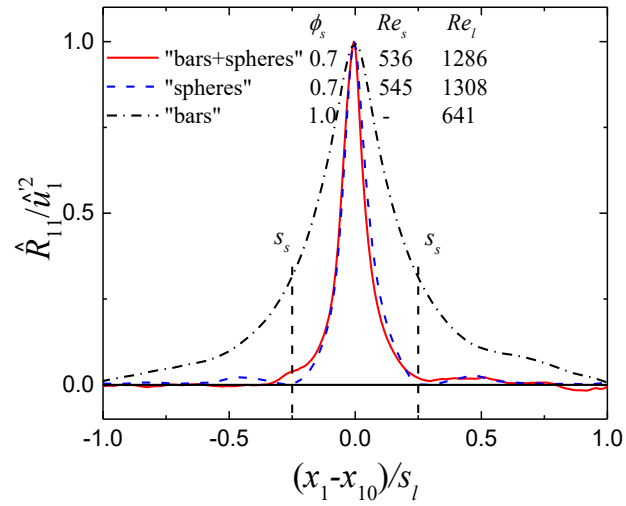
where the operator  $\langle \cdot \rangle_t$  denotes the time-averaging. However, the overall two-point correlation  $R_{ij}(\mathbf{r}, \mathbf{x}_0)$  consists of the true turbulent correlation  $\hat{R}_{ij}(\mathbf{r}, \mathbf{x}_0)$  and non-turbulent correlation  $\tilde{R}_{ij}(\mathbf{r}, \mathbf{x}_0)$ . The true turbulent correlation  $\hat{R}_{ij}(\mathbf{r}, \mathbf{x}_0)$  is adopted to analyze a turbulent flow regarding the scales (Jin *et al.*, 2015; Uth *et al.*, 2016). To derive  $\hat{R}_{ij}(\mathbf{r}, \mathbf{x}_0)$ , a lateral correlation is calculated as

$$\tilde{R}_{ij}(\mathbf{r}, r_3, \mathbf{x}_0) = \langle u'_i(\mathbf{x}_0, t) u'_j(\mathbf{x}_0 + \mathbf{r} + r_3 \mathbf{e}_3, t) \rangle_t \quad (7.10)$$

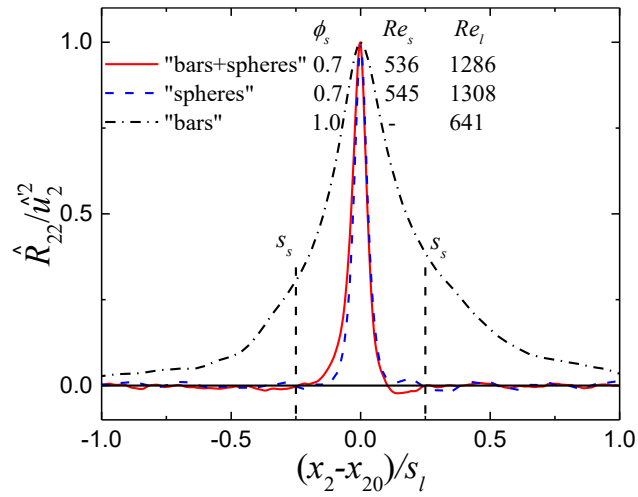
where  $\mathbf{e}_3$  is the unit vector in the spanwise direction and  $r_3$  is the value of distance. Due to the periodicity of the flow in the  $x_3$ , the non-turbulent correlation  $\tilde{R}_{ij}(\mathbf{r}, \mathbf{x}_0)$  can be approximated by  $\tilde{R}_{ij}(\mathbf{r}, r_3, \mathbf{x}_0)$  if  $r_3$  is large enough. Thus, the turbulent two-point correlation can be calculated as

$$\hat{R}_{ij}(\mathbf{r}, \mathbf{x}_0) = R_{ij}(\mathbf{r}, \mathbf{x}_0) - \tilde{R}_{ij}(\mathbf{r}, r_3, \mathbf{x}_0) \quad (7.11)$$

In this thesis, the correlation point  $\mathbf{x}_0$  is at the center of the cross-plane  $(s_l, s_l, x_3)$ . The distributions of  $\hat{R}_{11}(\mathbf{r}, \mathbf{x}_0)$  for turbulent flows in porous matrices with two length scales (“bars+spheres”) or only one length scale (“bars” or “spheres”) are shown in Fig. 7.5. It can be seen that, if the porous matrix has only large porous elements (“bars”),  $\hat{R}_{11}$  is non-zero as the distance from the center point  $x_1 - x_{10}$  is in the range  $[-s_l, s_l]$ , while  $\hat{R}_{22}$  is non-zero as  $x_2 - x_{20}$  is in the range  $[-s_l, s_l]$ , indicating that the turbulence close to the domain center has the length scale  $s_l$ , see the dash-dotted lines in Fig. 7.5. If the porous matrix has also small porous elements (“spheres”) with medium porosity ( $\phi_s = 0.7$ ), no matter whether the large porous elements (“bars”) are present or not, the non-zero ranges of  $\hat{R}_{11}$  and  $\hat{R}_{22}$  are reduced to  $[-\frac{1}{4}s_l, \frac{1}{4}s_l]$ , see the solid and dashed lines in Fig. 7.5. Turbulence has the length scale  $\frac{1}{4}s_l$  which is identical to the small pore size  $s_s = \frac{1}{4}s_l$ . The DNS results confirm the PSPH, which states that, for a porous matrix with medium with low porosity, the turbulence length scale is generally determined by the pore size and there is no macroscopic turbulence.



(a)

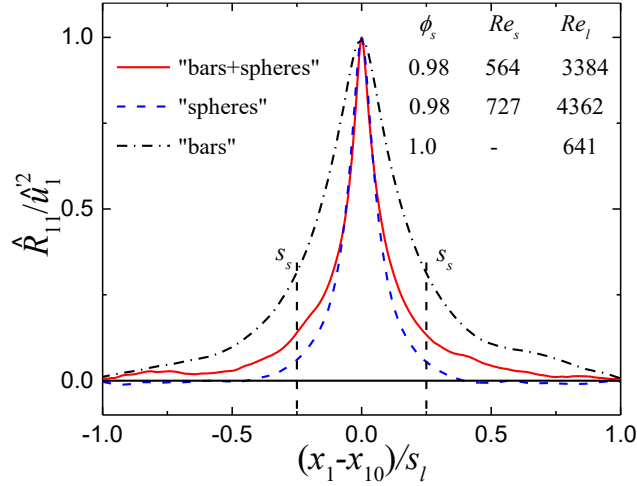


(b)

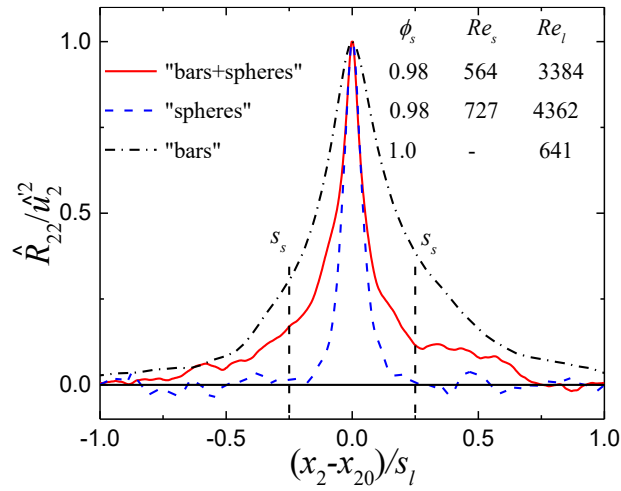
Figure 7.5. Turbulent two-point correlations in the streamwise  $x_1$  direction (a) and transverse  $x_2$  direction (b) for DNS results.

As the value of  $\phi_s$  is increased to 0.98, while the Reynolds number is kept high enough to ensure the flow to be fully turbulent, the non-zero ranges of  $\hat{R}_{11}$  and  $\hat{R}_{22}$  for “bars+spheres” become wider than  $[-\frac{1}{4}s_l, \frac{1}{4}s_l]$ , see Fig. 7.6. They are also larger than the non-zero ranges for

“spheres”. The DNS results indicate that macroscopic turbulence might survive at large porosity values.



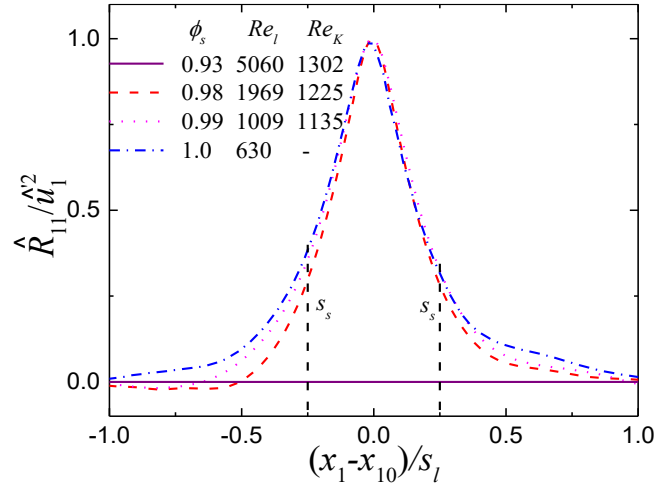
(a)



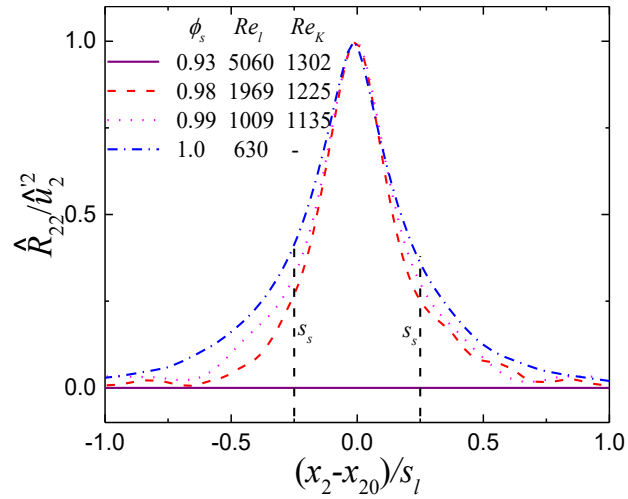
(b)

Figure 7.6. Turbulent two-point correlations in the streamwise  $x_1$  direction (a) and transverse  $x_2$  direction (b) for DNS results. Solid lines: “bars+spheres”,  $\phi_s = 0.98$ ,  $Re_s = 564$ ,  $Re_l = 3384$ ; Dashed lines: “spheres”,  $\phi_s = 0.98$ ,  $Re_s = 727$ ,  $Re_l = 4362$ ; Dash dotted lines: “bars”,  $\phi_s = 1.0$ ,  $Re_l=641$ .

In comparison with DNS results, figure 7.7 shows the turbulent two-point correlation  $\hat{R}_{11}(\mathbf{r}, \mathbf{x}_0)$  calculated from the macroscopic simulation. The test cases have similar values of  $Re_K$ .  $\hat{R}_{11}(\mathbf{r}, \mathbf{x}_0)$  is equal to 0 when  $\phi_s = 0.93$  but has a non-zero range when  $\phi_s \geq 0.98$ . This non-zero range of  $\hat{R}_{11}(\mathbf{r}, \mathbf{x}_0)$  exceeds  $[-\frac{1}{4}s_l, \frac{1}{4}s_l]$ , which corresponds to the microscopic length scale, and becomes wider as  $\phi_s$  is increased from 0.98 to 1.



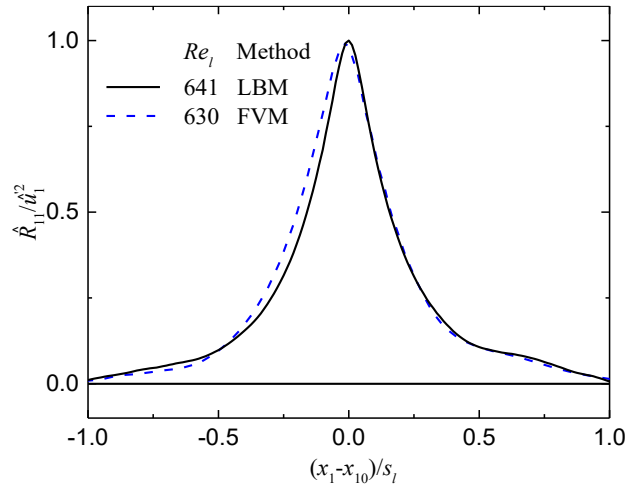
(a)



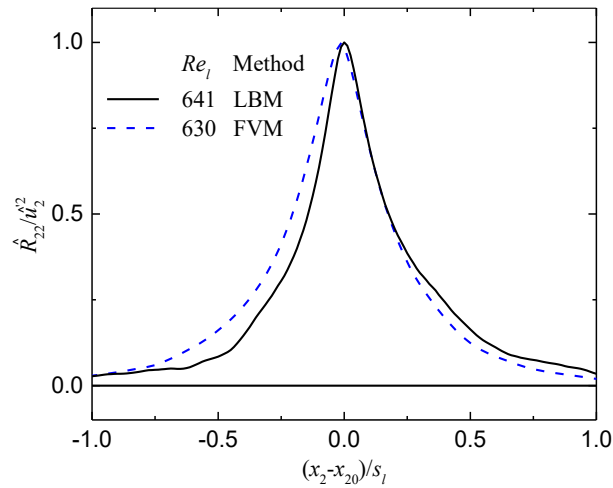
(b)

Figure 7.7. Turbulent two-point correlations in the streamwise  $x_1$  direction (a) and transverse  $x_2$  direction (b) for macroscopic simulation results. The porosity  $\phi_s$ , Reynolds number  $Re_l$  and  $Re_K$  are varied.

In order to better show the comparisons, Fig. 7.8 shows the turbulent two-point correlation values of DNS and macroscopic results in the same figures.



(a)



(b)

Figure 7.8. Turbulent two-point correlations in the streamwise ( $x_1$ -) direction (a) and transverse ( $x_2$ -) direction (b). The porous matrix is made of staggered arrays of bars,  $\phi_s = 1$ . FVM and LBM results are compared.

## 7.7 Integral length scales

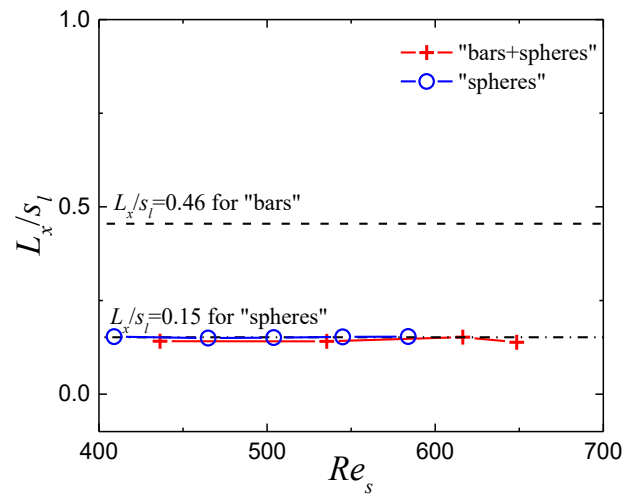
In addition to the turbulent two-point correlations, the integral length scales are another way to quantify the length scale of turbulence. Similar to the definitions in Pope (2000), the longitudinal integral length scales in the parallel ( $x_1$ -) and transverse ( $x_2$ -) directions  $L_x$  and  $L_y$  are respectively calculated as

$$L_x = \int_{-\infty}^{\infty} \hat{R}_{11}(r_1 \mathbf{e}_1, \mathbf{x}_0) / \hat{u}_1'^2(\mathbf{x}_0) dr_1, \quad (7.12)$$

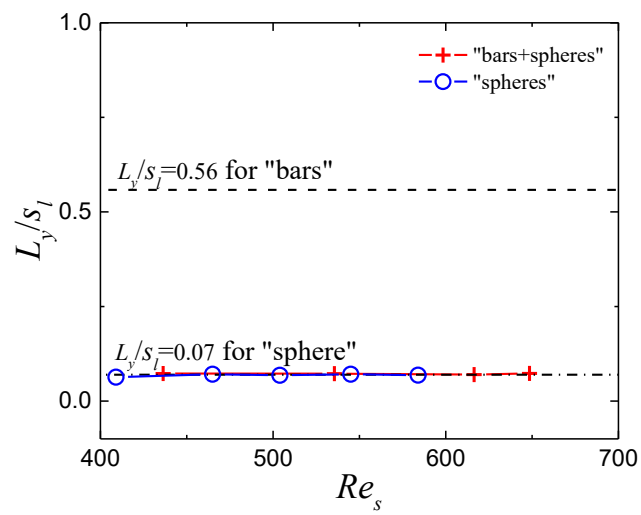
$$L_y = \int_{-\infty}^{\infty} \hat{R}_{22}(r_2 \mathbf{e}_2, \mathbf{x}_0) / \hat{u}_2'^2(\mathbf{x}_0) dr_2, \quad (7.13)$$

where  $\hat{u}_i'^2(\mathbf{x}_0)$  is the root-mean-square turbulent velocity component of the original position  $\mathbf{x}_0$ . Here, I assume that the definition of  $L_x$  and  $L_y$  can still be applied although the flow in the porous medium is neither isotropic nor homogeneous.

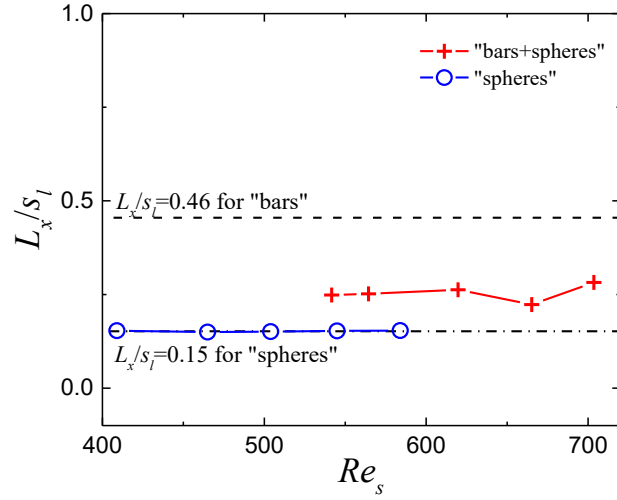
$L_x$  and  $L_y$  for “bars+spheres” with different Reynolds numbers  $Re_s$  are shown in Fig. 7.9. They are compared with the integral length scales in the porous matrices with only large length scale (“bars”) or small length scale (“spheres”).  $L_x$  and  $L_y$  are averaged in a certain range of Reynolds numbers ( $Re_s \in [400, 600]$  for “spheres” and  $Re_l \in [528, 653]$  for “bars”) for further analysis. The averaged integral length scales  $\langle L_x \rangle / s_l$  and  $\langle L_y \rangle / s_l$  for “spheres” are 0.15 and 0.07, respectively. They are much lower than the averaged integral length scales for “bars”, which are 0.46 and 0.56, respectively. It can be seen in Fig. 7.9a and 7.9b that the  $L_x / s_l$  and  $L_y / s_l$  values for “bars+spheres” change only marginally with the Reynolds number  $Re_s$  or  $Re_l$ . They are close to the values for “spheres”; this suggests that the macroscopic turbulence cannot be stimulated by increasing the Reynolds number. By contrast,  $L_x / s_l$  and  $L_y / s_l$  become closer to the values for “bars” as the porosity  $\phi_s$  is increased to 0.98, suggesting that the macroscopic turbulence occurs in this condition, see Fig. 7.9c and 7.9d.



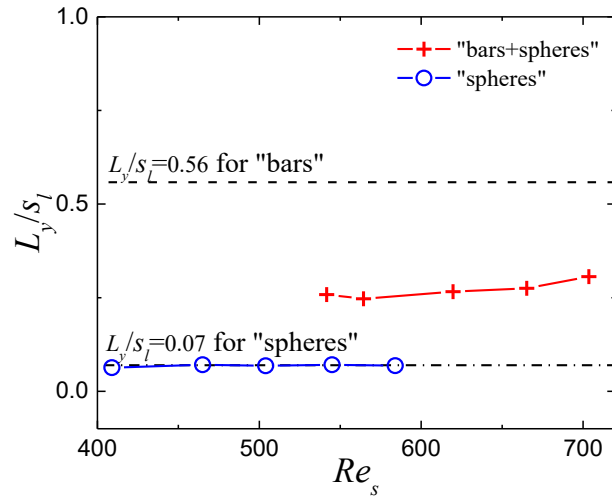
(a)



(b)



(c)

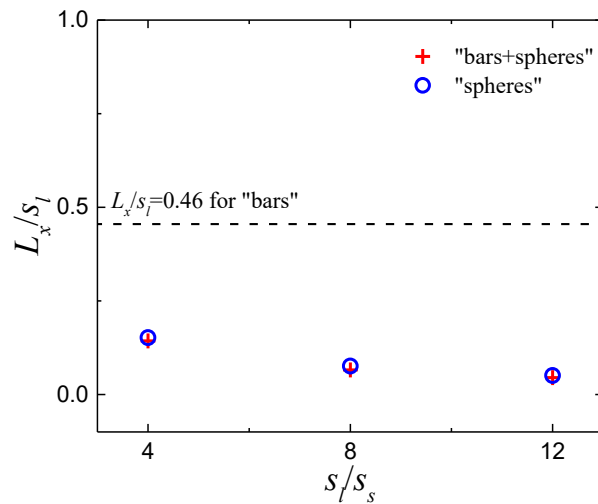


(d)

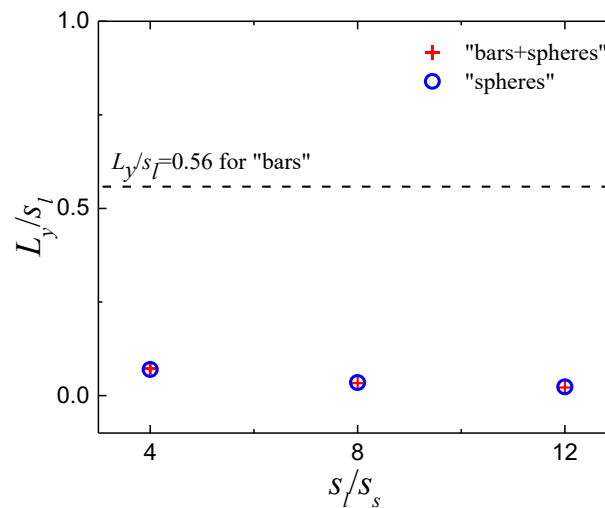
Figure 7.9. Effects of the Reynolds number on the integral length scales for DNS results. (a)  $L_x/s_l$ ,  $\phi_s = 0.70$ ; (b)  $L_y/s_l$ ,  $\phi_s = 0.70$ ; (c)  $L_x/s_l$ ,  $\phi_s = 0.98$ ; (d)  $L_y/s_l$ ,  $\phi_s = 0.98$ .

Figure 7.10 shows the averaged integral length scales  $\langle L_x \rangle/s_l$  and  $\langle L_y \rangle/s_l$  for  $\phi_s = 0.7$  and the pore-scale ratio  $s_l/s_s$  in the range 4-12. The difference between the length scale of macroscopic turbulence and the pore-scale turbulence becomes more evident as the scale ratio  $s_l/s_s$  becomes

larger. As  $s_l/s_s$  is increased from 4 to 12,  $\langle L_x \rangle/s_l$  is decreased from 0.14 to 0.05, while  $\langle L_y \rangle/s_l$  is decreased from 0.07 to 0.02. They are almost identical to the integral length values when the porous matrix has only small porous elements (spheres). The DNS results confirm that there is no macroscopic turbulence for this porosity value.



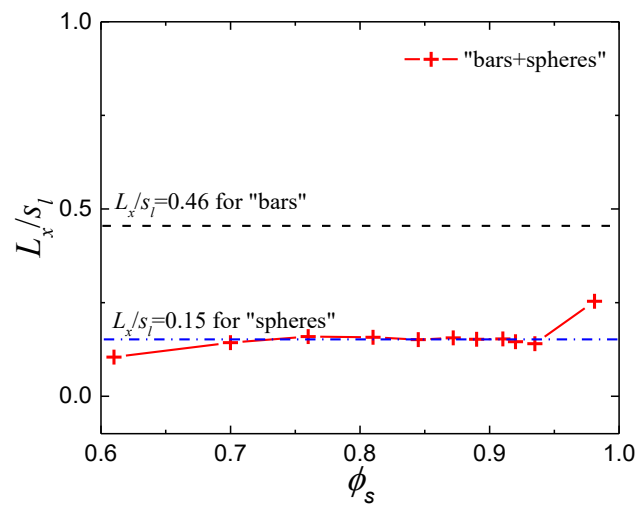
(a)



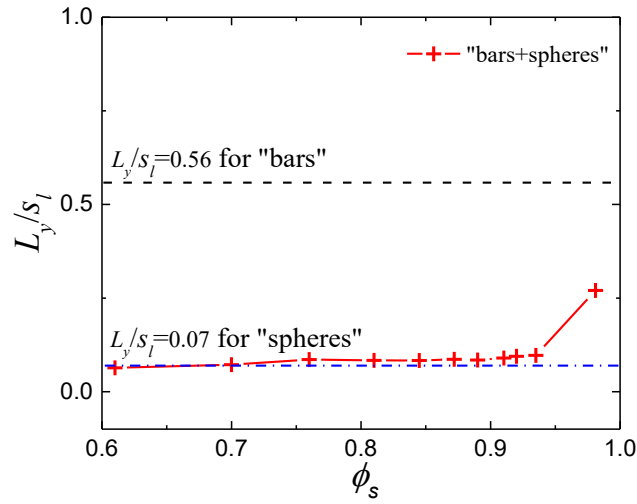
(b)

Figure 7.10. Effects of  $s_l/s_s$  on the averaged integral length scales,  $\phi_s = 0.70$  for DNS results. The length scales are averaged in the range  $Re_s \in [436, 649]$ . (a)  $\langle L_x \rangle/s_l$ ; (b)  $\langle L_y \rangle/s_l$ .

Figure 7.11 shows the relationship between the integral length scales and the porosity  $\phi_s$  when the flow is fully turbulent. The DNS results for “bars+spheres” are compared with those for “bars” and “spheres”.  $\langle L_x \rangle / s_l$  and  $\langle L_y \rangle / s_l$  change only marginally as  $\phi_s$  is increased from 0.61 to 0.93, while an abrupt jump can be found for  $\phi_s = 0.98$ , which indicates the onset of macroscopic turbulence. So, I expect that the critical porosity  $\phi_c$  for the survival of macroscopic turbulence lies between 0.93 and 0.98. It should be noted that, up to now, this critical porosity value is only validated for the scale ratio  $s_l / s_s = 4$ .



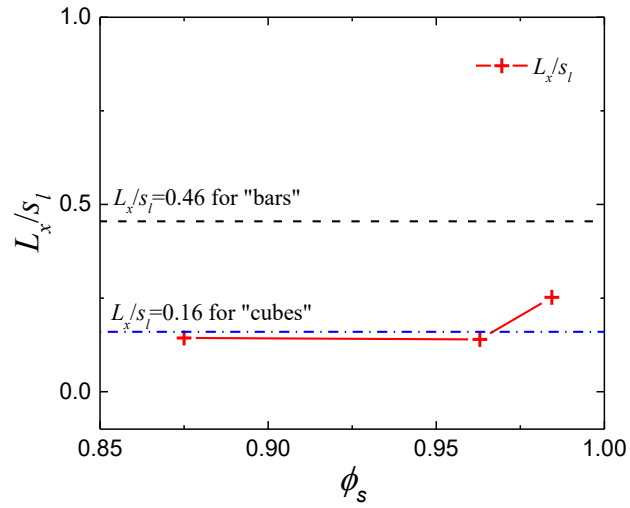
(a)



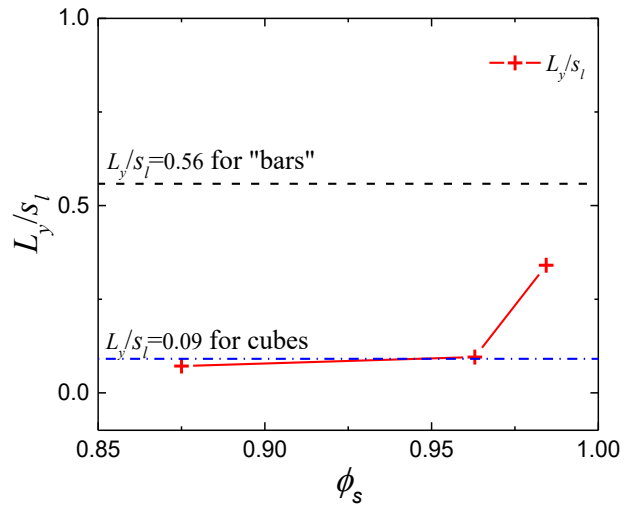
(b)

Figure 7.11. Effects of the porosity  $\phi_s$  on the averaged integral length scales for DNS results. (a)  $\langle L_x \rangle / s_l$ ; (b)  $\langle L_y \rangle / s_l$ .

Another porous matrix has been studied to understand the effects of pore-scale geometry on the critical porosity  $\phi_c$ . The small porous elements for this porous matrix are made of cubes. Fig. 7.12 shows the averaged integral length scales for different porous matrices. It can be seen that the values of  $\langle L_x \rangle / s_l$  and  $\langle L_y \rangle / s_l$  for “bars+cubes” are close to the values for “cubes” as  $\phi_s$  is increased from 0.86 to 0.96. They jump abruptly and become close to the values for “bars” as  $\phi_s$  is increased to 0.98. The DNS results suggest that the critical value for the onset of macroscopic turbulence lies between 0.96 and 0.98. Again, this critical porosity is only validated for the scale ratio  $s_l/s_s = 4$ .



(a)

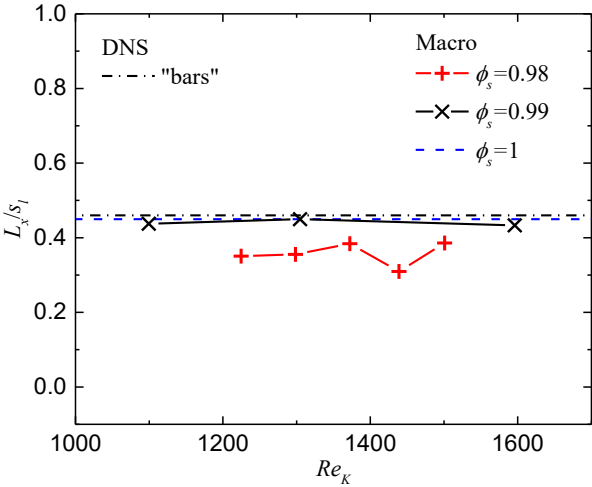


(b)

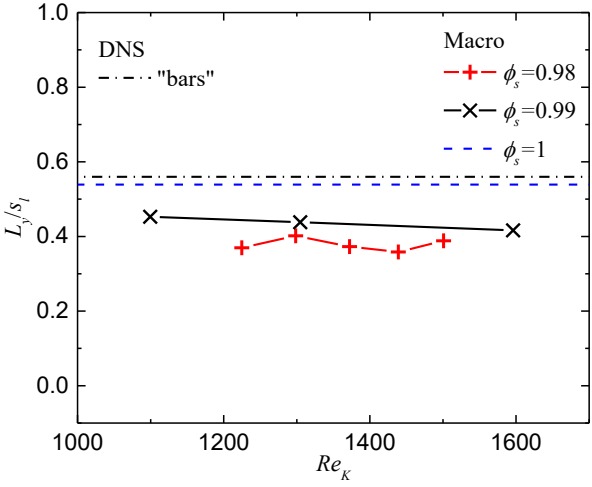
Figure 7.12. The averaged integral length scales for “bars+cubes” for DNS results. (a)  $\langle L_x \rangle / s_l$ ; (b)  $\langle L_y \rangle / s_l$ .

The longitudinal integral length scales  $L_x$  and  $L_y$  for  $Re_K > 1000$  are shown in Fig. 7.13. The macroscopic results are compared with the DNS results for “bars”. Both macroscopic simulation and DNS results show that  $L_x$  and  $L_y$  change only marginally when the value of  $Re_K$

is increased. The values of  $L_x$  and  $L_y$  increase with the increase of  $\phi_s$  and approach the values for  $\phi_s = 1$ . The macroscopic simulation results of  $\langle L_x \rangle$  and  $\langle L_y \rangle$  for  $\phi_s = 1$  are 0.45 and 0.54, respectively, which are close to DNS results for “bars”.



(a)



(b)

Figure 7.13. Turbulent two-point correlations in the streamwise ( $x_1$ -) direction and transverse ( $x_2$ -) direction, “bars+spheres” for macroscopic simulation results. (a)  $L_x$ ; (b)  $L_y$ .

## 7.8 Energy spectra and their premultiplied form

The one-dimensional energy spectra calculated from two-point correlations is applied to calculate the length scale of turbulence. According to the definition by Kolmogorov (1941) for locally homogeneous and isotropic turbulence, it is calculated with the Fourier transform as:

$$\hat{E}_{ii}(\mathbf{x}_0, k_1) = \frac{1}{\pi} \int_{-\infty}^{\infty} \hat{R}_{ii}(x_1 \mathbf{e}_1, \mathbf{x}_0) \exp(-ik_1 x_1) dx_1 \quad (7.14)$$

where  $k_1$  denotes the wavenumber in the  $x_1$  direction. Jin *et al.* (2015) and Gomes-Fernandes *et al.* (2015) argued that this equation can be also used to calculate the local energy spectra for inhomogeneous and anisotropic flows.

Figure 7.14 shows the premultiplied energy spectra  $k_1 \hat{E}_{ii}(\mathbf{x}_0, k_1)$  for DNS results, which can be used to identify the  $k_1^{-1}$  range which represents the very-large-scale motions (Jimenez, 1998). The maximum of wavelength  $\Lambda = 2\pi/k_1$  which corresponds to the peak values of  $k_1 \hat{E}_{ii}(\mathbf{x}_0, k_1)$  represents the largest length scale of turbulent structures (Hommema & Adrian, 2006; Balakumar & Adrian, 2007). When the porous matrix has only large porous elements (bars), the maximum value of  $\Lambda$  is about  $5.3s_s$ , which is between  $s_l = 4s_s$  and  $2s_l = 8s_s$ , while it is much larger than the small pore scale  $s_s$ . When the porosity for the small porous elements has a medium value ( $\phi_s = 0.7$ ), no matter the porous matrix has one (“spheres”) or two (“bars+spheres”) length scales, the maximum value of  $\Lambda$  is about  $1.6s_s$ , which is close to the small pore scale  $s_s$ . By contrast, when the porous matrix has two length scales (“bars+spheres”) and the porosity is large ( $\phi_s = 0.98$ ), the second peak of  $k_1 \hat{E}_{ii}(\mathbf{x}_0, k_1)$  can be observed. The corresponding value of  $\Lambda$  is about  $4s_s$ , which is close to the maximum  $\Lambda$  for “bars”. The premultiplied energy spectra also confirm the occurrence of macroscopic turbulence at  $\phi_s = 0.98$ .

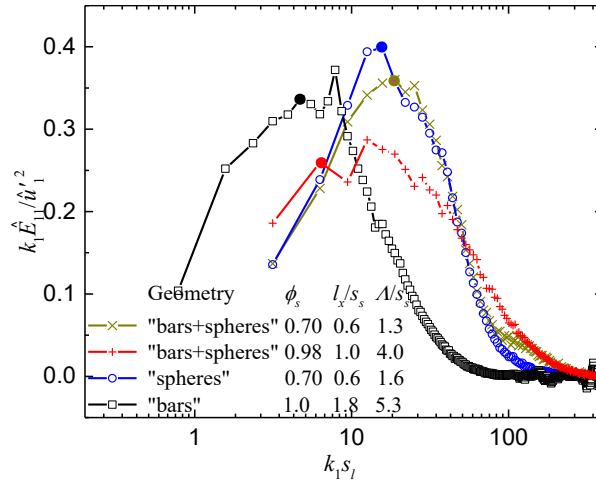


Figure 7.14. Pre-multiplied energy spectra for “bars+spheres”, “bars” and “spheres” for DNS results,  $s_l/s_s = 4$ . The peaks with the lowest wave numbers are indicated with solid circles. The values of  $Re_s$  are 536 for “bars+spheres” with  $\phi_s = 0.7$ , 564 for “bars+spheres” with  $\phi_s = 0.98$  and 545 for “spheres”, respectively. The value of  $Re_l$  for “bars” is 641.

Fig. 7.15 shows the pre-multiplied energy spectra of macroscopic simulation results. A plateau of  $k_1 \hat{E}_{11} / u_1'^2 \approx 0.35$  can be found for porosity  $\phi_s = 1$ , which indicates the range of large-scale turbulent motion. The peak of  $k_1 \hat{E}_{11}$  for  $\phi_s = 1$  corresponds to the wavelength  $\Lambda = 1.33s_l$ , which is identical to the value of  $\Lambda$  for  $\phi_s = 0.99$ . When the porosity  $\phi_s$  is decreased to 0.98, the value of  $\Lambda$  declines to  $s_l$  which is identical to the large pore size.

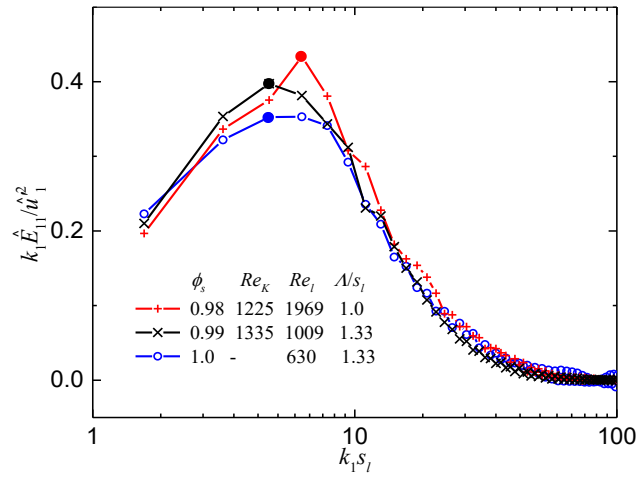


Figure 7.15. Pre-multiplied energy spectra for “bars+spheres” for macroscopic simulation results. The peaks are indicated with solid circles.

Fig. 7.16 shows the pre-multiplied energy spectra of DNS and macroscopic results in one figure to better show the comparisons. The reason of the slight difference is that the bounced back model used in the LBM leads to slightly larger solid region than in the FVM, which is an acknowledged error.

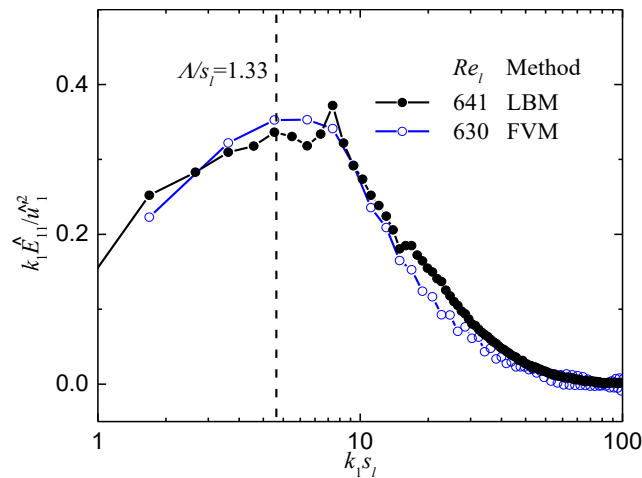


Figure 7.16. Pre-multiplied energy spectra. The porous matrix is made of staggered arrays of bars,  $\phi_s = 1$ . FVM and LBM results are compared.

## 7.9 Turbulent kinetic energy

The DNS and macroscopic simulation results show that, when the Reynolds number is high enough to ensure that the flow is fully turbulent, the porosity has a critical value  $\phi_c$  for the occurrence of macroscopic turbulence.  $\phi_c$  is generally independent of the Reynolds number and to the shape of porous elements. However, it might be affected by the Darcy number which is determined by the scale ratio  $s_l/s_s$ . To further investigate the generality of  $\phi_c$ , I calculated the turbulent flows in the same porous medium only with the large-scale porous matrix using macroscopic simulation for different  $Da_n$  values.

The macroscopic simulation results discussed above are for a GPM made of spherical porous elements with the scale ratio  $s_l/s_s = 4$  or  $8$ . The permeability  $K$  is calculated using the Carman-Kozeny equation (2.23). However, the values of  $K$  and the Darcy numbers calculated from this equation might have uncertainties due to the variation of the pore-scale geometries. To better understand the dependence of the critical porosity  $\phi_c$  on the Darcy number, I have solved Eqs. (7.3) and (7.4) with the drag terms expressed by Eqs. (7.7) and (7.8) for different Darcy numbers. These solutions correspond to the limit of infinite Reynolds number,  $Re_l \rightarrow \infty$ . Figure 7.17 shows the relationship between  $\phi_s$  and  $2\langle k \rangle / u_m^2$ . The macroscopic simulation results indicate that the critical porosity  $\phi_c$  for the survival of macroscopic turbulence is between 0.95 and 0.97, which is similar to the DNS results.  $\phi_c$  is not sensitive to the Darcy number when it is in the range 0.3-1.2. When  $\phi_s$  is smaller than  $\phi_c$ , macroscopic turbulence cannot be stimulated even if  $Re_l \rightarrow \infty$ .

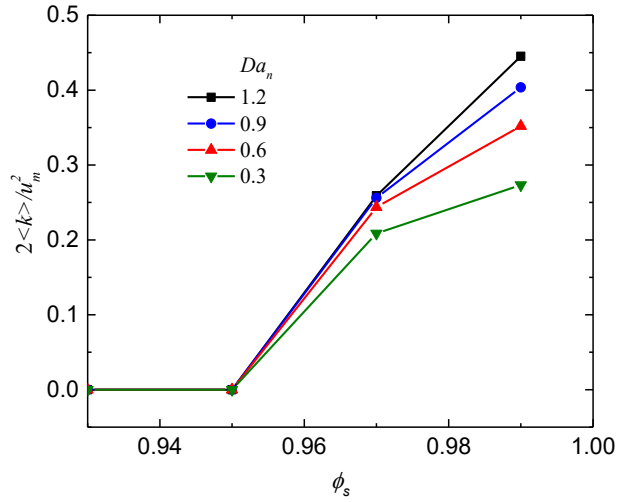


Figure 7.17. Normalized macroscopic turbulence kinetic energy  $2\langle k \rangle / u_m^2$  versus porosity versus,  $Re_l \rightarrow \infty$ ,  $Da_n \in [0.3, 1.2]$ , “bars+GPM”.

Figure 7.18 shows the relationship between the Reynolds number  $Re_K$  and the normalized macroscopic turbulence kinetic energy  $2\langle k \rangle / u_m^2$  for  $\phi_s = 0.98$  and different  $Da_n$  values. The onset of macroscopic turbulence occurs at  $Re_K = 133$  for  $Da_n = 0.39$  or  $Re_K = 120$  for  $Da_n = 0.10$ . The results are consistent with the statement by Nield and Bejan (2017) that the transition from a Darcy flow to a Darcy-Forchheimer flow occurs when  $Re_K$  is of order  $10^2$ . In addition, I have found that the values of  $2\langle k \rangle / u_m^2$  change only marginally when the  $Re_K$  is above 1000.

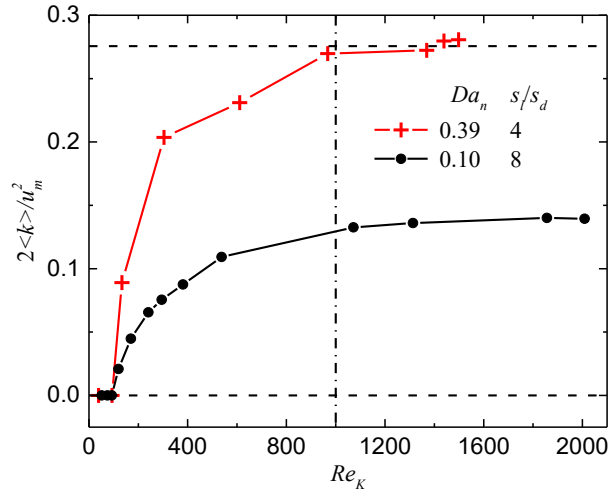


Figure 7.18. Reynolds number  $Re_K$  versus normalized kinetic energy of macroscopic turbulence  $2\langle k \rangle / u_m^2$ ,  $\phi_s = 0.98$ .

## 7.10 Conclusions

In order to understand whether macroscopic turbulence might survive in certain conditions and thus know the valid domain of the PSPH, I have studied the turbulent flows in porous matrices which have one or two length scales using DNS and macroscopic simulation. The large porous elements are made of 2-dimensional bars with the element size  $d_l$  and spacing  $s_l$ , while the small porous elements are made of spheres or cubes with the element size  $d_s$  and spacing  $s_s$ .

Instantaneous Q iso-surfaces, turbulent two-point correlations, integral length scales, and premultiplied energy spectra which are obtained from both DNS and macroscopic simulation are used to detect the possible macroscopic turbulence. The DNS results show that the critical porosity  $\phi_c$  for the survival of macroscopic turbulence is between 0.93 and 0.98 when the scale ratio  $s_l/s_s$  is set to 4. When the porosity is lower than  $\phi_c$ , the integral length scales for porous matrices with two length scales (“bars+spheres” or “bars+cubes”) are almost identical to those for porous matrices with only small porous elements (“spheres” or “cubes”). When the flow is fully turbulent, the value of  $\phi_c$  doesn’t change remarkably as the Reynolds number ( $Re_s$  or  $Re_l$ ) is increased or the pore-scale elements are changed from “spheres” to “cubes”.

The generality of the value of  $\phi_c$  is further studied using macroscopic simulation. The porous matrix made of spherical elements is modeled as a continuous porous medium whose geometric parameters were determined empirically in chapter 2. The macroscopic simulation results for “bars+spheres” show that  $\phi_c$  is in the range 0.95-0.97, which is close to the DNS results. Then, the macroscopic simulations for  $Re_l \rightarrow \infty$  and the Darcy number values in the range 0.3-1.2 are performed. The numerical results show that  $\phi_c$  is still in the range 0.95-0.97. It should be noted that that  $c_{B2}$  for our macroscopic simulation is calculated using Eq. (2.32) and the coefficient of the Forchheimer term is set to  $c_{F1} = 0.1$ . The effect of pore-scale geometries on these coefficients has not been taken into account in our study. In addition, the DNS is for only two pore-scale geometries (“spheres” and “cubes”). The dependence of the critical porosity on the pore-scale geometry still needs to be further investigated and ideally the scale ratio should be increased. This requires however extremely expensive simulations.

The comparison between the DNS and macroscopic simulation results also confirms the accuracy of the PSPH model proposed, as well as the capability of using this model to directly resolve the macroscopic turbulence in porous media.

# Chapter 8

## Summary and outlook

### 8.1 Summary

This Ph.D. thesis is dedicated to developing a macroscopic model taking into account laminar and turbulent flow in porous media. Due to the fact that DNS is often too computationally expensive and not practical in engineering applications, the cheap, efficient, and feasible macroscopic model was derived to study convection in porous media. In the following, the conclusions are summarized.

Based on the PSPH, a PSPH model for flows in porous media is derived by volume averaging the Navier-Stokes equations. The modeled terms include the drag term  $\hat{R}_i$  caused by the porous matrix and a Laplacian term  $L_i$  led by the gradient of macroscopic velocity. The  $\hat{R}_i$  is usually approximated by a Taylor expansion concerning a local Reynolds number  $Re_K$ . The Laplacian term  $L_i$  consists of effective viscosity  $\tilde{\nu}$  calculated by a local Reynolds number  $Re_d$  which characterizes the strength of momentum dispersion. Based on the PSPH, the pore size (identified by  $\sqrt{K}$ ) as the characteristic length and the mixing velocity  $\sqrt{K}|S_{Dij}|$  as the characteristic velocity constitute the local Reynolds number  $Re_d = \frac{K|S_{Dij}|}{\nu}$ . The ratio of effective viscosity to molecular viscosity is expanded as a Taylor series concerning  $Re_d$ . The two leading-order terms of the Taylor series are adopted in the present PSPH model. The coefficients  $c_{B1}$  and  $c_{B2}$  are determined by fitting the DNS results for flows in a wall-bounded porous medium made of the REV's under consideration. The coefficients are only related to the porosity. When the porosity is increased to 1, the effective viscosity approaches the molecular viscosity. When the porosity approaches 0, the effective viscosity approaches infinity.

The proposed macroscopic equations are used to simulate the flows in three types of porous media, a porous medium bounded by two walls, a porous medium with two porosities, and a porous medium with two length scales. The macroscopic equations are solved with the FVM by the linear interpolation for spatial discretization and with PISO algorithms for correcting the velocity field.

The Navier-Stokes solutions are approximated with the LBM indirectly by streaming and collision processes. The macroscopic model results are in good agreement with the DNS results in wide ranges of the Reynolds numbers, Darcy numbers, and porosities. The study shows that the effects of macroscopic velocity gradient on momentum transport in porous media can be reasonably well approximated using a Laplacian term.

Although the PSPH was validated in the previous studies (Jin *et al.*, 2015; Uth *et al.*, 2016), macroscopic turbulence must emerge when the flow is not restricted by the porous matrix and the porosity approaches 1. In order to find out under what conditions the macroscopic turbulence might survive and thus complement the PSPH, the porous matrix with two length scales (“bars+spheres” or “bars+cubes”) was applied to simulate turbulent flow by using DNS and macroscopic simulation. The large porous matrix stimulates strong large-scale turbulence, whereas the smaller porous matrix limits the size of turbulent coherent structures. Instantaneous Q iso-surfaces, turbulent two-point correlations, integral length scales, and premultiplied energy spectra were applied to measure the size of turbulent structures quantitatively and qualitatively. The DNS results indicated that the critical porosity  $\phi_c$  for the survival of macroscopic turbulence is between 0.93 and 0.98 when the scale ratio  $s_l/s_s$  is set to 4. Under the critical porosity, no macroscopic turbulence survives even if the Reynolds number ( $Re_s$  or  $Re_l$ ) is increased dramatically. The value of  $\phi_c$  does not change much as the Reynolds number ( $Re_s$  or  $Re_l$ ) is increased, or if the pore-scale elements are changed from “spheres” to “cubes” when the flow is fully turbulent. In order to confirm the generality of the critical porosity, the turbulent flow in the same porous medium only with the large-scale porous matrix using macroscopic simulation was simulated. The smaller porous matrix was modeled as a continuous porous medium, whose geometric parameters were determined empirically. Cases with the Reynolds number  $Re_l \rightarrow \infty$  and the different Darcy number values were computed. The macroscopic results indicate again that  $\phi_c$  is in the range 0.95-0.97 which is consistent with DNS results. And the accuracy and capability of the PSPH model proposed are further confirmed.

## 8.2 Outlook

An important perspective of the work is to study the probability of macroscopic turbulence where the Darcy number approaches 0. Jin *et al.* (2015) and Uth *et al.* (2016) provide a significant body of work that concluded the turbulent eddies are generally restricted by the pore size, leading to the pore-scale prevalence hypothesis (PSPH). Furthermore, the study in this thesis confirms no

survival of large-scale turbulence with infinite Reynolds numbers ( $Da_n \in [0.3, 1.2]$ ) and the porosity lower than the critical porosity. However, whether or not the macroscopic turbulence with the Darcy value close to 0 survives is still an open question. This question is useful in some systems where the Darcy number is low, such as heat transfer in porous media where the Darcy number could approach  $10^{-6}$  (Ebrahimi *et. al*, 2020).

Another significant question to be answered in the future is to take into account the effect of different geometries. In chapter 7, only the porous elements made of “sphere” and “cube” were considered to study the macroscopic turbulence in porous media with high porosity. Although the generality of the critical porosity is confirmed by using the macroscopic equations which model the porous matrices, the effect of the pore-scale geometry on the critical porosity still needs to be further validated.

This work can be extended to apply the macroscopic equations to the interface between the free flow and porous-medium flow. These flows near the interface are critical in the quantification of transferring fluxes of mass, momentum, and energy. The macroscopic turbulence in porous media enhances the convection. Although chapter 7 confirms the critical porosity above which macroscopic turbulence survives, how much depth the macroscopic turbulence in free flow due to Kelvin-Helmholtz stability penetrates the porous medium could be further researched. The macroscopic simulation with our developed PSPH model can be applied to do deep research about this interesting question.

# Appendix A.

DNS resolves turbulent flow accounting for all scales without any model. Therefore, the accuracy of DNS methods depends on the size of the given mesh. The finer mesh gives a solution of a little higher accuracy but at the expense of computational power and time. Quite generally the size of the best mesh is lower than the Kolmogorov scale  $\eta$  which depends on the local dissipation rate of the turbulent kinetic energy  $\varepsilon$  and the kinematic viscosity of the fluid  $\nu$ . However, it's hardly achieved, especially very close to the solid walls where the local dissipation rate  $\varepsilon$  is large and the Kolmogorov scale  $\eta$  is very little.

An alternative measure of checking mesh quality is comparing the pressure drop with the integration of the dissipation rate (Jin & Herwig, 2013). The accuracy of the DNS solution can be examined by an accuracy measure, which defines as:

$$\Delta = \frac{g_1 - g_s}{g_1} \quad (\text{A1})$$

where  $g_1$  and  $g_s$  are the pressure gradient in the streamwise direction and the volume-averaged dissipation rate in the computational domain. Jin *et al.* (2015) suggested that a solution with  $\Delta$  values below 10% for this type of flows is accurate enough for the analysis. Table A1 shows the values of  $\Delta$  for typical DNS cases.

Test cases	$\phi_s$	Mesh resolution	Accuracy		
			$Re_s$	$Re_l$	$\Delta$ (%)
"bars+spheres"	0.89	545 × 545 × 273	571	1941	8.0
	0.91	577 × 577 × 289	600	2160	6.3
	0.92	609 × 609 × 305	636	2417	5.6
	0.93	641 × 641 × 321	615	2460	5.1

---

	0.98	$961 \times 961 \times 481$	704	4224	1.0
“bars+cubes”	0.88	$641 \times 641 \times 321$	628	2512	7.3
	0.96	$961 \times 961 \times 481$	614	3684	1.3
	0.98	$1281 \times 1281 \times 641$	749	5992	0.2
“spheres”	0.70	$385 \times 385 \times 193$	465	1116	6.0
	0.76	$417 \times 417 \times 209$	476	1238	2.7
	0.81	$449 \times 449 \times 225$	647	1812	4.0
	0.84	$481 \times 481 \times 241$	623	1869	1.0
	0.87	$513 \times 513 \times 257$	775	2480	3.0
“bars”	-	$161 \times 161 \times 161$	-	528	3.0
	-	$161 \times 161 \times 161$	-	594	6.8
	-	$161 \times 161 \times 161$	-	630	7.9
	-	$161 \times 161 \times 161$	-	641	8.6
	-	$161 \times 161 \times 161$	-	653	8.5

Table A 1. Main parameters for the typical DNS cases, LBM.

---

# Bibliography

- AIDUN, C. K. & CLAUSEN, J. R. 2009 Lattice-Boltzmann method for complex flows. *Annu. Rev. Fluid Mech.* **41**, 439–472.
- ANTOHE, B. V. & LAGE, J. L. 1997 A general two-equation macroscopic turbulence model for incompressible flow in porous media. *Intl J. Heat Mass Transfer* **40**, 3013-3024.
- AURIAULT, J. L. 2009 On the domain of validity of Brinkman’s equation. *Transp Porous Med* **79**, 215-223.
- BALAKUMAR, B. J. & ADRIAN, R. J. 2007 Large- and very-large-scale motions in channel and boundary-layer flows. *Phil. Trans. R. Soc. Lond. A* **365**, 665-681.
- BEAR, J., BACHMAT, Y. 1990 Introduction to modeling of Transport Phenomena in Porous media. Kluwer Academic, Dordrecht.
- BEAVERS, G. S., SPARROW, E. M., RODENZ, D. E. 1973 Influence of bed size on the flow characteristics and porosity of randomly packed beds of spheres. *J. Appl. Mech.* **40**(3), 655-660.
- BELCHER, S. E., HARMAN, I. N. & FINNIGAN, J. F. 2012 The wind in the willows: flows in forest canopies in complex terrain. *Annual Review of Fluid Mechanics* **44**, 479-504.
- BHATNAGAR, P. L., GROSS, E. P. & KROOK, M. 1954 A model for collision processes in gases. I. Small amplitude processes in charged and neutral one-component systems. *Phys. Rev.* **94**, 511–525.
- BOOMSMA, K., POULIKAKOS, D. & ZWICK, F. 2003 Metal foams as compact high performance heat exchangers. *Mechanics of materials* **35**(12), 1161-1176.
- BOWLING, D. R. & MASSMAN, W. J. 2011 Persistent wind-induced enhancement of diffusive

- CO<sub>2</sub> transport in a mountain forest snowpack. *J. of Geophysical Research* **116 (1)**, G04006.
- BREUGEM, W. P., BOERSMA, B. J. & UITTENBOGAARD, R. E. 2006 The influence of wall permeability on turbulent channel flow. *J. Fluid Mech.* **562**, 35.
- BRINKMAN, H. C. 1947 A calculation of the viscous force exerted by a flowing fluid on a dense swarm of particles. *Appl. Sci. Res. A* **1**, 27-34.
- BROWN, M. J. 2001 Comparison of centerline velocity measurements obtained around 2D and 3D building arrays in a wind tunnel. In *Proceedings of the International Society of Environmental Hydraulics Conference*, Tempe, AZ, USA.
- BRUANT, R. G., JR, J., CELIA, M. A., GUSWA, A. J., PETERS, C. A. 2002 Peer Reviewed: Safe storage of CO<sub>2</sub> in Deep Saline Aquifers. *Environ. Sci. Technol.* **36(11)**, 240A-245A.
- CALMIDI, V. V., MAHAJAN, R. L. 1999 The effective thermal conductivity of high porosity fibrous metal foams. *Journal of Heat Transfer-Transactions of the ASME* **121**, 466-471.
- CARMAN, P. C. 1956 *Flow of gases through porous media*. Academic Press.
- CERRI, G., GIOVANNELLI, A., BATTISTI, L. & FEDRIZZI, R. 2007 Advances in effusive cooling techniques of gas turbines. *Applied Thermal Engineering* **27**, 692-698.
- CHEN, G., WANG, D., WANG, Q., LI, Y., WANG, X., HANG, J., GAO, P., OU, C. & WANG, K. 2020b Scaled outdoor experimental studies of urban thermal environment in street canyon models with various aspect ratios and thermal storage. *Sci.Total. Environ.* **726**, 138147.
- CHEN, G., YANG, X., YANG, H., HANG, J., LIN, Y., WANG, X., WANG, Q. & LIU Y. 2020a The influence of aspect ratios and solar heating on flow and ventilation in 2D street canyons by scaled outdoor experiments. *Build. Environ.* **185**, 107159.
- CHEN, S. & DOOLEN, G. D. 1998 Lattice Boltzmann method for fluid flows. *Annu. Rev. Fluid Mech.* **30**, 329-364.

- CHU, X., WEIGAND, B. & VAIKUNTANATHAN, V. 2018 Flow turbulence topology in regular porous media: from macroscopic to microscopic scale with direct numerical simulation. *Phys. Fluids*. **30**, 065102.
- DAHMEN, W., GOTZEN, T., MÜLLER, S. & ROM, M. 2014 Numerical simulation of transpiration cooling through porous material. *Int. J. Numer. Meth. Fluids* **76**, 331-365.
- DE LANGRE, E. 2008 Effects of wind on plants. *Annu. Rev. Fluid Mech.* **40**, 141-168.
- DE LEMOS, M. J. S. 2005 The double-decomposition concept for turbulent transport in porous media. In: Ingham, D.B., Pop, I. (eds.) *Transport Phenomena in Porous Media III*. pp.1-33. Elsevier, Oxford.
- DE LEMOS, M. J. S. 2009 Numerical simulation of turbulent combustion, in porous materials. *International communications in Heat and Mass Transfer* **36**(10), 996-1001.
- DE LEMOS, M. J. S. 2012a *Turbulence in Porous Media: Modeling and Applications*, 2nd edn. Elsevier, Oxford.
- DE LEMOS, M. J. S. 2012b *Turbulent Impinging Jets into Porous Media*. Springer, New York.
- DURLOFSKY, L., BRADY, J. F. 1987 Analysis of the Brinkman equation as a model for flow in porous media. *Phys. Fluids*. **30**, 3329-3341.
- EBRAHIMI, E., AMINI, Y. & IMANI, G. 2020 Numerical study of fluid flow and heat transfer characteristics of an oscillating porous circular cylinder in crossflow. *Phys. Fluids*. **32**(2), 023602.
- EPSTEIN, N. 1989 On tortuosity and the tortuosity factor in flow and diffusion through porous media. *Chemical Engineering Science*. **44** (3): 777-779.
- FAN, J. & WANG, L. 2011 Analytical theory of bioheat transport. *Journal of Applied Physics* **109**, 104702.
- FAN, Y, HUNT, J. C. R. & LI, Y. 2017 Buoyancy and turbulence-driven atmospheric circulation

- over urban areas. *J. Environ. Sci.* **59**, 63–71.
- GERRITSEN, M. G., CHEN, T., CHEN, Q. 2005 personal communication. Stanford University, California.
- GETACHEW, D., MINKOWYCY, W. J. & LAGE, J. L. 2000 A modified form of the  $\kappa - \varepsilon$  model for turbulent flows of an incompressible fluid in porous media. *Intl. J. Heat Mass Transfer* **43**, 2909-2915.
- GHISALBERTI, M. & NEPF, H. 2009 Shallow flows over a permeable medium: the hydrodynamics of submerged aquatic canopies. *Transp Porous Med* **78**, 309.
- GIVLER, R. C., ALTOBELLI, S. 1994 A determination of the effective viscosity for the Brinkman-Forchheimer flow model. *J. Fluid Mech.* **258**, 355-370.
- GOMES-FERNANDES, R., GANAPATHISUBRAMANI, B. & VASSILICOS, J. C. 2015 The energy cascade in near-field non-homogeneous non-isotropic turbulence. *J. Fluid Mech.* **771**, 676-705.
- GRAY, W. G. & LEE, P. C. Y. 1977 On the theorems for local volume averaging of multiphase systems. *Int. J. Multiphase Flow* **3**, 333-340.
- GREBENYUK, Y. & DREYER, M. E. 2016 Wicking of liquid nitrogen into superheated porous structures. *Cryogenics* **78**, 27-39.
- GREBENYUK, Y., ZHANG, H. X., WILHELM, M., REZWAN, K. & DREYER, M. E. 2017 Wicking into porous polymer-derived ceramic monoliths fabricated by freeze-casting. *Journal of the European Ceramic Society* **37(5)**, 1993-2000.
- GRISAN, E., FORACCHIA, M. & RUGGERI, A. 2003 A novel method for automatic evaluation of retinal vessel tortuosity. *Proceedings of the 25th Annual International Conference of the IEEE EMBS*, Cancun, Mexico.
- GUALA, M., HOMMEMA, S. E. & ADRIAN, R. J. 2006 Large-scale and very-large-scale motions in turbulent pipe flow. *J. Fluid Mech.* **554**, 521-542.

- HANG, J. & LI, Y. 2010 Wind conditions in idealized building clusters: macroscopic simulations using a porous turbulence model. *Bound. Layer Meteorol.* **136**, 129–159.
- HART, W. E., GOLDBAUM, M., COTE, B., KUBE, P. & NELSON, M. R. 1999 Automated measurement of retinal vascular tortuosity. *International Journal of Medical Informatics.* **53** (2–3), 239–252.
- HEINEMANN, N., ALCALDE, J., MIOCIC, J. M., HANGX, S. J. T., KALLMEYER, J., OSTERTAG-HENNING, C., HASSANPOURYOUBAND, A., THAYSEN, E. M., STROBEL, G. J., WILKINSON, M., SCHMIDT-HATTENBERGER, C., EDLMANN, K., BENTHAM, M., HASZELDINE, R. S., CARBONELL, R., RUDLOFF, A. 2021 Enabling Large-Scale Hydrogen Storage in Porous Media - the Scientific Challenges. *Energy Environ. Sci.* **14**, 853.
- HIRSCH, C. 2007 *Numerical Computation of Internal and External Flows: The Fundamentals of Computational Fluid Dynamics*, 2nd edn. Butterworth-Heinemann.
- HSU, C. T., CHENG, P. 1990 Thermal dispersion in a porous medium. *Int. J. Heat Mass Transfer.* **33**, 1587-1597
- HSU, P.-F., HOWELL, J. R., MATTHEWS, R. D. 1993 A numerical investigation of premixed combustion within porous inert media. *Journal of Heat Transfer* **115**, 744-750.
- HUNT, J. C. R., WARY, A. A. & MOIN, P. 1988 Eddies, stream, and convergence zones in turbulent flows. *Center for Turbulence Research Report CTR-S88*, pp. 193-208.
- INGHAM, D. B. & POP. I. 1998, *Transport phenomena in porous media*, Elsevier.
- IRMAY, S. 1958 On the theoretical derivation of Darcy and Forchheimer formulas. *Trans. Am. Geophys. Union.* **39**(4), 702-707.
- ISSA, R. I. 1986 Solution of the implicitly discretized fluid flow equations by operator splitting.

*Journal of Computational Physics.* **62**, 40-65.

JIMENEZ, J. 1998 The largest scales of turbulent wall flows. In *Center for Turbulence Research, Annual Research Briefs*, pp. 137-154. Stanford University.

JIN, Y. & HERWIG, H. 2013 From single obstacles to wall roughness: some fundamental investigations based on DNS results for turbulent channel flow. *Z. Angew. Math. Phys.* **64**, 1337-1352.

JIN, Y. & KUZNETSOV, A. V. 2017 Turbulence modeling for flows in wall bounded porous media: an analysis based on direct numerical simulations. *Phys. Fluids.* **29**, 045102.

JIN, Y., UTH, M.-F., KUZNETSOV, A. V. & HERWIG, H. 2015 Numerical investigation of the possibility of macroscopic turbulence in porous media: A direct numerical simulation study. *J. Fluid Mech.* **766**, 76-103.

KAZEROONI, R. B. & HANNANI, S. K. 2009 Simulation of turbulent flow through porous media employing a v2f model. *Sci. Iran. Trans. B* **16**, 159-167.

KHALED, A. -R. A. & VAFAI, K. 2003 The role of porous media in modeling flow and heat transfer in biological tissues. *Int. J. Heat Mass Transfer* **46**, 4989–5003.

KHANAFER, K. & VAFAI, K. 2006 The role of porous media in biomedical engineering as related to magnetic resonance imaging and drug delivery. *Heat Mass Transfer* **42**, 939–953.

KIM, T., BLOIS, G., BEST, J. L. & CHRISTENSEN, K. T. 2020 Experimental evidence of amplitude modulation in permeable-wall turbulence. *J. Fluid Mech.* **887**, A3.

KOLMOGOROV, A. N. 1941 Dissipation of energy in locally isotropic turbulence. *Dokl. Akad. Nauk SSSR* **32**, 19-21.

KOZENY, J. 1927 Ueber kapillare Leitung des Wassers im Boden. *Sitzb. Akad. Wiss. Wien. Math. naturw. Klasse.* **136**, 271-306.

KUNDU, P., KUMAR, V. & MISHRA, I. M. 2014 Numerical modeling of turbulent flow through isotropic porous media. *Intl. J. Heat Mass Transfer* **75**, 40-57.

- KUWAHARA, F., KAMEYAMA, Y., YAMASHITA, S. & NAKAYAMA, A. 1998 Numerical modeling of turbulent flow in porous media using a spatially periodic array. *J. Porous Media* **1**, 47-55.
- KUZNETSOV, A. V. 1997 Influence of the stress jump condition at the porous-medium/clear-fluid interface on a flow at a porous wall. *Int. Comm. Heat Mass Transfer*. **24**, 401-410.
- KUZNETSOV, I. A., KUZNETSOV, A. V. 2017 Using resampling residuals for estimating confidence intervals of the effective viscosity and Forchheimer coefficient. *Transp. Porous Med.* **119**, 451-459.
- LAGE, J. L. & ANTOHE, B. V. 2000 Darcy's experiments and the deviation to nonlinear flow regime. *J. Fluids Eng.* **122**, 619-625.
- LAGE, J. L., ANTOHE, B. V., NIELD, D. A. 1997 Two types of nonlinear pressure drop versus flow-rate relation observed for saturated porous media. *J. Fluids Eng.* **119**(3), 701-706.
- LASSEUX, D., VALDÉS-PARADA, F. J., BELLET, F. 2019 Macroscopic model for unsteady flow in porous media. *J. Fluid Mech.* **862**, 283-311.
- LATT, J., MALASPINAS, O., Kontaxakis, D. *et al.* 2020 Palabos: Parallel Lattice Boltzmann Solver. *Computers & Mathematics with Applications*. **81**, 334-350.
- LEE, K. B. & HOWELL, J. R. 1991 Theoretical and experimental heat and mass transfer in highly porous media. *Intl. J. Heat Mass Transfer* **34**, 2123-2132.
- LEVY, T. 1981 Loi de Darcy ou loi de Brinkman? *C. R. Acad. Sci. Paris, Sér. II.* **292**, 872-874.
- LIEN, F. S., YEE, E., CHENG, Y. 2004 Simulation of mean flow and turbulence over a 2D building array using high-resolution CFD and a distributed drag force approach. *J. Wind. Eng. Ind. Aerodyn.* **92**, 117-158.
- MAIER, M., SCHACK-KIRCHNER, H., AUBINET, M., GOFFIN, S., LONGDOZ, B. &

- PARENT, F. 2012 Turbulence effect on gas transport in three contrasting forest soils. *Soil Sci. Soc. Am. J.* **76**, 1518-1528.
- MASUOKA, T., TAKATSU, Y. 1996 Turbulence model for flow through porous media. *Int. J. Heat Mass Transfer.* **39**, 2803-2809.
- MERONEY, R. N. 2007 Fires in porous media: natural and urban canopies. In *Flow and Transport Processes with Complex Obstructions* (ed. Y. A. Gayev & J. C. Hunt), vol. 236. Springer.
- MOHAMAD, A. A. 2011 *Lattice Boltzmann Method*. Springer.
- NAKAYAMA, A. & KUWAHARA, F. 1999 A macroscopic turbulence model for flow in a porous medium. *Trans. ASME. J. Fluids Eng.* **121**, 427-433.
- NAKAYAMA, A. & KUWAHARA, F. 2008 A general bioheat transfer model based on the theory of porous media. *Int. Heat Mass Transfer* **51**, 3190–3199.
- NEPF, H. M. 2012 Flow and transport in regions with aquatic vegetation. *Ann. Rev. Fluid Mech.* **44**, 123-142.
- NIELD, D. A. 1991 The limitations of the Brinkman-Forchheimer equation in modeling flow in a saturated porous medium and at an interface. *Intl J. Heat Fluid Flow* **12**, 269-272.
- NIELD, D. A. 2001 Alternative models of turbulence in a porous medium, and related matters. *ASME. J. Fluids Eng.* **123**, 928-931.
- NIELD, D. A. & BEJAN, A. 2017 *Convection in Porous media*, 5th edn. Springer.
- OCHOA-TAPIA, J. A., WHITAKER, S. 1995 Momentum transfer at the boundary between a porous media and a homogeneous fluid – I. Theoretical development. *Int. J. Heat Mass Transfer.* **38**, 2635-2646.
- OPENFOAM 2018 The open source CFD toolbox for OpenFOAM: <http://www.openfoam.com>. (accessed on 01.10.2021)
- PATASIUS, M., MAROZAS, V., LUKOSEVICIUS, A. & JEGELEVICIUS, D. 2005 Evaluation

- of tortuosity of eye blood vessels using the integral of square of derivative of curvature [elektroninis isteklius]. *In proceedings of the 3rd IFMBE European Medical and Biological Engineering Conference, IFMBE European Conference on Biomedical Engineering EMBEC'05, Prague, Czech Republic, Volume 11.*
- PICKL, M. J. 2019 The renewable energy strategies of oil majors-From oil to energy? *Energy Strategy Reviews* **26**, 100370.
- POPE, S. B. 2000 *Turbulent Flows*. Cambridge University Press.
- PRANDTL, L. 1925 Bericht über untersuchungen zur ausgebildeten turbulenz. *Z. Angew. Math. Mech.* **5**(1), 136–139.
- PRESCOTT, P. J. & INCROPERA, F. P. 1995 The effect of turbulence on solidification of a binary metal alloy with electromagnetic stirring. *ASME J. Heat Transfer* **117**, 716-724.
- RAO, F., KUZNETSOV, A. V. & JIN, Y. 2020 Numerical modeling of momentum dispersion in porous media based on the pore scale prevalence hypothesis. *Transp Porous Med* **133**, 271-292.
- ROETZEL, W. & XUAN, Y. 1998 Transient response of the human limb to an external stimulus. *Int. J. Heat Mass Transfer* **41**, 229–239.
- RUBINSTEIN, J. 1986 Effective equations for flow in random porous media with a large number of scales. *J. Fluid Mech.* **170**, 379-383
- RUBOL, S., LING, B. & BATTIATO, I. 2018 Universal scaling-law for flow resistance over canopies with complex morphology. *Sci Rep* **8**, 4430.
- SAEZ, A. E., PERFETTI, J. C. & RUSINEK, I. 1991 Prediction of effective diffusivities in porous media using spatially periodic models. *Transp. Porous Med.* **6**, 143-157.
- SANYAL, D. C. & MAJI, N. K. 2001 Thermoregulation through skin under variable atmospheric and physiological conditions. *J. Theor. Biol.* **208**(4), 451-456.

- SCRITTORE, J. J., THOLE, K. A. & BURD, S. W. 2007 Investigation of velocity profiles for effusion cooling of a combustor liner. *J. Turbomach.* **129** (3), 518-526.
- SERRA, T., FERNANDO, H. J. S. & RODRIGUEZ, R. 2004 Effects of emergent vegetation on lateral diffusion in wetlands. *Water Res.* **38**, 139-47.
- SIAVASHI, M., RASAM, H. & IZADI, A. 2019 Similarity solution of air and nanofluid impingement cooling of a cylindrical porous heat sink. *Journal of Thermal Analysis and Calorimetry* **135**(2), 1399-1415.
- SLATTERY, J. C. 1967 Flow of viscoelastic fluids through porous media. *AIChE J.* **13**, 1066-1071.
- SRIKANTH, V., HUANG, C. W., SU, T. S. & KUZNETSOV, A. V. 2018 Symmetry breaking in porous media as a consequence of the von Kármán instability. *arXiv: Fluid Dynamics*, 1810.10141.
- SUGA, K. 2016 Understanding and modelling turbulence over and inside porous media. *Flow, Turbulence and Combustion.* **96**(3), 717-756.
- TAHERI, H. 2014 Numerical investigation of stratified thermal storage tank applied in adsorption heat pump cycle. PhD thesis Karlsruher Institut für Technologie.
- TAM, C. K. W. 1969 The drag on a cloud of spherical particles in low Reynolds number flow. *J. Fluid Mech.* **38**(3), 537-546.
- TANINO, Y. & NEPF, H. M. 2008 Lateral dispersion in random cylinder arrays at high Reynolds number. *J. Fluid Mech.* **600**, 339-371.
- TUCCI, C., TRUJILLO, M., BERJANO, E., IASIELLO, M., ANDREOZZI, A. & VANOLI, G. P. 2021 Pennes' bioheat equation vs. porous media approach in computer modeling of radiofrequency tumor ablation. *Sci. Rep.* **11**, 1–13.

- UTH, M.-F., JIN, Y., KUZNETSOV, A. V. & HERWIG, H. 2016 A direct numerical simulation study on the possibility of macroscopic turbulence in porous media: effects of different solid matrix geometries, solid boundaries, and two porosity scales. *Phys. Fluids*. **28**, 065101.
- VAFAI, K., TIEN, C. L. 1981 Boundary and inertial effects on flow and heat transfer in porous media. *Int. J. Heat Mass Transfer*. **24**, 195-203.
- VAFAI, K., TIEN, C. L. 1982 Boundary and inertial effects on convective mass transfer in porous media. *Int. J. Heat Mass Transfer*. **25**, 1183-1190
- VAFAI, K. 2015 *Handbook of porous media*, 3th edn. CRC Press.
- VALDES-PARADA, F. J., OCHOA-TAPIA, J. A., ALVAREZ-RAMIREZ, J. 2007 On the effective viscosity for the Darcy-Brinkman equation. *Physical A: Statistical Mechanics and its Applications*. **385**, 69-79.
- WARD, J. C. 1964 Turbulent flow in porous media. *Journal of the Hydraulics Division*. **90**, 1-12.
- WHITAKER, S. 1969 Advances in theory of fluid motion in porous media. *Ind. Eng. Chem.* **61**, 14-28.
- WHITAKER, S. 1999 *The Method of Volume Averaging*. Springer.
- WINSTON, G. C., STEPHENS, B. B., SUNDQUIST, E. T., HARDY, J. P. & DAVIS, R. E. 1995 Seasonal variability in CO<sub>2</sub> transport through snow in a boreal forest. *Biogeochemistry of Seasonally Snow-Covered Catchm* **228**, 61-70.
- WOOD, B. D., HE, X. L., APTE, S. V. 2020 Modeling turbulent flows in porous media. *Annu. Rev. Fluid Mech.* **52**, 171-203.